Mixing processes in the changing Arctic Ocean

Algot K. Peterson

Thesis for the degree of philosophiae doctor (PhD)
at the University of Bergen

2017

Date of defence: 11.08.2017

Scientific environment

This study was carried out at the Geophysical Institute, University of Bergen. The study was funded by the Norwegian Research Council, through the grant 229786. Additional support was provided by the Centre for Climate Dynamics at the Bjerknes Centre, through the grant BASIC: Boundary Layers in the Arctic Atmosphere, Seas and Ice Dynamics. I have been enrolled in the ResClim research shool for Climate Science, who also provided several relevant courses. The field work involving the drift of R/V Lance was supported by the Norwegian Polar Institute's Centre for Ice, Climate and Ecosystems (ICE) through the N-ICE project. My supervisors are Ilker Fer (UiB) and Miles G. McPhee (McPhee Research).

UNIVERSITY OF BERGEN
Faculty of Mathematics and Natural Sciences

BJERKNES CENTRE
for Climate Research

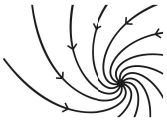

ResClim
RESEARCH SCHOOL IN CLIMATE DYNAMICS

Acknowledgements

First of all, I would like to thank my main supervisor Ilker Fer, for thorough feedback, invaluable help and advice throughout. Your door was always open whenever I had questions. Thank you for all the opportunities you have provided me with, and for encouraging me to also pursue my own interests. I am also grateful towards my co-supervisor Miles McPhee, for facilitating the under-ice turbulence measurements, and for help and advice along the way.

From the field campaigns, I want to thank all the great people that have made this study possible, at UiB, NPI and elsewhere. To the whole of N-ICE's Leg 2 group of scientists, Lance's ship crew and WP7, thank you for making the time in the Arctic winter such a memorable one. From the long days on the ice over the deep Arctic, I'm grateful that Amélie Meyer was there with me during long MSS shifts, TIC debugging and polar bear guarding, and for all the energy she put into the project. Thanks to the crew of K/V Svalbard, who were involved both in the N-ICE operations, and in mooring deployment on the Yermak Plateau. Thanks to Jen MacKinnon for having me tag along on your ArcticMix cruise. And to the ArcticMix team, I'm happy I got to see the flip side of the Arctic Ocean with such an awesome group of scientists and ship crew on the R/V Siquilaq, from which I learned a great deal.

Thanks to Kjetil and Anthony for good office company and conversations. To the aquarium fishes at SKD, thanks for the many coffee breaks over the years. Too all who engaged in Galε, I look back at all the good beers we made (and drank) in the after-hours at GFI, ensuring the success of all the parties at the institute.

Finally, I want to thank my friends and family who have provided support and encouragement, distractions and fun through these years. Most of all, I want to direct my gratitude to Ida, for being my reason to come home from work in the afternoon, and for her constant support and faith in me. And for our dog Iver, who always jumps for joy when I get home, no matter how my day has been.

The difficult is what takes a little time,
the impossible is what takes a little longer.

Fridtjof Nansen

Abstract

The Arctic has undergone tremendous changes the last decades, including a strong decline in sea ice extent and thickness. The rapid pace of Arctic changes relative to the global changes are known as Arctic amplification, and has been referred to as the 'canary in the coalmine' of the present climate changes. Factors contributing to the accelerated changes are the ice-albedo effect, and the vast heat reservoir of Atlantic water flowing in the ocean below. This study has aimed to describe and quantify the influence of oceanic heat on the heat budget at the ocean's upper boundary.

There is a delicate heat balance at the interface between the atmosphere, the sea ice and the ocean. A small change in heat flux can have large effect on the ice cover. While the Arctic Ocean is generally not a very energetic one, the recent changes has raised concern about whether internal wave energy and the importance of vertical mixing processes are increasing. Reductions in sea ice extent may allow for more momentum transfer from the atmosphere to the ocean, either mixing the surface layer directly, or initiating inertial oscillations in the boundary layer. Near-inertial internal waves may propagate into the interior and cause mixing away from the surface boundary layer. An increase in vertical mixing in the Arctic Ocean may bring up more heat from the underlying warm Atlantic Water, posing a further threat to the diminishing Arctic sea ice.

The study is based on observations from two different campaigns, both located in the region north of Svalbard. First, under-ice boundary layer and upper ocean measurements made during the winter-to-spring drift campaign N-ICE2015. Second, a yearlong deployment of three moorings on the slope of the Yermak Plateau is used to study the near-inertial wave field by the plateau.

From an under-ice turbulence mast, a unique data set of winter-time measurements over the deep basin is obtained. Direct measurements of heat fluxes are weakly positive, even in winter, which are roughly doubled during storm events. Individual events can cause an order of magnitude increase in fluxes. A one-dimensional vertical diffusion model based on the observations from the drift satisfactorily reproduced observed changes in upper ocean winter hydrography. The model further suggests that observed salinity increase in the mixed layer was dominated by entrainment of saline water from below, rather than brine rejection from ice growth.

In spring, coincident with drift over the shallower topography, where the warm Atlantic Water is found at shallow depths, heat fluxes below the sea ice are much higher. Varying by one to two orders of magnitude, heat fluxes are highly dependent on the depth of the warm water layers, the wind forcing and its effect on the ice cover. Highest heat fluxes exceeded $100\,\mathrm{W\,m^{-2}}$ over several hours, during a wind event in the marginal ice zone.

From a subset of the under-ice turbulence measurements, during sea ice melt in June, heat and salt fluxes are found to be inversely correlated. This is contrary to expectations of positive heat- and salt fluxes during sea ice melt. This is hypothesized to origin in salt released from the melting sea ice. Objective criteria are used to identify 131 salty plumes descending past the measurement volume, accounting for 9% of the salt fluxes in only 0.5% of the time. The accumulated salt flux indicate a near full desalination of the sea ice. The reduction in bulk salinity of two nearby ice cores, taken three days apart, agree with accumulated salt flux within a factor of two. Plumes have previously only been observed from land-fast ice in a Svalbard fjord. The study confirms its existence on drifting Arctic sea ice, with implications for the understanding of salt and freshwater distribution in the under-ice boundary layer, and brine drainage in sea ice.

From the southwestern Yermak Plateau, the near-inertial field was analyzed in year-long records from three moorings. The near-inertial signal is clockwise dominant, indicative of downward energy propagation. The clockwise polarization is stronger closer to the surface, further suggesting surface generation by winds. Examples of wind-generated near-inertial wave propagation are presented, and wave group properties are calculated. At mid-depth and in the deep, episodic events of elevated near-inertial horizontal kinetic energy can be caused by surface generation at a remote location, or by tidal currents interacting with the rough topography. Theoretical characteristic beam paths initiated at the shelf break are consistent with the mid-depth elevation in near-inertial horizontal kinetic energy.

The sum of these observations further highlight the importance and complexity of ocean mixing processes, both at the ice-ocean interface and at depth. The Yermak Plateau is a region of significant internal wave generation and energetic turbulence, and will be an important and interesting region for further studies. The diapycnal mixing taking place here is key in determining the vertical exchange of heat between inflowing Atlantic water and the surface, and the fate of this heat in the Arctic basins.

List of papers

1. **Algot K. Peterson**, Ilker Fer, Miles G. McPhee, Achim Randelhoff
   Turbulent heat and momentum fluxes in the upper ocean under Arctic sea ice, Journal of Geophysical Research - Oceans **122**, 2017. DOI: 10.1002/2016JC012283

2. Ilker Fer, **Algot K. Peterson**, Achim Randelhoff, Amelie Meyer
   One-dimensional evolution of the upper water column in the Atlantic sector of the Arctic Ocean in winter, Journal of Geophysical Research - Oceans **122**, 2017. DOI: 10.1002/2016JC012431

3. **Algot K. Peterson**
   Observations of brine plumes below Arctic sea ice, Ocean Science Discussions, 2017. doi:10.5194/os-2017-27.

4. **Algot K. Peterson**, Ilker Fer
   Near-inertial internal wave variability from one-year duration moored measurements near the Yermak Plateau, Arctic Ocean, manuscript in preparation.

Contents

Chapter 1

Introduction

The Arctic Ocean is known as a 'low energy' ocean, with little energy available to cause mixing in the ocean's interior. Dramatic changes in the state of Arctic sea ice in recent decades has raised the hypothesis that energy transfer to the ocean will increase, and potentially drive more upward mixing of underlying warm water masses. Increased mixing can further increase the sea ice melt, potentially threatening the perennial ice cover. So far the evidence is equivocal.

1.1 The Arctic Ocean

1.1.1 Atlantic Water Inflow

The Arctic Ocean is a mediterranean sea, limiting exchange of oceanic heat, freshwater and export of sea ice (Figure 1.1). Two deep basins are surrounded by shallow continental slopes. The Arctic Ocean is connected to the Pacific Ocean through the Bering Strait, and to the Atlantic Ocean through the Canadian Archipelago, Fram Strait and the Barents Sea. The only deep connection is Fram Strait, situated between Greenland and Svalbard, with a sill depth of 2500 m.

The Norwegian Atlantic Current carries warm and saline Atlantic Water (AW) to the Arctic Ocean. One branch of the current enters the Barents Sea north of Norway, but is partly recirculated back in the western Barents Sea (Skagseth, 2008), while the remainder loses most of its heat on its path towards the Nansen Basin (Årthun and Schrum, 2010). The remainder of the AW continues northward through Fram Strait as the West Spitsbergen Current (WSC). North of Svalbard, the AW continues as a subsurface boundary current. As it reaches the Yermak Plateau (YP), the WSC is divided further. Part of the water detaches from the continental slope, and recirculates to the Fram Strait. The rest continues northward along the YP (Yermak branch), or along the slopes of Svalbard at shallower depths (Svalbard branch). The AW continues to circulate cyclonically along the continental slopes, and is found at intermediate depths

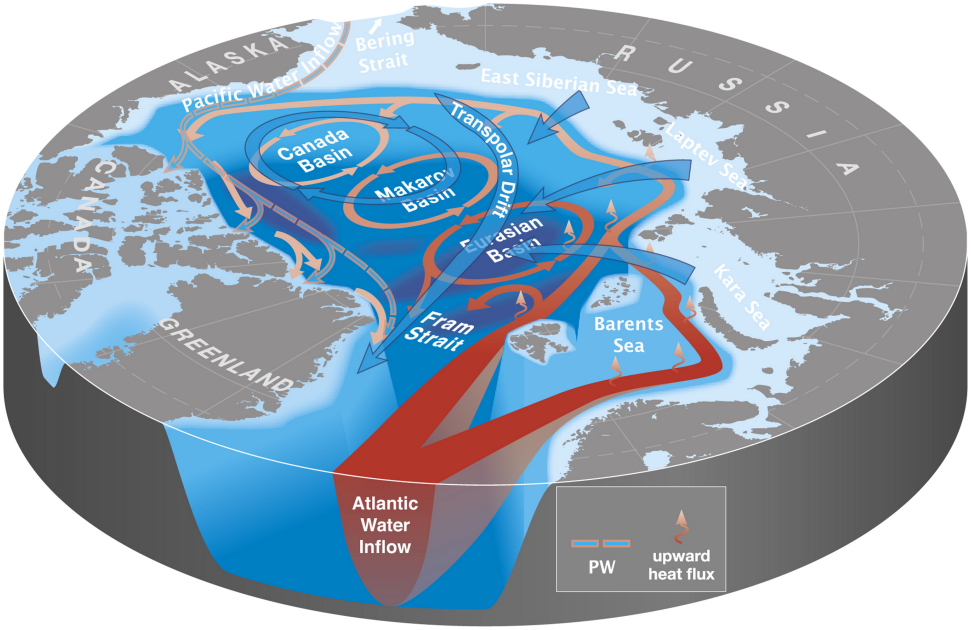

Figure 1.1: Map of the Arctic Ocean, schematically showing the inflow of warm Atlantic Water (red), intermediate Pacific water (pink/blue) and circulation of surface waters (blue). From Carmack et al. (2015).

(200-700m) all over the Arctic Ocean.

The WSC is the greatest heat source to the Arctic Ocean (Aagaard and Greisman, 1975). Net northward volume transport across the strait is estimated to 6.6 ± 0.4 Sverdrups[1] (Beszczynska-Möller et al., 2012), with a heat transport in the WSC of 26 TW to 50 TW[2] relative to an inflow temperature of 1 °C (Schauer and Beszczynska-Möller, 2009). Observations of warm pulses in the AW inflow, raised concern of an increased AW heat flux to overlying layers, eventually threatening the sea ice cover (Polyakov et al., 2011, 2005). Turner (2010) estimated that the Atlantic Water inflow contains enough heat to melt all Arctic sea ice in a few years, would it reach the surface.

1.1.2 The Cold Halocline Layer

The cold and fresh Arctic surface waters are separated from the warm and saline AW by the presence of a cold halocline layer (CHL), where increasing salinity with depth (halocline) causes a strong density gradient, while temperature remains close to freezing (Figure 1.2). In effect, any mixing across the pycnocline will thus only bring cold water towards the surface, effectively reducing the turbulent flux of heat from the AW layer

[1] Sverdrups (Sv); $1\ \mathrm{Sv} = 1 \times 10^6\ \mathrm{m^3\,s^{-1}}$
[2] Terawatt (TW), $1\ \mathrm{TW} = 10^6\ \mathrm{W}$

(Aagaard et al., 1981). Observations have shown that the main source of ocean heat flux in the central Arctic is solar heating through openings in the ice cover, thin ice and melt ponds (Maykut and McPhee, 1995; Perovich and Elder, 2002; Shaw et al., 2009), rather than AW heat. A central formation mechanism of the CHL is by salt release from ice formation on the continental shelves. Salt increases density of the cold surface waters until they finally descend on the slopes and forms the cold and saline CHL (Aagaard et al., 1981, Figure 1.2). Rudels et al. (1996) suggested a more advective mechanism, which gives less credit to brine rejection on the shelves. Winter convection north of Barents Sea forms a cold, saline layer is formed, which advects with the AW around the basin. When the flow reaches the eastern Eurasian Basin shelf water is encountered, which is fresh from river run-off, homogenized by winter convection, giving rise to the cold and fresh upper layer.

In the 1990's, a retreat of the CHL was observed, which was associated with advance and shoaling of the AW layer (Steele and Boyd, 1998). From a simple model they estimated that annually averaged heat fluxes could increase by as much as $1.5\,\mathrm{W\,m^{-2}}$, a 30-40% increase relative to previous observations by Maykut and McPhee (1995). A partial recovery of the CHL was later observed, and the changes in the halocline and upper ocean salinity were related to changes in circulation of fresh surface waters (Björk et al., 2002; Boyd et al., 2002). From microstructure measurements near the North Pole, Fer (2009) found that eddy diffusivity in the central Arctic Ocean is sufficiently weak to allow for maintenance of the CHL. However, the CHL is sensitive to changes in diffusivity, and Fer (2009) estimates that basin averaged vertical eddy diffusivity exceeding $5 \times 10^{-5}\,\mathrm{m^2\,s^{-1}}$ could be enough to erode the halocline.

1.2 Sea Ice

The Arctic Ocean is largely covered by sea ice, preventing efficient energy transfer from the atmosphere to the ocean. Sea ice also works to redistribute salinity in the Arctic Ocean, through the formation, evolution and eventual melt, and has a profound impact on the oceanic boundary layer.

Sea ice contains only a fraction of the salinity found in the sea water from which it is formed. The sea ice is made up of pure ice crystals, interspersed with pockets of high-salinity brine, and is often referred to as a mushy layer (Feltham et al., 2006). The salt addition to the surface waters increases density. If ice production is sufficient, the increasingly dense surface water will finally convect downward. This is typical where sea ice is constantly removed from its formation area, such as the coastal polynyas over the Arctic continental shelves (Winsor and Björk, 2000).

Over time, brine is lost from the sea ice. In sea ice, the pockets of liquid brine are connected through a network of capillaries and brine channels (Petrich and Eicken,

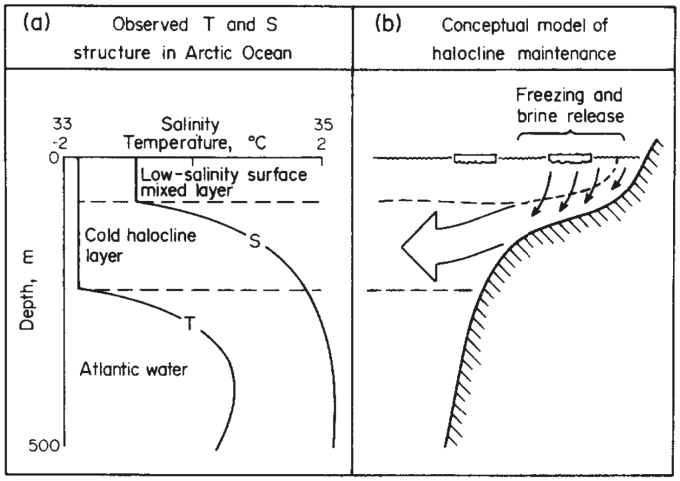

Figure 1.2: Schematic of the temperature and salinity structure in the upper Arctic Ocean, and the maintenance of the cold halocline layer by salt release from ice formation on the continental slopes. From Aagaard et al. (1981).

2010). In winter, low temperatures keeps the ice relatively impermeable, and except for the initial brine rejection at formation, little of the brine is lost before the onset of spring (Griewank and Notz, 2015).

The dominant processes of desalination are gravity drainage, where brine loss increases with ice permeability, and flushing by melt water in summer (Notz and Worster, 2009). Brine density is highest at cold temperatures, so in winter, the brine profile is unstable in the ice. When temperature increases, permeability increases, and the unstable brine can cause convective overturning within the ice. Brine convecting out of the ice can be replaced by underlying seawater. A few indirect observations of gravity drainage have been made around Svalbard; Widell et al. (2006) observed brine plumes descending from landfast sea ice in a Van Mijenfjorden; and possibly two salinity anomalies observed close to the base of the ice in Storfjorden reported by Jardon et al. (2013).

With snow and ice melting at the top of the ice, meltwater accumulates in meltponds. The overhead pressure from meltwater at the surface can cause flushing of the brine channels (Eicken et al., 2004). Meltwater taking the place of brine in the ice not only desalinates the ice efficiently, but also warms the ice throughout (Notz and Worster, 2009). Melt ponds are also important contributors to albedo reduction in summer. Ice roughness affects pond distribution and thus also the ice albedo, and Eicken et al. (2004) found albedo to decrease more for younger ice than for multiyear-ice.

During sea ice melt, small scale processes concerning the molecular diffusivity can be important. The molecular rate of diffusion differs for salt and heat, a feature of sea water known as 'double diffusion'. Notz et al. (2003) documented the formation of 'false bottoms' under the ice, that can play a significant role in the ice-ocean heat budget in

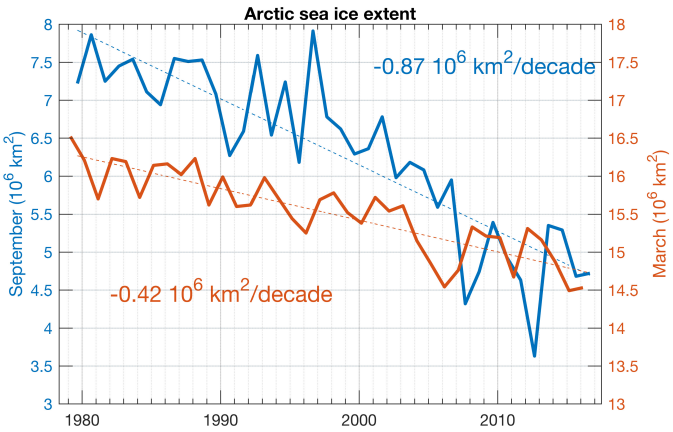

Figure 1.3: Areal extent of Arctic Ocean sea ice as monthly averages at minimum (September) and maximum (March), as measured by satellite since 1979. Linear decadal trends are given based on the full record. Data are from the National Snow and Ice data Center (NSIDC, `https://nsidc.org/`).

summer. False bottoms form by accumulated fresh melt water below sea ice in contact with sea water well below the freezing point of the fresh water. Ignoring doubly diffusive processes during rapid melt can cause underestimation of melt rates, when using a bulk formula based on mixed layer properties. McPhee (2017, p. 153) showed that oceanic heat flux increases super-linearly with thermal forcing in presence of double diffusion, supported by independent estimates of the exchange coefficients for heat and salt from Whaler's Bay (Sirevaag, 2009). There are no clear indications of corresponding double diffusive effects during ice formation (McPhee et al., 2008).

Sea ice drifts in response to the wind forcing (Nansen, 1902). Large scale circulation patterns redistribute sea ice in the basin. The anti-cyclonic Beaufort Gyre concentrates sea ice in the Canada Basin, and towards the coast of Greenland and Canada, and the transpolar drift drives sea ice across the Arctic Ocean, and is resulting in the significant export of sea ice through the Fram Strait (Aagard and Carmack, 1989). Increased atmospheric forcing has caused a spin-up of the Beaufort Gyre in recent decades, responsible for accumulation of freshwater in the gyre through Ekman pumping (McPhee, 2013).

The transition zone from the pack ice to open water is known as the marginal ice zone (MIZ). The location of the ice edge is largely determined by the ocean heat flux convergence at any location (Bitz et al., 2005). In the Eastern Arctic, the AW inflow largely explains the typically low sea ice extent in the Barents Sea (Årthun et al., 2012; Onarheim et al., 2015) and north of Svalbard (Onarheim et al., 2014). In summer, oceanic heat flux is enhanced by insolation, which along with surface melt causes roughly a halving of the sea ice area in September compared to March (Figure 1.3).

The last few decades have brought tremendous changes to the Arctic (Carmack et al.,

2015). Since satellite observations started in 1979, the annual minimum sea ice extent has shrunk from $7.4 \times 10^6\,\mathrm{km}^2$ in the first decade of the record, to $4.8 \times 10^6\,\mathrm{km}^2$ averaged over the last 10 years (Figure 1.3). A synthesis data set of sea ice area extending back to 1850 shows no precedence of the recent minima in sea ice extent (Walsh et al., 2016). A decrease is observed in all months, but the trend is twice as steep in summer (September, $-0.87\ 10^6\ \mathrm{km}^2\ \mathrm{decade}^{-1}$) compared to winter (March, $-0.42\ 10^6\ \mathrm{km}^2\ \mathrm{decade}^{-1}$). The trend in sea ice extent is steepening, in part linked to a preferential loss of old multi-year ice (Serreze and Stroeve, 2015). The loss of old, thick ice and reduced sea ice concentration has led to an increase in drift speed (Rampal et al., 2009; Spreen et al., 2011). Most recently, Polyakov et al. (2017) reported an "atlantification" of the Eurasian Basin, with a weakened halocline and shoaling of the AW layer, which they relate to the most recent reductions in sea ice extent in the eastern Eurasian Basin. The area where the surface mixed layer interacts directly with the AW layer has increased, which might have a significant impact on maintaining the CHL. The changes observed in the Arctic have been taken as indications of a shift to a new normal state (Jeffries et al., 2013).

1.3 Mixing in the Arctic Ocean

1.3.1 Air-Ice-Sea Interactions

The presence of sea ice modulates the exchange of heat, mass and momentum between the atmosphere and the ocean. Solar radiation is a major heat source for the upper ocean in summer (Maykut and McPhee, 1995; Shaw et al., 2009). From observations made in nine transpolar drifts, Stanton et al. (2012) showed that the solar radiation entering the upper ocean was sufficient to support observed ocean-ice interface heat fluxes, and that year-to-year variability was largely explained by variation in open water fraction.

The high reflectivity (albedo) of snow and sea ice compared to the ocean means that sea ice reduces the amount of solar radiation input to the ocean. More heat absorbed by the ocean results in further ice melt, as a positive feedback effect (Curry et al., 1995). The ice-albedo feedback and is one of the reasons for Arctic amplification of climate change (Laîné et al., 2016). It has been speculated whether the Arctic sea ice cover has passed a tipping point (Lindsay and Zhang, 2005), but recovery mechanisms, such as efficient heat loss from open water in fall, and the much higher growth rate of thin ice, speaks against irreversible loss of the summer sea ice (Tietsche et al., 2011).

Momentum transfer from atmosphere to ocean varies greatly with seasonal changes in sea ice extent. Records of ocean heat flux below sea ice are typically dominated by events (e.g., Cole et al., 2014; McPhee, 1992). The presence of a rigid sea ice cover can prevent significant mixing, even during strong storms. In ice-free periods, however, storms can drive strong inertial currents, thus deepening the surface mixed layer (Rainville and

Winsor, 2008). In a study of coastal upwelling in the Beaufort Sea, Schulze and Pickart (2012) found the strongest response during partial ice cover, weaker both under ice-free conditions and full ice cover. Martini et al. (2014) found a strong seasonality in generation and decay scales of near-inertial internal wave field from yearlong mooring observations, and identified an optimum ice concentration of 80-90% leading to threefold amplification of momentum transfer. Energy transfer from the atmosphere was efficient during the ice-free summer, while oscillations were weaker and dampened by the ice cover in winter. Dampening time scales were longer in early winter, while the ice was still mobile, reducing in later winter when the ice cover was more rigid. Momentum transfer to the ocean increases with ice concentration due to the drag of freely moving sea ice keels (Pite et al., 1995; Skyllingstad et al., 2003), but decreases when concentrations are too high because of internal stress between floes. Younger, thinner sea ice is smoother, and gives less drag, and tends to reduce ocean surface stress (Martin et al., 2016), consistent with the observations of Schulze and Pickart (2012) and Martini et al. (2014).

Freshwater from sea ice melt can also have profound effect on heat and momentum transfer, as increased stratification inhibits mixing. Drifting over a fresh surface layer during the Marginal Ice Zone Experiment (MIZEX), Morison et al. (1987) reported generation of internal gravity waves as surface stratification increased. This effectively increased momentum transfer from the ice, feeding the internal wave field, and caused heat flux at the ice-ocean interface to decrease. The generation mechanism of internal waves by sea ice was supported by a subsequent modeling study (McPhee and Kantha, 1989).

1.3.2 Internal Wave Energy

In the ocean interior, vertical mixing is primarily driven by breaking of internal waves, typically generated by winds at the surface or by tidal currents over bottom topography. While much of the wind energy input to the ocean goes directly to mixing of the upper layer, some energy propagates deeper in the water column as near-inertial waves. Dohan and Davis (2011) observed contrasting response in the pycnocline during mid-latitude two storms, with steady deepening in response to wind stress in the first, while the other storm excited resonant near-inertial waves. The wave energy may propagate away from its origin, and induce mixing where the waves eventually break (Alford et al., 2016). While low-mode near-internal waves have been observed to propagate far at lower latitudes (Alford, 2003), observations have indicated that near-inertial internal waves in the Arctic are dissipated effectively against the sea ice boundary (Morison et al., 1985; Pinkel, 2005).

Numerous field observations has classified the Arctic Ocean as a ‘low-energy ocean’. From a five day thermistor string time series, Levine et al. (1985) reported less energetic

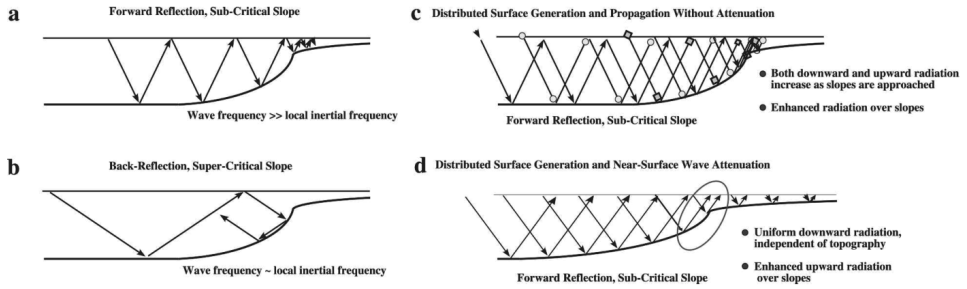

Figure 1.4: Scenarios for shoaling internal waves. Sufficiently high frequency waves are (a) forward reflected and buily up energy as they approach the shore, or (b) are back-reflected against a super-critical slope. For uniformly distributed generation at the surface (c) without and (d) with attenuation at the surface. From Pinkel (2005).

internal wave field than that typical at mid-latitudes, although with a spectral shape consistent with the Garrett-Munk model (Garrett and Munk, 1975). Fine-scale velocity shear and temperature profiles revealed an internal wave field 1-2 orders of magnitude less energetic than typical at mid-latitudes (Levine et al., 1987). From expendable current profilers D'Asaro and Morison (1992) found low background diffusivity, but also a highly variable internal wave field, indicating that internal wave mixing could play a major role in vertical heat transport in the Arctic. Pinkel (2005) found a weak near-inertial wave field in the Canada Basin during the yearlong Surface Heat Budget of the Arctic project. Separating down- and upward propagating wave groups, he found that downgoing waves were distributed relatively uniformly over the basin, while for upward propagating wave groups variance related inversely with depth. Rather than unattenuated reflection (Figure 1.4a-c), leading to cross-Arctic propagation, the dominant dissipation in the under-ice boundary layer and lack of correlation between downward propagating energy and location or depth point to a "one-bounce" regime in the Arctic Ocean (Figure 1.4d).

Breaking internal tidal waves can bring heat from the Atlantic Water towards the surface. While tides generate little mixing in the Central Arctic, numerous hotspots of enhanced currents, elevated sea level amplitudes and phase variability have been identified along the Arctic continental slope (Kowalik and Proshutinsky, 1993; Rippeth et al., 2015). One such region is the Chukchi Borderlands in the western Arctic, where Shaw and Stanton (2014) found that diffusivities elevated by one order of magnitude compared to interior Canada Basin, where diffusion was on molecular levels. The enhanced diffusivities is linked to turbulence and internal wave activity interaction with topography. In the Laptev Sea, Lenn et al. (2011) found elevated dissipation rates of turbulent kinetic energy, related to tidal interaction with the continental slope.

Another region of particular interest is the Yermak Plateau (YP), where significant

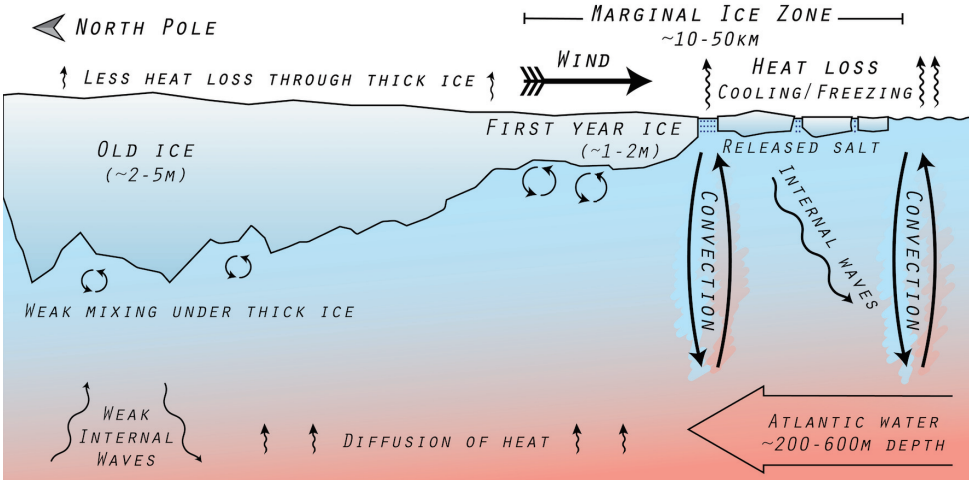

Figure 1.5: Illustration of mixing processes in winter, in the "old Arctic", dominated by thick multi-year sea-ice. Atlantic water enters to the right in the figure, red colors representing warmer water. In the marginal ice zone surface waters are cooled, and subsequently frozen, and convection results from the cooling and brine release during freezing. In the marginal ice zone storms may mix the upper ocean, or generate near-inertial internal waves. Thicker ice reduces the effect of wind and cooling. Adapted from Peterson (2016).

internal wave production has been observed (D'Asaro and Morison, 1992; Fer et al., 2015; Plueddemann, 1992), and has been linked to response of strong tidal currents over the bottom topography (Padman et al., 1992). Current measurements by Hunkins (1986) clearly indicated stronger diurnal currents over YP and slope compared to further off-slope. In the 2002 NPEO drift, buoys drifting over YP showed that large mixed layer temperature elevation above freezing and heat flux coincided with shallow bathymetry and energetic tides (McPhee et al., 2003). A model study shows that enhanced dissipation and loss of heat from AW should be expected in regions of shallow and complex topography (Holloway and Proshutinsky, 2007). Fer et al. (2010) found variability in internal-wave activity and mixing related to topography and hydrography in the southern YP, indicating that the path of the WSC will affect the cooling and freshening of the Atlantic inflow.

1.3.3 Mixing in the "New Arctic"

With a reduced ice cover, the under-ice energy dissipation is expected to reduce, and wind forcing increase, leading to a more energetic internal wave field (Figure 1.6). At the same time, increasing run-off due to the accelerated hydrological cycle will increase stratification and may counter the effects of enhanced energy input (Nummelin et al., 2016).

From moored observations in the Chukchi Sea, Rainville and Woodgate (2009) found a significant increase in near-inertial currents in the ice free months, even though storms occurred throughout the seasons. Significant enhancement of wind-driven near-inertial shear in the absence of ice cover has also been reported from the Laptev Sea (Lenn et al., 2011). From nearly a decade of ice-tethered profilers in the Canada Basin, Dosser et al. (2016) reported a seasonal cycle in the near-inertial wave field, with maxima at summer's minimum sea ice extent and in early winter when wind forcing peaks. The record also reveals a weak increasing trend in response to the declining sea ice cover. From a yearlong data set of ice-tethered profilers in the Canada Basin, Cole et al. (2014) found that near-inertial wave energy was not constant in time, with elevated internal wave shear in the winter months.

Studies have also reported on the importance of individual storm events on internal wave generation. Following two wind events, Merrifield and Pinkel (1996) observed upward and downward propagating near-inertial internal waves in the Beaufort Sea. In the Central Arctic, Fer (2014) observed near-inertial oscillations, likely generated by a preceding storm. The near-inertial frequency band displayed a dominant clockwise rotation, and led to elevated dissipation rates in the pycnocline. From their yearlong ITP data set in the Beaufort Sea, Cole et al. (2014) could also identify packets of internal waves with downward energy propagation in response to changing wind forcing.

Guthrie et al. (2013) compared recent studies of internal waves and mixing to data from historic studies. They found no discernible trend in near-inertial wave energy over 30 years, while sea ice extent has declined rapidly in the same period. They hypothesize that increased surface stratification in the same period has caused internal wave boundary layer dissipation to increase correspondingly.

Recently, Lincoln et al. (2016) analyzed data from the Canada Basin from the extraordinary summer of 2012, with an unprecedented minimum in sea ice extent, and unusually high storm activity. Despite enhanced internal wave energy associated with the ice-free conditions, no significant elevation of mixing levels at intermediate depths were observed away from topography. This implies that the stratification in the Canada Basin continues to suppress vertical mixing.

Carmack et al. (2015) summarized the observed changes in the Arctic sea ice cover, including the reduced ice extent and thickness, and the increasing drift speed and duration of the melt season. They highlight the need to quantify processes relating to the contribution of oceanic heat in heat budgets as the changes progress. In their suggested research strategy, the need for improved mapping of heat loss from AW, and need for process studies to improve our conceptual understanding of heat exchange in the Arctic Ocean, including the generation and propagation of internal waves, are emphasized.

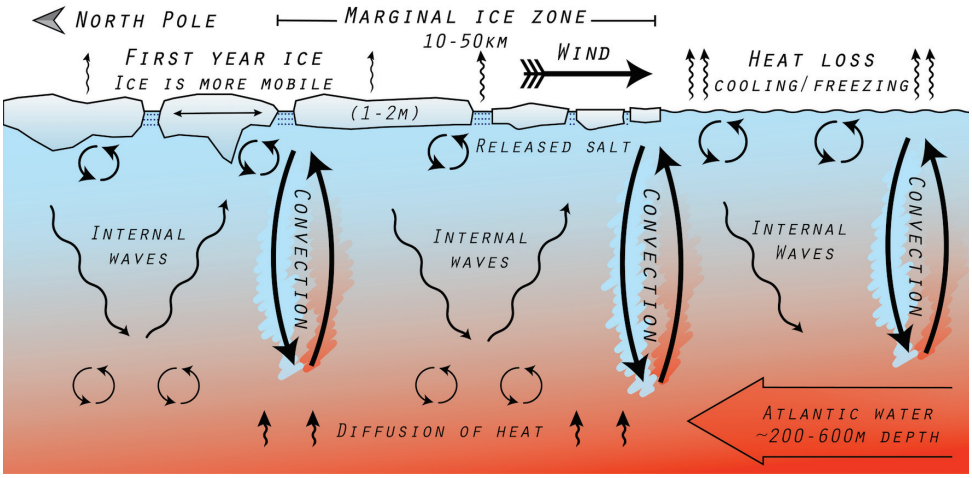

Figure 1.6: Winter in the "new Arctic", where the Atlantic water is warmer than before, and the thick, old sea ice is largely replaced by thinner, young sea ice. The young sea ice is more mobile; it moves more easily with the wind, and is more vulnerable to ice break-ups. Cooling and freezing leads to convection further into the Arctic Ocean, and wind-forced mixing may occur in larger parts of the Arctic. Adapted from Peterson (2016).

Chapter 2

This study

2.1 Objectives

This study is part of the project "On Thin Ice: Role of Ocean Heat Flux in Sea Ice Melt" (NICE), funded by the Norwegian research council (NFR project 229786). My research aim has been to study the role of ocean heat flux and turbulent mixing in the changed Arctic. Among the main research questions has been whether the shift from predominantly old, thick sea ice to thinner first-year sea ice has affected oceanic mixing and air-ice-sea interactions. The study also aimed to investigate the effect of a seasonal ice cover on near-inertial internal wave energy. Focus has been on vertical mixing of Atlantic water towards the surface, for which the inflow region around the Yermak Plateau is a very suitable location. From turbulence measurements near the ice-ocean interface to full depth moorings, I have addressed mixing processes on different spatial and temporal scales. A key question assess and quantify the role of oceanic heat in the heat budget at the ice-ocean interface. The unique data set collected during N-ICE2015 (Section 2.2.1) has allowed us to study mixing processes over the deep basin in winter, quantifying the differences between stormy and quiescent forcing conditions.

2.2 Field work

This study is based on two field campaigns, both focused on the region north of Svalbard, over the Yermak Plateau and the surrounding slopes and deep ocean (Figure 2.1). First presented here is the drift campaign of the Norwegian Polar Institute in January to June 2015, named the Norwegian Young Sea Ice Experiment (N-ICE2015, Section 2.2.1). Second, three moorings were deployed on the slope of the Yermak Plateau, covering the inflow region of Atlantic Water between September 2014 to August 2015 (Section 2.2.2).

2.2.1 Norwegian Young Sea Ice Cruise (N-ICE2015)

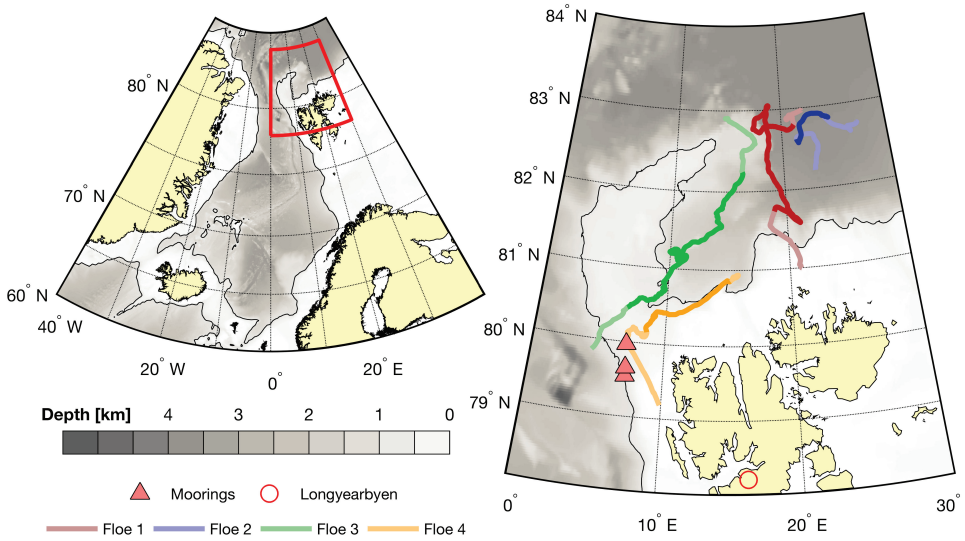

Figure 2.1: Map overview of the field work. The red box in (a) outlines the area shown in (b). Depth is indicated by the shading, with a black isoline at 1000 m. Drift tracks of N-ICE2015 are shown in separate colored lines, stronger colors indicate parts of the drift covered by TIC measurements.

Figure 2.2: N-ICE2015 project logo.

In January 2015, the R/V Lance set out from Longyearbyen to be frozen into the sea ice north of Svalbard. The objective of N-ICE2015 is to understand how the rapid shift to a younger and thinner sea ice regime in the Arctic affects energy fluxes, sea ice dynamics and the ice-associated ecosystem, as well as local and global climate. With the ship as a base, scientists collected data from ocean, atmosphere, sea ice, snow and biology from the drifting ice floe. On the ocean side, data sets of currents, hydrography and turbulence were collected throughout the campaign, covering both the deep basin and continental slope, as well as the seasonal span from winter to early summer.

The southwestward drift of the ice camp was accelerated by several storms (Cohen et al., n.d.), and the ship was repositioned three times. The drifts are termed Floes 1 to 4, shown on the map in Figure 2.1 and detailed in Table 2.1.

The overlap of the N-ICE project with my own project in both time and scientific aims merited my participation in the drift, which turned to be a central part of my study. I took part in the second leg of the drift, lasting from mid February through March. The main contribution from my part was the turbulence instrument cluster (TIC), which was the key data set for Paper I and III, described below.

	Floe 1	Floe 2	Floe 3	Floe 4
Date start	15 Jan	24 Feb	18 Apr	7 Jun
Latitude start	83.2°N	83.0°N	83.2°N	81.1°N
Longitude start	21.6°E	27.4°E	13.5°E	14.4°E
Date end	21 Feb	19 Mar	5 Jun	22 Jun
Latitude end	81.2°N	82.5°N	79.9°N	80.1°N
Longitude end	20.3°E	22.6°E	3.1°E	5.7°E
Drift distance	516 km	243 km	609 km	375 km

Table 2.1: Drift details for N-ICE2015.

Turbulence instrument cluster

A turbulence instrument cluster (TIC) is a suite of instruments mounted on a mast, designed to make high frequency point measurements of a small volume of water (Figure 2.3). The TIC consists of SeaBird Electronics temperature (SBE3F) and conductivity (SBE4) sensors, and a Sontek Acoustic Doppler Velocimeter (ADV), which are connected to a common SBE 9plus underwater unit ("fish"). A compass and a pressure gauge are also connected to the "fish", which in turn reports the data to a computer through a SBE 911 deck unit at the surface.

During N-ICE2015, a mast holding two TICs were deployed through a hole in the ice on all four floes, set up to sample at 1 m and 5 m below the ice undersurface. On Floe 1, a mast setup by the NPI was used, where the mast was deployed on a fixed mast, where each of the TICs were manually rotated to face the flow. During retrieval in February, the mast was unfortunately severely damaged, and could not be used for the remainder of the campaign. On Floes 2-4, a slightly different setup, provided by Miles McPhee was used. The mast was suspended on a wire, connected to a mechanic winch on a derrick, allowing simple adjustment of the mast depth. The hydrohole was covered with styrofoam to prevent substantial refreezing, and the derrick was covered by a tarp to protect the hole from the weather.

Originally, the McPhee TIC was planned be used as a supplement to the NPI mast, which would facilitate e.g. investigation of horizontal variability, and sampling at four depths simultaneously. When this was not possible, we decided to maintain sampling at 1 m and 5 m for consistency throughout. Much of the current measurements at 5 m, however, turned out to be of poor quality, and the study has focused on the measurements nearest the ice-ocean interface.

N-ICE2015 list of publications

The initial round of publications which resulted from the project were all submitted to Journal of Geophysical Research to be part of a special section. My contributions

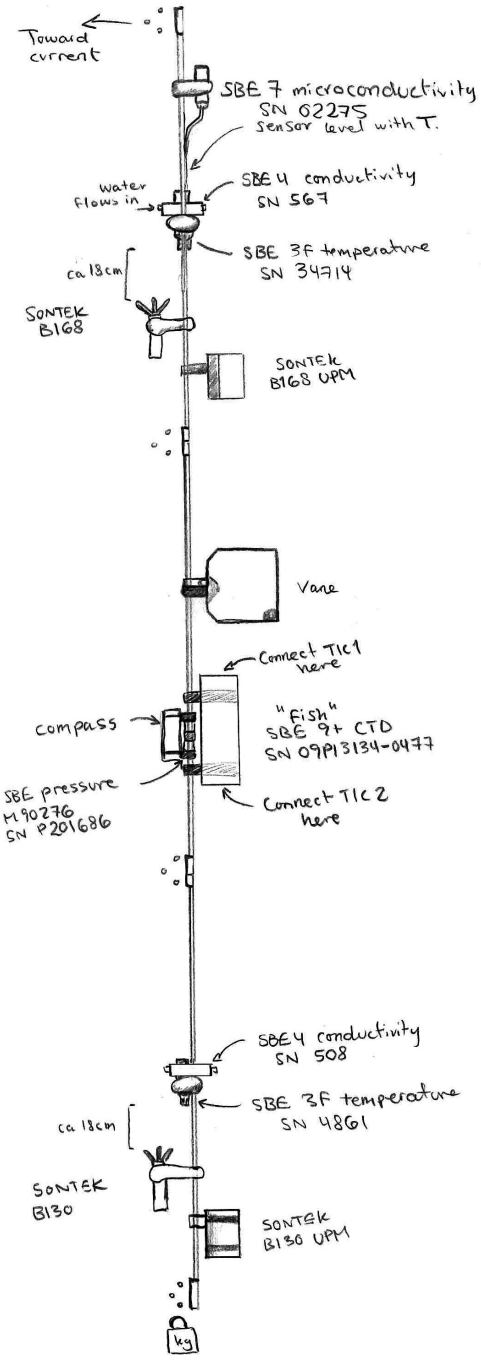

Figure 2.3: Sketch of the TIC setup. The turbulence cluster (TIC) hold conductivity (SBE4), temperature (SBE3F) and current (Sontek ADV) sensors. The upper TIC also has a micro-conductivity sensor (SBE7). The mast also holds a compass and a pressure gauge. All instruments are connected to a SBE 9plus underwater unit ("fish"), which in turn is connected to a SBE911 deck unit. The vane helps the freely rotating mast to keep instruments directed into the current.

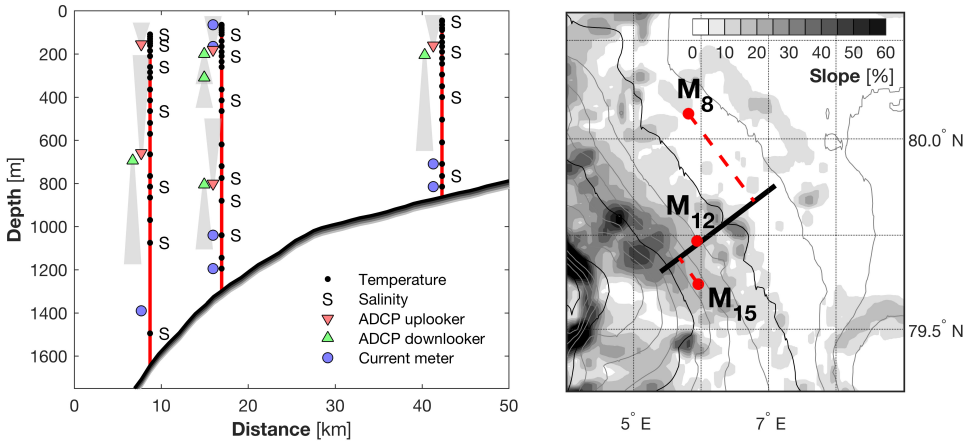

Figure 2.4: Overview of the mooring array. The distribution of instruments on each of the three moorings is indicated over the slope in (a), where the moorings are projected along isobaths onto the cross-section shown in (b). Shading in (b) reflects the local topographic slope, calculated from ETOPO-1 bathymetric data.

to these are listed in Chapter 3. An updated list of publications in the N-ICE2015 special section can be found at `http://onlinelibrary.wiley.com/10.1002/(ISSN)2169-9291/specialsection/NICE1`

2.2.2 Moorings

Three moorings were deployed on the slope of the Yermak Plateau by coast guard vessel KV Svalbard, north west of Svalbard (Figure 2.1). The moorings were placed on a north-south line at depths of 863, 1327 and 1609 m, covering the core of the West Spitsbergen Current. Deployment lasted from September 2014 to August 2015.

The moorings were densely equipped with instruments (Figure 2.4), designed to resolve near-inertial internal waves. All instruments sampled at 1 h frequency or faster, and were gridded to a 1 h and 5 m grid.

The experiment was designed to deploy the moorings well into the pack ice, relying on the ice-strengthened vessel. The intention was to have the moorings in seasonally ice covered waters, to assess internal wave energetics under varying ice cover. Local sea ice conditions north of Svalbard in August 2014 prevented deployment further into the region of seasonal ice cover. Because of this, the moorings were not entirely ice covered during the winter, and could not be used to assess seasonal changes relating to presence and absence of complete sea ice cover.

Chapter 3

Introduction to the papers

Paper I: **Turbulent heat and momentum fluxes in the upper ocean under Arctic sea ice**

Algot K. Peterson, Ilker Fer, Miles G. McPhee, and Achim Randelhoff (2017), Journal of Geophysical Research - Oceans, 122, doi: 10.1002/2016JC012283.

In this paper we investigate turbulent fluxes in the ice-ocean boundary layer from the N-ICE drift north of Svalbard, and relate temporal and spatial variations to changing wind forcing, ice conditions and bathymetry as the ice drifts. Away from topographic features in winter we find weakly positive turbulent heat fluxes, and observe a rough doubling during storms. From drift over one point separated approximately one week in time we observe an elevation in the mixed layer indicating a vertical mixing process - further explored in Paper II. In spring, coinciding with drift closer to the marginal ice zone and Atlantic Waters, heat fluxes are 1-2 orders of magnitude greater than in winter. Storms passing concurrent with warm water near the surface drive the highest fluxes, on the order of 100 W m^{-2} over several hours. Direct measurements of heat fluxes agree well with a common parametrization, except for two occasions, where we hypothesize that influx of fresh water from ice melt causes the bulk formula to overestimate heat flux. The heat- and salt fluxes during the last floe are further explored in Paper III. An additional component we studied was the free drift force balance, which is not included in the paper, but can be found in Appendix A.

Paper II: **One-dimensional preconditioning of the upper Arctic Ocean water column during winter**

Ilker Fer, Algot K. Peterson, Achim Randelhoff, and Amelie Meyer (2017), Journal of Geophysical Research: Oceans, 122, doi: 10.1002/2016JC012431.

This is a study of upper ocean winter-time hydrographic data from drift over the deep Nansen basin, and hypothesize that observed changes are caused by vertical mixing

processes. Applying a one-dimensional model forced by vertical diffusion equations for temperature and salinity, we are satisfactorily able to reproduce observed changes for two pairs of profiles. Results are sensitive to the profiles of vertical diffusivity, which were synthesized from observed microstructure profiles from the same drift. Salinity increase in the mixed layer is dominated by entrainment of saline water from below (90%), rather than brine rejection from ice formation (10%).

Paper III: **Observations of brine plumes below Arctic sea ice**
Algot K. Peterson, Ocean Science Discussions, doi: 10.5194/os-2017-27, under review for Ocean Science.

This paper focuses on a subset of the under-ice turbulence data collected during N-ICE2015, from the marginal ice zone in June. Opposite of expectations during sea ice melt, salt and heat fluxes were anti-correlated; heat was brought upwards while salt flux was downward. I argue that this is caused by brine release from the melting sea ice, most clearly manifested by descending plumes of high-salinity water sinking past the measurement volume. Calculated as an average over a composite structure, the plumes stand for 6% and 9% of heat- and salt fluxes over only lasting 0.5% of the time. The accumulated salt fluxes indicate a nearly full desalination of the sea ice as it decays in the marginal ice zone. Bulk salinity reduction in two nearby ice cores agree with accumulated salt fluxes to within a factor of two. Similar plumes have previously been observed from land-fast ice in a Svalbard fjord, and this study confirms that the process is also present in drifting Arctic sea ice.

Paper IV: **Near-inertial band variability from one-year duration moored measurements near Yermak Plateau**
Algot K. Peterson and Ilker Fer, manuscript in preparation.

From three moorings deployed on the western slope of the Yermak Plateau for one year, we study the near-inertial wave field. Near-inertial energy is elevated in sporadic events, particularly near the surface, but also at intermediate depths and near bottom. Currents rotate in a dominantly clockwise fashion with depth, indicating downward propagation. The clockwise dominance is greatest closer to surface, consistent with surface generation by wind. We find that both wind and tidal interaction with topography are important for generation of near-inertial internal waves in the region. We identify packets of downward propagating near-inertial internal waves, and calculate their wave properties. Tidal analysis reveals significant diurnal K_1 and semidiurnal (near-inertial) M_2 components, and several tidal ellipses directed on-slope. Calculated paths of near-inertial beams radiating from the shelf break are consistent with elevated near-inertial kinetic energy at

intermediate depths.

Additional contributions

- Fer, Ilker, M. Müller, and **Algot K. Peterson**. 2015. *"Tidal Forcing, Energetics, and Mixing near the Yermak Plateau."* Ocean Science 11 (2): 287–304. doi: 10.5194/os-11-287-2015.

- Fransson, Agneta, Melissa Chierici, Ingunn Skjelvan, Are Olsen, Philipp Assmy, **Algot K. Peterson**, Gunnar Spreen, and Brian Ward. 2017. *"Effects of sea-ice and biogeochemical processes and storms on under ice water fCO_2 during the winter-spring transition in the high Arctic Ocean: Implications for sea-air CO_2 fluxes."* Journal of Geophysical Research: Oceans, in press. doi: 10.1002/2016JC012478.

- Meyer, Amelie, Ilker Fer, Arild Sundfjord, and **Algot K. Peterson**. *"Mixing Rates and Vertical Heat Fluxes North of Svalbard from Arctic Winter to Spring."* Journal of Geophysical Research, in press. doi: 10.1002/2016JC012441.

- Duarte, Pedro, Amelie Meyer, Lasse M. Olsen, Hanna M. Kauko, Philipp Assmy, Anja Rösel, Polona Itkin, Stephen R. Hudson, Mats A. Granskog, Sebastian Gerland, Arild Sundfjord, Harald Steen, Haakon Hop, Lana Cohen, **Algot K. Peterson**, Nicole Jeffery, Scott M. Elliott, Elizabeth C. Hunke, Adrian K. Turner. *"Sea-Ice Thermohaline-Dynamics and Biogeochemistry in the Arctic Ocean: Empirical and Model Results."* Journal of Geophysical Research - Biogeosciences, accepted for publication.

Chapter 4

Scientific results

I

Paper I

4.1 Turbulent heat and momentum fluxes in the upper ocean under Arctic sea ice

Algot K. Peterson, Ilker Fer, Miles G. McPhee, and Achim Randelhoff

Journal of Geophysical Research – Oceans, **122** (2017), doi:10.1002/2016JC012283.

AGU PUBLICATIONS

JGR

Journal of Geophysical Research: Oceans

RESEARCH ARTICLE

10.1002/2016JC012283

Special Section:
Atmosphere-ice-ocean-ecosystem Processes in a Thinner Arctic Sea Ice Regime: the Norwegian Young Sea ICE Cruise 2015 (N-ICE2015)

Turbulent heat and momentum fluxes in the upper ocean under Arctic sea ice

Algot K. Peterson[1,2], Ilker Fer[1,2], Miles G. McPhee[3], and Achim Randelhoff[4,5]

[1]Geophysical Institute, University of Bergen, Bergen, Norway, [2]Bjerknes Centre for Climate Research, Bergen, Norway, [3]McPhee Research Company, Naches, Washington, USA, [4]Institute for Arctic and Marine Biology, UiT, Arctic University of Norway, Tromsø, Norway, [5]Norwegian Polar Institute, Tromsø, Norway

Abstract We report observations of heat and momentum fluxes measured in the ice-ocean boundary layer from four drift stations between January and June 2015, covering from the typical Arctic basin conditions in the Nansen Basin to energetic spots of interaction with the warm Atlantic Water branches near the Yermak Plateau and over the North Spitsbergen slope. A wide range of oceanic turbulent heat flux values are observed, reflecting the variations in space and time over the five month duration of the experiment. Oceanic heat flux is weakly positive in winter over the Nansen Basin during quiescent conditions, increasing by an order of magnitude during storm events. An event of local upwelling and mixing in the winter-time Nansen basin highlights the importance of individual events. Spring-time drift is confined to the Yermak Plateau and its slopes, where vertical mixing is enhanced. Wind events cause an approximate doubling of oceanic heat fluxes compared to calm periods. In June, melting conditions near the ice edge lead to heat fluxes of O(100 W m^{-2}). The combination of wind forcing with shallow Atlantic Water layer and proximity to open waters leads to maximum heat fluxes reaching 367 W m^{-2}, concurrent with rapid melting. Observed ocean-to-ice heat fluxes agree well with those estimated from a bulk parameterization except when accumulated freshwater from sea ice melt in spring probably causes the bulk formula to overestimate the oceanic heat flux.

Key Points:
- Unique winter and spring measurements of under-ice turbulence characteristics in the Eastern Arctic
- Winter oceanic turbulent heat flux toward ice is O(1) W m^{-2} in deep Arctic
- Under-ice heat fluxes are O(100) W m^{-2} near Atlantic Water pathways

Correspondence to:
A. K. Peterson,
algot@uib.no

Citation:
Peterson, A. K., I. Fer, M. G. McPhee, and A. Randelhoff (2017), Turbulent heat and momentum fluxes in the upper ocean under Arctic sea ice, *J. Geophys. Res. Oceans*, *122*, doi:10.1002/2016JC012283.

Received 26 AUG 2016
Accepted 24 JAN 2017
Accepted article online 31 JAN 2017

1. Introduction

Ocean heat is a key factor in the heat budget of Arctic sea ice, and small changes in oceanic heat transport can have a substantial influence on the sea ice cover [*Carmack et al.*, 2015]. Summer sea ice extent is declining increasingly fast [*Serreze and Stroeve*, 2015], and what was once a thick, perennial ice cover has now been replaced by thinner first-year ice [*Krishfield et al.*, 2014; *Lindsay and Schweiger*, 2015]. The Arctic seems to have shifted to a new normal state [*Jeffries et al.*, 2013], and we are facing essentially ice-free summers [*Stroeve et al.*, 2012]. With a seasonally ice-free Arctic, a stronger seasonality in heat exchange between the upper ocean and ice/atmosphere is expected [*Tietsche et al.*, 2011]. A reduced ice cover may lead to increased energy input from direct wind forcing to the upper ocean [*Rainville et al.*, 2011].

In the interior Arctic, turbulent heat exchange is limited by the cold halocline layer [*Fer*, 2009], and heat transfer is dominated by individual events [*Fer*, 2014]. The warm boundary currents in the Eastern Arctic, however, are associated with turbulent oceanic fluxes elevated by up to two orders of magnitude [*Sirevaag and Fer*, 2009]. The marginal ice zone (MIZ) is often located over the Yermak Plateau (YP), a manifestation of large oceanic heat loss to melting ice along the path of Atlantic Water (AW) north of Svalbard. Although large regional and seasonal variability in ocean heat flux has been observed, the contribution and importance of the oceanic heat for the variability of the sea ice cover is still not accurately quantified [*Carmack et al.*, 2015].

A few major experiments have shed light on the heat budget of the Arctic sea ice cover. From the 1975 Arctic Ice Dynamics Joint Experiment (AIDJEX), *Maykut and McPhee* [1995] demonstrated the strong seasonal cycle in oceanic heat flux and found solar radiation to be the major source of upper ocean heat in the central Arctic. During the yearlong drift of SHEBA (Surface Heat Budget of the Arctic) over the western Arctic, ocean-to-ice heat flux was low to moderate (~3.5 W m^{-2}) in the first parts of the record, reflecting

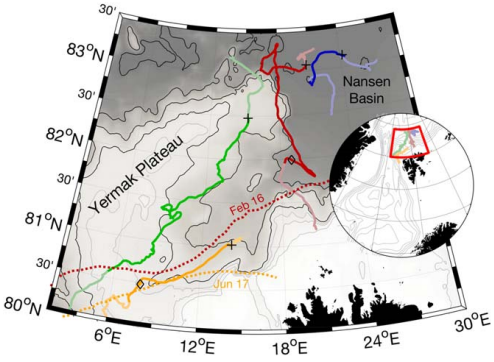

Figure 1. Map of the study area, north of Svalbard, as shown in the inset. Drift track is shown in faint colors, and track covered by TIC sampling in clear colors. Each color represents one drift, and is consistent with following figures. Crosses mark the start of TIC sampling. Bathymetry is from ETOPO-1, with isobaths at 1000 m intervals in black, and at 250 m intervals for depths shallower than 1000 m in gray. Lines for 50% sea ice concentration are shown for two dates (marked by diamonds on the track), based on satellite data acquired from the Norwegian Meteorological Institute.

variations in bathymetry and stratification. Solar heating of the upper ocean was the dominant heat source during the summer part of the drift [*Shaw et al.*, 2009]. *Hudson et al.* [2013] observed significant contribution of oceanic heat flux to the energy budget of melting first-year ice in the Nansen Basin. In spring and summer when the radiation forcing is strong, it is challenging to quantify the oceanic contribution to the energy balance. In winter, on the other hand, when the sole source of heat is the oceanic heat, it is possible to quantify the vertical flux of heat from the ocean interior.

Winter observations in the Arctic are sparse, and the most notable exceptions, AIDJEX and SHEBA, were both from the central western Arctic. More typical field campaigns in the Arctic are drift stations in the marginal ice zone in spring, lasting a few days or less [*Sirevaag and Fer*, 2009]. In recent years, autonomous measurement systems have proven useful in for long-term measurements of Arctic Ocean momentum and heat fluxes in the Canada Basin [*Cole et al.*, 2014; *Gallaher et al.*, 2016] and along the transpolar drift [*Shaw et al.*, 2008; *Stanton et al.*, 2012].

Here we present approximately two months duration measurements of directly measured heat and momentum fluxes, sampled from four consecutive drift stations north of Svalbard, spanning from January to June 2015. The drift trajectories cover the deep Nansen Basin, the shelf break, and the YP. In the Nansen Basin, conditions are typical of the central Arctic, while the MIZ and the presence of the inflowing warm AW dominate when the drift is over topography. The main purpose of this paper is to describe the under-ice boundary layer conditions encountered during the drifts. Furthermore, we assess the relative importance of oceanic heat flux in winter versus spring, and contrast measurements from the Arctic basins versus over the boundary current and topographic features.

2. General Description of the Experiment

2.1. Ice Camp Floes

As a part of the Norwegian Young Sea Ice Cruise project (N-ICE2015) [*Granskog et al.*, 2016], the research vessel (RV) Lance conducted multiple drifts from January through June 2015 in the sea ice north of Svalbard. A total of four subsequent ice camps were supported by the RV Lance (Figure 1), hereinafter referred to as Floes 1–4. Floes 1 and 2 were typically confined to the deep Nansen Basin, starting their southward drift from approximately 83°N. Floe 3 drifted southwest over the eastern flanks and then across the Yermak Plateau (YP), whereas Floe 4 started its drift closer to the continental slope north of Spitsbergen and proceeded over to the southern parts of the YP. Durations of the four ice floes were 38, 23, 49, and 15 days, respectively, 126 days in total. The first two floes can be considered winter conditions, Floe 3 covers spring and Floe 4 was early summer conditions. Floe 1 drifted in complete darkness, and on 1 March, the sun rose after four and a half months of polar night at 83°N. Five weeks after the first sunrise, on 5 April, was the onset of midnight sun.

At each floe, a turbulence instrument cluster (TIC, section 3.1) measurement system was established. The measurements from the TICs constitute the main data set of this study. The details of the TIC coverage for each floe are given in Table 1 and highlighted in colors in Figures 1 and 2.

Table 1. TIC Deployment Details for the Four Floes[a]

	Start Date	Start Position	End Date	End Position	Duration (h)	Distance (km)
Floe 1	Jan 24	83°4′N, 20°43′E	Feb 17	81°57′N, 018°8′E	524	349
Floe 2	Mar 4	83°8′N, 24°14′E	Mar 15	82° 53′N, 020°55′E	155	89
Floe 3	Apr 26	82°29′N, 15°6′E	Jun 2	80°34′N, 005°32′E	892	406
Floe 4	Jun 10	81°1′N, 14°10′E	Jun 19	80°15′N, 007°21′E	200	175

[a]Date is in 2015. Duration is length of TIC data coverage, prior to quality screening.

2.2. Environmental Conditions

In the following, storms are defined as by L. Cohen *et al.* (Meteorological conditions during the Norwegian Young Sea Ice (N-ICE) experiment, submitted to *Journal of Geophysical Research*, 2017), and are indicated by horizontal bars in Figure 3b. Start and end of storms correspond to periods when the 10 min averaged wind speed at 10 m height (U_{10m}) was greater than 8 m s^{-1} for more than 3 h, with no interruptions exceeding 1 h. A storm is classified as "major" when the rate of pressure decrease exceeds 5 hPa in 6 h. Wind measurements from the on-ice weather-mast are supplemented by ship-based measurements, adjusted to the 10 m measurement height [*Hudson et al.*, 2015; L. Cohen *et al.*, submitted manuscript, 2017].

Drift velocity, U_{ice}, is calculated from the ship's GPS position (Figure 3c). U_{ice} includes the signature of inertial and tidal oscillations. Because the near-surface water column typically oscillates approximately in phase with the ice, the instantaneous U_{ice}, or the shear between the ice drift and measured ice-relative current in the surface layer, is not representative of turbulence production. Therefore, following *McPhee* [1988], we also present the filtered (demodulated with diurnal and semidiurnal, approximately inertial, frequencies) drift speed together with the average measured ice-relative current at 1 m below the ice undersurface.

The drift of Floe 1 was mostly over the abyssal Nansen Basin. Winds measured at 10 m height were modest (5.1 m s^{-1} average) and ice drift slow (8 cm s^{-1}) during the first 10 days of the measurements. On 3 February, a storm pushed the ice northward, compacting the ice for 2 days, before the wind turned, and flushed the floe southward until the end of the storm on 9 February. During the 5.4 day longstorm (mean $U_{10m} = 12$ m s^{-1}, $U_{ice} = 28$ cm s^{-1}), the floe traveled 136 km. For comparison, total drift over the 10.5 days prior to the storm was 72 km. During the swift southward drift, the floe passed the eastern tip of the YP, with water depths shoaling to 1600 m before entering deeper water between the plateau and the Svalbard shelf (Sofia Deep). In mid-February, another storm brought strong winds and high drift speed and led the floe further south. The floe broke up, and TIC logging terminated before the floe drifted onto the Svalbard shelf.

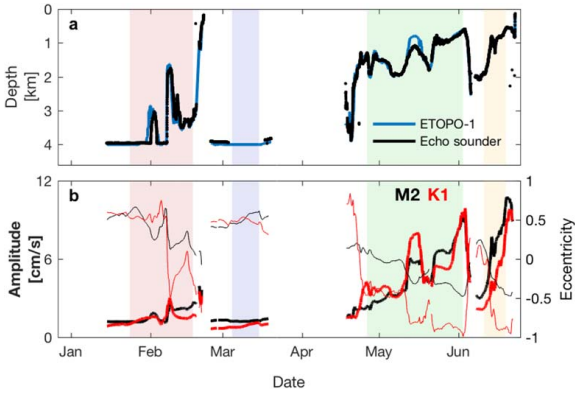

Figure 2. Time series of water depth and tidal currents. (a) Water depth from the ship's echo sounder (blue) and ETOPO-1 bathymetry (black). During most of Floe 2 the echo sounder was covered by ice. (b) Tidal parameters from AOTIM-5 [*Padman and Erofeeva*, 2004] along the ship track; major tidal ellipse amplitudes and eccentricity (thin line) for M_2 (black) and K_1 (red) tidal constituents. Shading indicates data coverage of the TIC, colors following Figure 1.

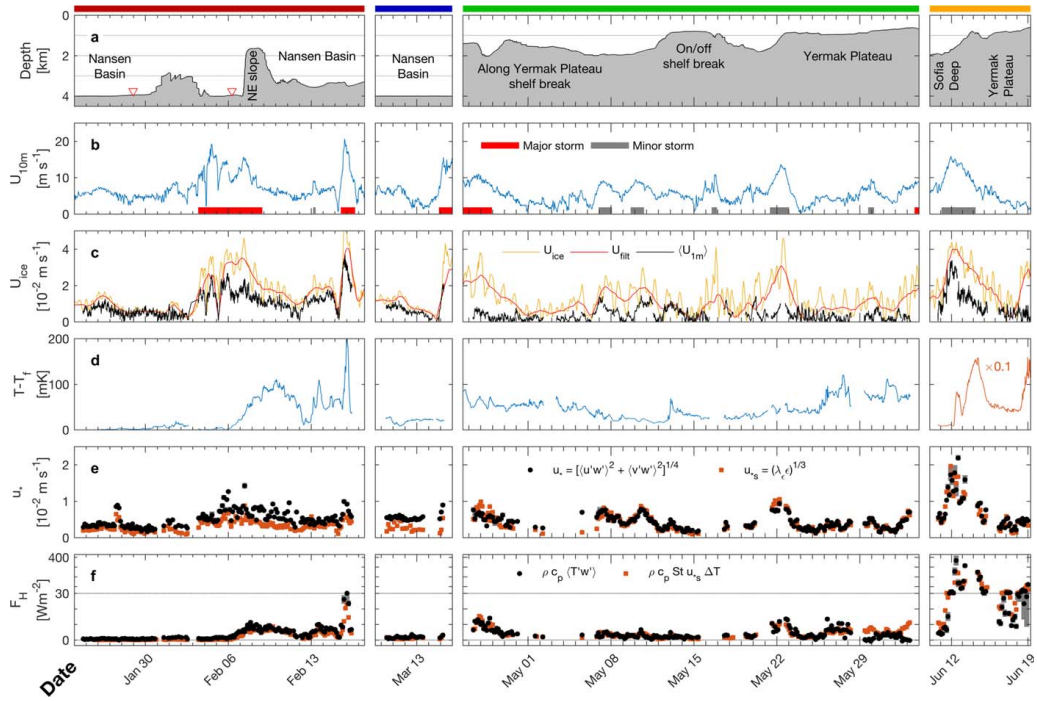

Figure 3. Time series of (a) water depth (ETOPO-1), (b) 10 m wind speed, with storms indicated by horizontal bars, (c) filtered (demodulated using diurnal and semidiurnal periods) and unfiltered ice drift speed and current magnitude at 1 m (black), (d) temperature above freezing (note factor of 10 reduction in fourth panel), and 3 hourly averaged values of (e) friction speed from covariance measurements (u_*, black) and vertical velocity spectra (u_{*s}, red) and (f) heat flux for the four TIC deployments. Parameterized heat flux is shown in red. Note the change in vertical scale above 30 W m^{-2} in Figure 3f. Error bars for friction velocity and heat flux indicate 95% confidence limits from bootstrap calculations.

Floe 2 drift was confined to the Nansen basin, at depths greater than 3900 m. The under-ice turbulence record from Floe 2 covers about 6 days. A passing storm between 14 and 16 March broke up the ice floe, disconnected the power cord, and thus terminated the record on the night of 15 March. Ice drift speeds were on average 30 cm s^{-1} during the storm, compared to 10 cm s^{-1} the week prior.

Floe 3 drifted over the eastern flank and top of the YP. Depths during TIC deployment varied between 600 and 2000 m. Our measurements here started during a major storm event, and throughout May, several minor storms were encountered. The wind speed averaged over the duration of the storms was 9.3 m s^{-1}, compared to 4.6 m s^{-1} otherwise. Over the plateau, the ice drift speed was affected by tides as well as wind (Figure 2b), and diurnal variation in drift speed can clearly be seen from Floe 3 (Figure 3c). Mean ice speed during the storms was 25 cm s^{-1}, whereas excluding storms gives a mean of 11 cm s^{-1}. Onset of ice bottom melt was observed on 31 May by hot-wires [*Rösel et al*., 2016], concurrent with the ice camp drifting over warmer AW.

Floe 4 was a drift during rapid melting conditions [*Itkin et al*., 2015]. Ice bottom melt started on 12 June. The first melt pond was observed on 9 June, and the onset of snow melt was recorded on 14 June (A. Rösel, personal communication, 2016). The drift covered from the Sofia Deep to up the slope of the YP. A storm passed between 11 and 14 June, with a peak wind speed of 17.3 m s^{-1} and drift speed up to 44 cm s^{-1}.

An overview of the hydrographic and ocean current conditions during the experiment is given by A. *Meyer et al*. [2017]. AW or modified-AW is present in the water column for the whole drift, although warmer and shallower close to the Svalbard continental slope, where the main branch of the West Spitsbergen current

flows along the topography [*Meyer et al.*, 2017a]. Over the deep basin, tidal forcing is weak, whereas over the shelf slope both the M2 and K1 tidal constituents become significant (Figure 2b) [see also *Padman et al.*, 1992; *Fer et al.*, 2015].

3. Measurements in the Under-Ice Boundary Layer

3.1. Turbulence Instrument Cluster

Turbulence instrument clusters (TICs) were deployed through a hole in the ice to measure turbulent fluxes in the ice-ocean boundary layer. The hydrohole was located a few hundred meters away from the ship to avoid sampling in its wake, and was covered with styrofoam to avoid refreezing. Each cluster acquires sufficiently high-frequency measurements of ocean currents, temperature, and conductivity to resolve the turbulent momentum and heat fluxes, together with the salinity, all at approximately the same measurement volume. A set of two TICs were deployed, located at approximately 1 and 5 m below the ice undersurface. The TIC at 5 m failed to return good quality data in 90% of the total duration of the experiment. We therefore concentrate on the continuous time series obtained from the cluster 1 m below the ice.

Currents were measured by a Sontek acoustic Doppler velocimeter (ADV), sampling a 2 cm^3 volume 18 cm from the transmitter at 24 Hz, averaged to 2 Hz temporal resolution. Temperature and conductivity were measured using Sea-Bird Electronics sensors (SBE3F and SBE4, respectively), sampling at 24 Hz, averaged to 3 Hz. Additionally, the TIC was equipped with a microconductivity sensor (SBE7) on Floes 2–4.

Two slightly different setups were used during the field campaign. On Floe 1, the TICs were mounted on a fixed pole, requiring manual rotation to align with the mean flow, a setup previously used by *Randelhoff et al.* [2014]. Upon retrieval, the mast and the instrumentation were severely damaged and could not be used for the remainder of the campaign. From Floe 2 onward, another TIC mast, equipped with similar but not identical sensors, was suspended on a wire and equipped with a vane, freely rotating to face the current. This general setup and instrumentation is identical to that of *McPhee et al.* [2008] and *Sirevaag* [2009]. A pressure sensor is used to infer the exact depth of the sensors until mid-May when the pressure sensor failed. For the remaining period, the depth of the clusters was estimated manually. At times of rapid melt, the instrument depth was controlled daily.

3.2. Covariances, Friction Velocity, and Heat Flux

The processing of data from TICs follows standard methods reported thoroughly in earlier studies [*McPhee*, 2002, 2008]. The time series is split into 15 min segments. The motivation for the choice of the segment length is discussed in section A4. For each segment, currents are aligned with the mean current, so that cross stream and vertical current components average to zero, $\langle v \rangle = \langle w \rangle = 0$. Time averages are indicated by angled brackets, $\langle \cdot \rangle$. Temperature (T), salinity (S), and current components (u, v, and w) are then detrended to obtain the fluctuating ($\cdot'$) parts.

Covariances $\langle u'w' \rangle$, $\langle v'w' \rangle$, and $\langle T'w' \rangle$ are calculated to obtain the Reynolds stress components and the kinematic vertical heat flux, respectively. Confidence intervals for the covariance calculations are obtained using the bootstrap method following *McPhee* [2008, pp. 46–51]. Each 15 min time series is resampled 1000 times to make an estimate of the likelihood of our sample mean happening by chance. Covariance estimates are averaged in bins of $n = 12$ (3 h), and assuming the individual covariances are normally distributed, the 95% confidence intervals for the true mean can be calculated as [*McPhee*, 2008]

$$CI_n = \bar{X}_n \pm 1.96\sigma_n/\sqrt{n}, \tag{1}$$

where $\bar{X}_n$ is the mean of n covariance calculations and σ_n is the mean bootstrap standard deviation. Friction velocity is calculated from

$$u_* = \left[\langle u'w' \rangle^2 + \langle v'w' \rangle^2\right]^{1/4}, \tag{2}$$

together with the 95% confidence limits from the bootstrap calculations. Turbulent heat flux in units of W m^{-2}, is obtained from

$$F_H = \rho_w c_p \langle T' w' \rangle, \tag{3}$$

where ρ_w is the water density and c_p is the specific heat of seawater.

The data set is acquired under highly variable environmental forcing conditions, and is therefore subjected to an extensive quality control, fully described in Appendix A. After ensuring basic data quality for the SBE temperature and salinity sensors (section A1), noise levels of the current measurements are obtained (section A2), and a set of objective criteria are applied to each 15 min segment in order to identify and exclude questionable data affected by noise and swell, or defy the assumption of stationarity and Taylor's frozen turbulence hypothesis (section A3).

Based on our quality control, 19% of 6014 data segments are excluded from further analysis. The majority of the rejected data was from winter, caused by the lack of scatterers in the water. In total, approximately 50 days of high-quality turbulence data are retained.

3.3. Heat Flux Parameterization

A parameterization of the oceanic heat flux from bulk properties is desirable, given the inherent difficulties of direct measurements. The oceanic heat flux depends strongly on the interface friction velocity, u_{*0}, and temperature elevation above freezing. From observations of heat flux and Reynolds stress during MIZEX, *McPhee* [1992] suggested a simple bulk parameterization of heat flux,

$$F_{H,bulk} = \rho_w c_p \mathrm{St} u_{*0} \Delta T, \tag{4}$$

where $\Delta T = (T - T_f)$ is the mixed-layer temperature elevation above its freezing temperature and St is the turbulent Stanton number. In practice, we use temperature and salinity measurements from the TIC at 1 m below the ice. From the yearlong SHEBA drift, an average value of St$=0.0057 \pm 0.0004$ was found, with no apparent dependence on Reynolds number (we refer to this as the canonical value of St) [*McPhee*, 2008, pp. 116–118]. Friction velocity from covariances measured by the TIC 1 m below ice (u_*, equation (2)) can be used here, but we opt for a less noisy alternative and use u_{*s} calculated from the spectra of vertical velocity (section 3.4).

3.4. Mixing Length and Dissipation Rate

Mixing length is the vertical distance over which energy-containing turbulent eddies effectively diffuse momentum. The mixing length, λ_M, can be estimated from the inverse of the wave number at the peak in the variance-preserving form of the vertical velocity spectrum [*McPhee*, 1994]. In practice, we calculate the wave number, k, spectrum of vertical velocity, $\Phi_w(k)$, for each 15 min segment, obtain the weighted spectrum as $k\Phi_w$, logarithmically bin in k, fit a tenth order polynomial, and then detect its maximum value and the corresponding wave number k_{max}. Mixing length is then obtained as $\lambda_M = 0.85/k_{\max}$, where k_{max} is in radian units.

In the inertial subrange of $\Phi_w(k)$, the dissipation rate of turbulent kinetic energy, ε, depends only on the local wave number and the spectral density through

$$\Phi_w(k) = \frac{4\alpha_\varepsilon}{3} \varepsilon^{2/3} k^{-5/3}, \tag{5}$$

where the constant $\alpha_\varepsilon = 0.51$ has been determined from laboratory and atmospheric experiments [*McPhee*, 2008, p. 57]. We obtain ε from a (k, Φ_w) value read from the inertial subrange, identified by the $-2/3$ slope in $k\Phi_w$ (or the $-5/3$ slope in Φ_w).

From mixing length and dissipation rate we calculate an independent, spectrally-derived friction velocity [*McPhee*, 1994],

$$u_{*s} = (\varepsilon \lambda_M)^{1/3}. \tag{6}$$

This method, using the vertical component of the velocity measurement, results in less noisy u_{*s} in low signal-to-noise ratios for two reasons: (i) w spectra are relatively less noisy than the horizontal component as a result of transducer configuration (see Appendix A) and (ii) the detection of a well-defined inertial subrange required for equation (5) excludes any spectrum with a small dynamical range. The noise level of u_* is discussed in section A2.

The mixing length is an uncertain parameter, both because of the spectral wave number bandwidth and the assumptions inherent in the method. Uncertainty propagated to the friction velocity u_{*s}, however, is small: for an assumed 50% error in ε and λ_M, assuming independent random error, the resulting uncertainty in u_{*s} is approximately 24%.

4. Results

Over the course of the four deployments we observe a wide range of heat fluxes (Figure 3f), from typically near-zero upward fluxes in winter and interior basin to several hundred W m^{-2} over the plateau when ice melt is reinforced by wind forcing and warmer underlying waters. Friction velocity (Figure 3e) generally responds to variations in wind forcing and the mobility of the ice pack. In the following, we present a floe-by-floe overview of the heat flux and friction velocity statistics based on 15 min values. Temperature is given as the elevation above the salinity-determined freezing point, $\Delta T = T - T_f(S)$, in units of milli Kelvin (mK).

On Floe 1, average vertical heat flux is 3.8 W m^{-2}. Prior to 6 February, wind is relatively calm and drift is slow over the abyssal plain. Temperature is near freezing ($\langle \Delta T \rangle = 2.9$ mK) and heat fluxes are small ($\langle F_H \rangle = 0.9\,\mathrm{W\,m^{-2}}$). The storm on 3 February accelerates the ice, and from 6 February temperatures rise to $\Delta T = 110$ mK accompanied with an increase in turbulent heat flux. Between 6 and 12 February, $\langle F_H \rangle = 6.1\,\mathrm{W\,m^{-2}}$, with a maximum of 11.3 W m^{-2}. The elevated heat fluxes correspond to the drift over shallower topography on the eastern slope of the YP where the mixed-layer temperature is higher. Water temperature approaches freezing again on 12 February, but rises in response to the passage of an intense storm, peaking at $\Delta T = 240$ mK on 16 February. Heat fluxes increase to $F_H = 31\,\mathrm{W\,m^{-2}}$, and $\langle F_H \rangle = 7.4\,\mathrm{W\,m^{-2}}$ between 12 and 17 February. Friction velocity averages to 4 mm s^{-1} prior to 6 February, and 6 mm s^{-1} after. Note that the velocities for Floe 1 have been filtered to remove the contamination by noise (see section A1), and friction velocity is likely underestimated.

The entire Floe 2 drift is over the deep Nansen basin. Temperature is slightly higher than during the first part of Floe 1 ($\langle \Delta T \rangle = 21$ mK), and heat fluxes are nearly doubled ($\langle F_H \rangle = 1.7\,\mathrm{W\,m^{-2}}$). This is consistent with differences seen in the upper mixed layer between Floe 1 and Floe 2 [*Meyer et al.*, 2017]. Using idealized one-dimensional modeling, I. Fer *et al.* [2017] attribute this mainly to entrainment of warm water from below. On 14 March, a storm accelerated the ice drift, but the ice broke up, and the instruments lost power before the storm peaked. The highest heat flux observed on Floe 2 was 3.2 W m^{-2}, but does not include possibly larger values during the storm.

The drift of Floe 3 is the longest, moving along the slope of the YP (depths less than 2000 m), before drifting over the plateau after 22 May. Available heat at the sensor depth ($\langle \Delta T \rangle = 46$ mK) is about twice that of Floe 2, and heat flux averages to $\langle F_H \rangle = 3.8\,\mathrm{W\,m^{-2}}$. During the five storms, heat fluxes average to 6.3 W m^{-2}, a doubling compared to periods without storms ($\langle F_H \rangle = 3.1\,\mathrm{W\,m^{-2}}$).

Floe 4 covers a period of rapid melt, when ocean-ice heat fluxes are enhanced by the passage of a storm. Temperature is 91 mK above freezing the day before the storm, and increases to 840 and 1600 mK in two separate peaks; 1 day after the peak wind forcing, and then by the end of the storm. The first peak is associated with stronger wind forcing and higher drift speed. Turbulent heat fluxes averaged over a 12 h window centered at each temperature peak are $\langle F_H \rangle = 286\,\mathrm{W\,m^{-2}}$ and $\langle F_H \rangle = 140\,\mathrm{W\,m^{-2}}$, respectively. The maximum heat flux was observed with the first peak, reaching 578 W m^{-2} (3 h average, 367 W m^{-2}). There is an 18 h data gap in observations during the storm. Excluding the storm and the following first day from the calculations, the heat fluxes are still relatively high compared to other drifts, $\langle F_H \rangle = 46\,\mathrm{W\,m^{-2}}$. Averaged over all of Floe 4, $\langle F_H \rangle = 63\,\mathrm{W\,m^{-2}}$, reflecting the frequent moderate heat fluxes. Also, occasional negative values are observed, notably in the two final days of the drift, and tend to lower the 3 h averages which remain positive throughout. Friction velocity is 11 mm s^{-1} on average, and reaches a maximum of 22 mm s^{-1}, which is also the largest throughout the campaign.

Estimated mixing length is highly variable on short timescales, leading to large error bars on daily averages (Figure 4b), but the campaign average value ($\pm$one standard deviation) is $\lambda_M = 0.54 \pm 0.20$. The mode value (0.44) is close to the mixing length for neutral stratification, $\kappa z = 0.4$, expected at a distance $z = 1$ m from the boundary in the constant stress boundary layer using von Kármán's constant $\kappa = 0.4$. Dissipation rates of

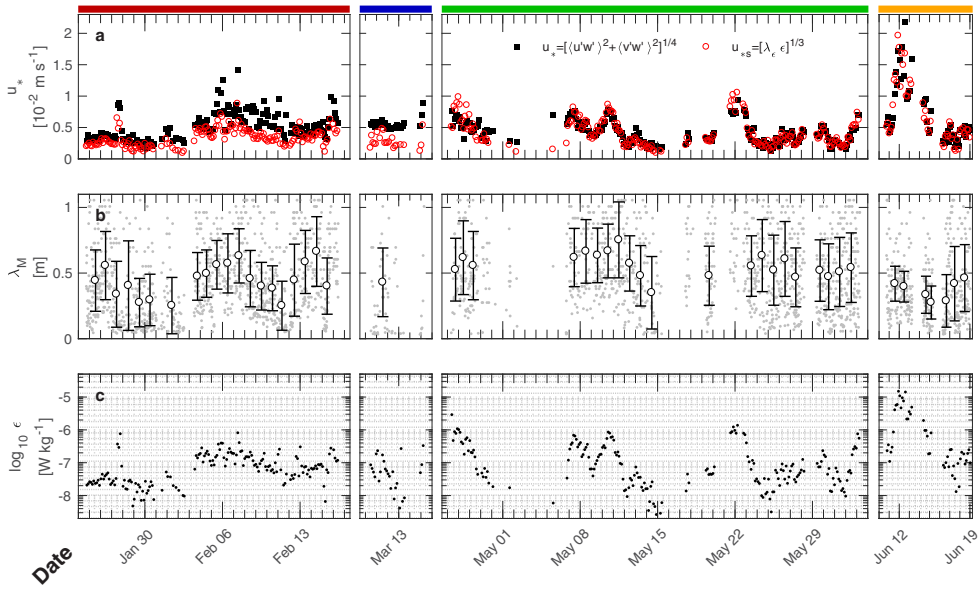

Figure 4. Time series of variables derived from spectra of vertical velocity. (a) Friction velocity from covariance (black) and from spectra of vertical velocity (red). (b) Mixing length (dots), daily average (circles) and one standard deviation envelope. (c) Dissipation rate of turbulent kinetic energy, ε, calculated as described in section 3.4.

turbulent kinetic energy span 4 orders of magnitude, from $\varepsilon \sim 10^{-9}$ W kg^{-1} in quiescent periods of Floes 1–3, to a maximum of $\sim 10^{-5}$ W kg^{-1} during the wind event in Floe 4.

5. Discussion

Momentum transfer from atmosphere to ocean drives mixing of the upper ocean. Typically the observed ocean heat flux to sea ice is a combination of several factors, including solar heating of the upper layer, salt and heat fluxes from sea ice melt, and the vertical mixing of heat from underlying warm water by wind from above or by tides over topography. Differences are large between the deep basin and over the continental slope where AW resides. We attempt to separate and quantify these factors.

5.1. Wind-Forced Mixing

The absence of solar heating in winter allows us to estimate the contribution of oceanic heat from below to observed heat fluxes during Floes 1 and 2. Floe 1 drifted in complete darkness, and during Floe 2 solar angles were low enough that we can assume no solar heating under the ice. The two floes were mostly confined to the deep basin, away from significant tidal mixing (Figure 2). We thus consider the observed heat fluxes to be wind forced, and representative of deep basins in the Arctic Ocean. Over the deep basin ($D > 3750$ m), $\langle F_H \rangle = 1.4 \pm 1.6$ W m^{-2} ($\pm$ one standard deviation) from January through March. The median value is 0.9 W m^{-2} and is representative of the quiescent periods. Calculated over storm periods, the average heat flux in winter is 2.1 ± 2.3 W m^{-2}, while for quiescent periods the average is 1.0 ± 1.1 W m^{-2}. The comparatively high standard deviations reflect the high temporal variability and the importance of individual events. The occurrence distribution of the observed heat fluxes is shown in Figure 5, and it is clear that storm events in winter shift the distribution toward higher, although still modest, heat fluxes. Using a simple one-dimensional model, *Fer et al.* [2017] show that the hydrographic evolution of the upper ocean during the N-ICE2015 winter drift can be fairly well reproduced from realistic forcing from variable profiles of eddy diffusivity in the water column. The increase in heat flux during winter storms can be attributed to entrainment of relatively warm waters from deeper in the water column.

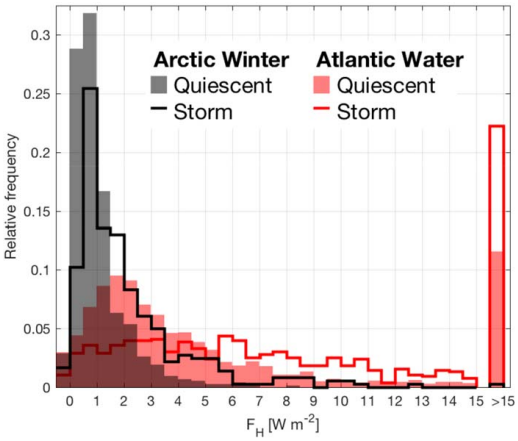

Figure 5. Histograms showing relative frequency of occurrence of ocean-to-ice heat flux during Arctic winter (black, identified as depths $D > 3750$ m) and over Atlantic Water influence (red, $D < 2000$ m). Data from storm periods (lines) show a shift toward higher heat fluxes compared to quiescent (shading) in both cases. 21 and 10% of the fluxes over Atlantic water are >15 W m^{-2} during storms and quiescent conditions, respectively, and are bulked together in the rightmost column.

Relying on the bulk parameterization applied to data from drifting buoys, *McPhee et al.* [2003] estimated an annual average heat flux of 2.6 W m^{-2} over the deep Arctic Ocean, by assuming zero heat flux from January through April. This suggests that the winter values can account for approximately one third of the annual average heat flux in the central Arctic. Using eddy covariance measurements at 6 m on ice-tethered profilers in the Canada Basin, *Cole et al.* [2014] found October–April average heat flux of 1.0 ± 2.9 W m^{-2}, comparable to our observations.

One event worth highlighting is from the storm in early February. The storm causes the ice camp to retroflect and cross its own track (Figures 1 and 6a). The times of passages at the intersection (I1 and I2) are approximately 1 week apart (red triangles in Figure 3a), and can give some insight into the temporal variability. Figure 7 contrasts 1 week time series of selected parameters surrounding I1 and I2, and Table 2 lists their mean values over 24 h, centered at the intersection. The first passing, I1, is during calm conditions, slow ice drift, and near-zero heat flux. The second passing, I2, is during strong winds and high drift speed, where temperature at the measurement depth is higher and the observed heat flux is four times larger than during I1. The rapid turning of the wind (Figure 7a)

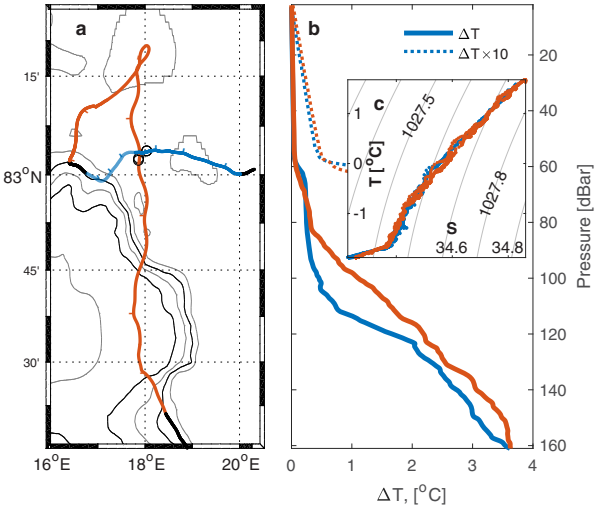

Figure 6. (a) Map of the drift trajectory around the intersection. One week surrounding the I1 (blue) and I2 (red) intersects correspond to the time series in Figure 7. (b) Average profiles of temperature above freezing from three MSS casts nearest the crossing I1 (blue) and after I2 (red) (see Figure 7), marked by circles in Figure 7a; corresponding temperature-salinity diagram is shown in Figure 7c.

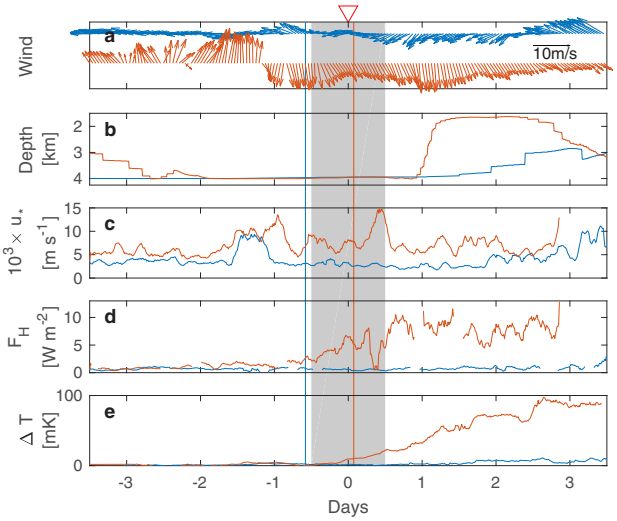

Figure 7. One week time series of (a) wind, (b) depth, (c) friction speed, (d) heat flux, and (e) temperature above freezing, centered on each of the two crossings I1 (blue) and I2 (red) (see Figure 6). Gray patch envelopes the 24 h window used to calculate average values in Table 2, and the times of profiles used in Figure 6 are indicated by vertical lines. Here wind arrows are 1 h running average, 15 min values are used for u_* and F_H.

accelerates the ice pack southward, breaking up the ice. At this time, strong shear and divergence of the ice cover is observed as the sea ice concentration dips below 100% (P. Itkin *et al.*, Thin ice and storms: Sea ice deformation from buoy arrays deployed during N-ICE2015, submitted to *Journal of Geophysical Research*, 2017). Profiles of temperature (Figure 6b) and salinity reveal a rise in the pycnocline of approximately 10 m, and there is an increase in mixed-layer (top 58 m) temperature above freezing of 4.5 mK. The similar TS properties (Figure 6c) indicate that the water mass is essentially the same, and the change in the profiles is likely due to local processes, rather than, e.g., a shift in the AW layer. This is supported by the findings of *Fer et al.* [2017]. The divergence of the ice field in response to northerly winds could also drive upwelling of the pycnocline, as was previously observed by *McPhee et al.* [2005].

While the first half of the experiment drifts over the deep basin, Floes 3 and 4 are typically located over the slopes or the Yermak Plateau. The main pathway of AW north of Svalbard crosses the saddle of the YP, and continues along the continental shelf slope, while another branch follows the slope around the north side of YP, before reconnecting with the main branch [*Rudels et al.*, 2000; A. Meyer *et al.*, 2017a]. Elevated oceanic heat fluxes in proximity to AW were reported by *Sirevaag and Fer* [2009], who observed surface heat fluxes of order 100 W m^{-2} over the branches of the West Spitsbergen current. From a buoy drift over the YP, *McPhee et al.* [2003] found that basal heat flux was dominated by mixing of the underlying warm water over the plateau, reaching up to 100 W m^{-2}. We therefore expect elevated heat fluxes here compared to the deep basin, and the circulation pattern is in part reflected in the observed heat fluxes (Figure 8). The southernmost track (Floe 4) passes over the main pathway of AW, where we observed the highest heat fluxes. Also, observations made between the eastern flank of YP and the continental slope (Floe 1) show elevated heat fluxes relative to other locations; however, these occurred under severe wind forcing. Away from these branches and the shelves, heat fluxes were typical of the central Arctic.

Table 2. Average Wind Speed (U_{10}), Friction Velocity (u_*), Heat Flux (F_H), Temperature Above Freezing (ΔT), and Ice Speed (u_{ice}) Over 24 h Centered on the Two Intersection Passings I1 and I2, Indicated by Gray Shading in Figure 7

	I1	I2
U_{10} (m s^{-1})	4.5	12.8
u_* (10^{-3} m s^{-1})	3.0	8.2
F_H (W m^{-2})	0.54	2.3
ΔT (mK)	1.3	7.1
u_{ice} (cm s^{-1})	5.5	34

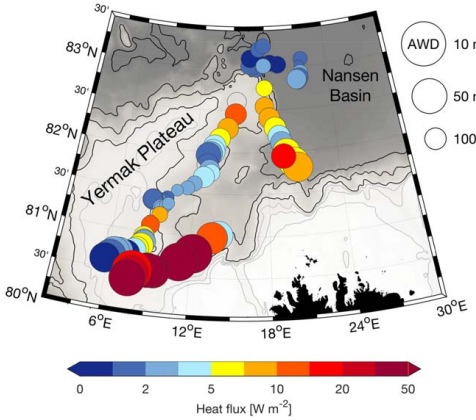

Figure 8. Map of daily averaged observed upward ocean-ice heat flux along the drift track (colors). Circle size scales inversely with the depth of the Atlantic Water layer (AWD, inferred as the depth of the 0°C isotherm).

The relative influence of topographic features and the presence of AW on the observed heat fluxes cannot be separated using the present data set. Because the boundary current carrying the AW follows the bathymetry, the drift over the AW branches is always colocated with rough topography. For depths $D < 2000$ m, AW or modified-AW is typically present, and the histogram of heat flux (Figure 5) is markedly different from the Arctic Winter case. The mode value is approximately twice as large ($\sim$2 W m^{-2}), median is four times greater (3.6 W m^{-2}), and the mean value over all data where $D < 2000$ m is $\langle F_H \rangle = 15.5 \pm 54$ W m^{-2}, reflecting how episodic occurrences of heat fluxes greater than 15 W m^{-2} (7%, Figure 5) dominate the mean and variability. When subsampled over quiescent periods with $D < 2000$ m, $\langle F_H \rangle = 10.8 \pm 42.3$ W m^{-2}. During storms, the average heat flux increases to $\langle F_H \rangle = 27.8 \pm 76.4$ W m^{-2}.

Toward the end of Floe 3, incident solar radiation becomes significant, as evident from the encounter of an under-ice phytoplankton spring bloom on 25 May [*Assmy et al.*, 2017]. Effects of solar heating and sea ice melt dominate observations from the remainder of the campaign.

5.2. Solar Heating and Sea Ice Melt

Solar radiation is a major source of heating in the surface mixed layer [*Maykut and McPhee*, 1995; *McPhee et al.*, 2003; *Shaw et al.*, 2009; *Gallaher et al.*, 2016]. In summer, solar radiation heats the upper ocean through openings in the ice cover and through melt ponds, which then can reach the ice from below. Floe 4 drifts onto the YP in June, and snowmelt, melt ponds, and rapid ice bottom melt were observed concurrently with the highest heat fluxes throughout the campaign.

The presence of AW north of Svalbard is the cause of the typically low sea-ice extent in the area [*Rudels et al.*, 2004; *Onarheim et al.*, 2014], and the AW constantly loses heat to the surface water, melting or preventing the formation of sea ice. While AW flows near the surface during the whole Floe 4 drift (Figure 8) (see also A. Meyer *et al.*, 2017a), the floe drifts near the ice edge (Figure 1), and the wind event between 11 and 14 June takes the ice over waters which were recently exposed to solar radiation. The observed heat fluxes in the later part of the experiment (Floe 4) are thus caused by a combination of heat from the AW layer from below and solar heating of the upper ocean [*Taskjelle et al.*, 2016], as well as effects of freshwater from the melting ice.

The low sea ice concentration and proximity to the ice edge (P. Itkin *et al.*, submitted manuscript, 2017) enhance solar heating of the upper mixed layer, and can at least in part account for the large heat fluxes observed in Floe 4. During its last days, Floe 3 drifted parallel to Floe 4, but observed heat fluxes here were 1–2 orders of magnitude lower, which can be related to the greater distance from the ice edge. The ice edge from 17 June shown in Figure 1 is representative of June ice extent. The mean distance between these two drift segments was 30 $\pm$ 5 km ($\pm$one standard deviation, distance is taken as that to the nearest point on the Floe 4 track from the position Floe 3 at each time). Similar observations were made by *Morison et al.* [1987] and *McPhee et al.* [1987] during the Marginal Ice Zone Experiment (MIZEX) in June 1984. The final days of Floes 3 and 4 are colocated with the ice station drift of the Polar Queen in 1984. In the same season, they drifted near the ice edge, and across a temperature front which corresponded to the recent position of the ice edge. They found that periods where the ice floe drifted over recently ice-free waters, additionally warmed by insolation, dominated the heat budgets.

During parts of the drift, heat fluxes measured at the TIC are occasionally reduced relative to what would be expected from a standard bulk parameterization (see section 5.3). Two possible explanations exist: solar heating, which can invert or weaken the temperature gradient, or near-surface intrusions of meltwater which skews the ice-ocean interface heat balance. Both explanations are explored below.

Differential heating increases with the observed spring bloom (P. Assmy *et al*., submitted manuscript, 2017), as a greater fraction of the light is absorbed in the top layer [*Taskjelle et al*., 2016]. While this typically stabilizes the surface layer, turbulent mixing would lead to a downward flux of this heat. As the ice floe drifts from warmer to cooler waters, shear drags warm water near the boundary over cooler water below, setting up a positive vertical temperature gradient. The warm water lens may be located above the sampling volume, which may explain why observed vertical heat fluxes at 1 m are significantly reduced, or even negative, while the true heat flux to the ice undersurface is still strongly positive in later parts of Floe 4. Indeed, while heat flux measured by the TIC for example on 14 June is equivalent to about 4 cm of melt, nearby ice thickness measurements from hot wires show a 24 cm reduction in ice thickness [*Rösel et al*., 2016]. The same mechanism was proposed to explain the negative heat fluxes observed by *McPhee* [1992], and for significantly reduced heat fluxes observed by *Sirevaag* [2009] as they drifted over a horizontal temperature gradient. When this mechanism dominates, it is likely that the true oceanic heat flux to the ice is significantly greater than observed at the 1 m measurement level.

The second possibility to explain apparent reductions in heat fluxes measured at 1 m below the ice-ocean interface is that the melting ice can also introduce lateral freshwater fluxes. Parameterized heat flux follows the observed values throughout the experiment (see section 5.3), except for two periods in the last days of Floe 3. Two wind events passed the ice camp between 29 May 17:00 and 30 May 05:00, and between 2 and 6 June (peak wind speeds 10.6 and 13.7 m s^{-1}, respectively, Figure 3b). Friction velocity was higher during the two storms ($\langle u_* \rangle$=5.7 mm s^{-1}) compared to the calm period between the storms ($\langle u_* \rangle$=2.9 mm s^{-1}). These dates match with periods when $F_{H,\mathrm{bulk}}$ underestimated F_H (Figures 9a and 9b). Using a similar set of observations of ice-ocean heat fluxes in late summer, *Randelhoff et al*. [2014] observed that the bulk heat flux formula (equation (4)) frequently overestimated the measured heat flux. As an explanation, they suggested that atmospheric (non-oceanic-derived) ice melt could create additional freshwater at the ice-ocean interface which increases the ice-ocean interface freezing temperature, thereby effectively skewing the balance between

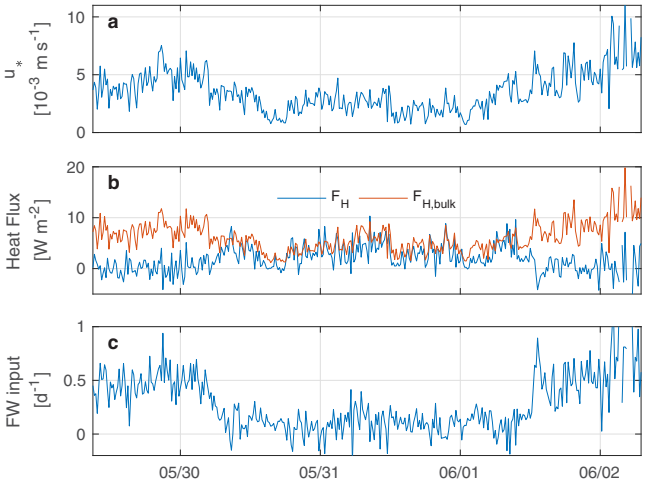

Figure 9. Time series from the period where parameterized heat flux deviates significantly from measured heat flux, showing (a) friction speed, (b) observed and parameterized heat flux, and (c) calculated equivalent freshwater input.

oceanic heat and salt fluxes and reducing the ice-ocean temperature gradient [*Randelhoff et al.*, 2014, equation (14)].

Following the equations given by *Randelhoff et al.* [2014], we estimate the additional (from non-oceanic melt) salt flux that would be necessary in order to achieve this reduction in heat flux within the three-equation formalism [*McPhee*, 2008]. With the ratio of heat to salt transfer coefficients of R = 70 [*Notz et al.*, 2003] and assuming conductive heat flux through the ice $q_c = 0$ (summer conditions), ice bulk salinity $S_i = 5$ and interface salinity $S_0 = 30$, this results in an "additional" salt flux of approximately 0.5 m d^{-1} during those periods, or meltwater entrainment equivalent to 2 cm d^{-1} of ice melt (Figure 9c). Basal melt rates at that time estimated from ice mass balance data [*Itkin et al.*, 2015] were O(1 cm d^{-1}), hence, it is possible that the equivalent of 2 cm d^{-1} was diverted into leads over several preceding days. Lateral melting of ice floes, aided by water warmed in leads, might have contributed, but if the "additional" salt flux term were to explain the entire discrepancy, a buildup of the additional freshwater pool (from either leads or percolation) on the order of a few days would be required.

We conclude that the deviation from the bulk Stanton-number formula at the end of Floe 3, or at least part of it, can be explained using the more general form of *Randelhoff et al.* [2014] if during the wind events, meltwater previously accumulated in leads was entrained into the ice-ocean molecular sublayer approximately at a rate of 2 cm d^{-1}. Counter-intuitively, wind events during the melting season might therefore (temporarily) have reduced ocean cooling by inserting a disproportionately low-salinity (thus "high"-temperature) layer between oceanic heat and the melting ice. This explanation is also consistent with visually observed accumulation of freshwater in instrument holes during strong melting conditions (A. Meyer, personal communication, 2016). In addition, the ice cover was weakly convergent during that time (P. Itkin *et al.*, submitted manuscript, 2017), indicating that meltwater may have been pushed out of the leads, contributing to entrainment of freshwater into the ice-ocean boundary layer.

5.3. Parameterized Heat Flux

Agreement between the heat flux measured by covariance and the one estimated by the bulk parameterization (equation (4)) using the canonical value of the Stanton number was typically good, with a correlation of r = 0.82, reflecting the variability in wind forcing (u_*) and mixed-layer heat content (ΔT). A variable value for the bulk heat transfer coefficient (bulk Stanton number denoted by St_*) is calculated as the ratio between measured heat flux near the interface and the product of mixed-layer temperature above freezing and interface friction velocity,

$$St_* = \frac{\langle w'T' \rangle}{u_{*0}\Delta T}. \tag{7}$$

Different authors have noted a dependence of St_* on whether ice is melting or freezing at the bottom [e.g., *McPhee et al.*, 2008]. Freezing conditions are characterized by St_* on the order of 0.012 [*Cole et al.*, 2014], and the neutral and melting case is usually associated with the canonical value of about 0.0057. The ratio *R*, of heat and salt transfer coefficients is indicative of the strength of double-diffusive processes near the ice-water interface. Typical values of *R* during melting conditions are between 35 and 70 [*McPhee et al.*, 2008; *Notz et al.*, 2003], with a measured value of 33 north of Svalbard [*Sirevaag*, 2009], i.e., only melting conditions lead to substantial double-diffusive effects.

We group the data in three temperature categories: We define $\Delta T < 50$ mK as "near-freezing," 50 mK $< \Delta T < 200$ mK as "nonfreezing," and $\Delta T > 200$ mK as "warm." Observed and parameterized heat fluxes are grouped accordingly, and we find mean bulk Stanton numbers of $St_*(\text{near-freezing}) = 0.0108$ (0.0039, 0.0130), $St_*(\text{nonfreezing}) = 0.0061$ (0.0020, 0.0080), and $St_*(\text{warm}) = 0.0059$ (0.0024, 0.0072), where numbers in brackets indicate first and third quartiles.

Overall, our data set exhibits a tendency that the average bulk Stanton number (not accounting for a constant meltwater-induced offset) increases with lower values of ΔT, particularly below O(0.1 K) (Figure 10). We can conjecture that this indicates increasingly freezing-favorable conditions at low temperatures, and thus an overall gradual shift into the nondouble-diffusive freezing regime, characterized values of *R* near unity [*McPhee et al.*, 2008].

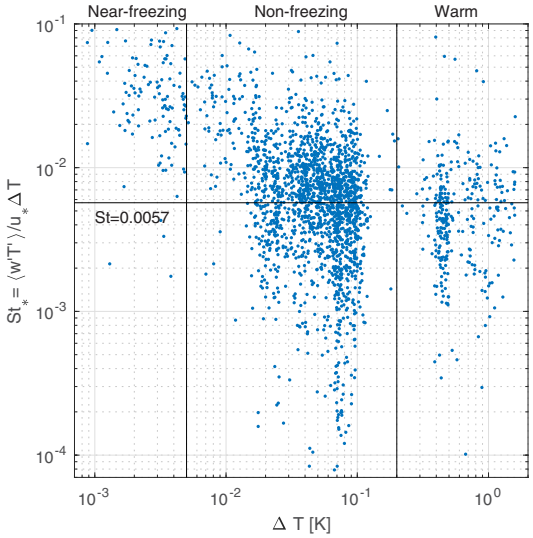

Figure 10. Temperature elevation above freezing versus bulk Stanton number. The three temperature groups (section 5.3) are indicated, separated by vertical lines. The canonical $St = 0.0057$ is shown for reference.

6. Conclusions

From direct measurements of under-ice turbulence in the Nansen Basin we find low, but non-zero upward heat fluxes in winter, averaging to 1.4 W m^{-2} with a standard deviation of 1.6 W m^{-2}, from January through March. Episodic events, such as a local upwelling event observed in February (section 5.1 and Figures 6 and 7), significantly increase heat fluxes and dominate variability. The proximity to Atlantic Water (AW) pathways and the shoaling of the AW layer are observed to increase the heat fluxes in winter by one order of magnitude (Figures 5 and 8).

Significantly higher oceanic heat fluxes are observed in spring. The observed heat fluxes are a combination of heat from the AW layer from below, solar heating at the surface, as well as effects of freshwater from the melting ice. Turbulent fluxes were particularly enhanced when the ice camps drift over topography near the YP or the northern slope of Spitsbergen. However, the presence of AW is not sufficient, and forcing is necessary to mix up heat toward the ice. We consistently observe enhanced mixing during wind events, and even more so when the ice is free to move. A wind event combined with drift over a shallow AW layer, resulted in 3 h average heat fluxes reaching 367 W m^{-2}, coinciding with rapid melt.

A commonly used bulk parameterization for heat flux is useful, and results in credible estimates in good agreement with observations. The bulk formula overestimates the heat flux on two occasions of increased wind forcing, both attributed to freshwater accumulated in leads, equivalent to approximately 2 cm d^{-1} of sea ice melt. Overall, while the parameterization successfully reproduces heat fluxes in winter conditions, more detailed process studies will be necessary to increase predictability of ice-ocean fluxes in conditions of rapid melt, solar heating, and strong lateral gradients.

Appendix A: Quality Screening

A1. Basic Quality Control

As a basic quality measure, temperature and salinity measurements from the two TICs at 1 and 5 m are compared for consistency. Temperature is concluded to be reliable for the whole deployment at both depths, while salinity at 5 m is discarded for Floes 1 and 3. Shorter periods with spurious salinity values are discarded from the 1 m sensor (e.g., salinity drift at start of a deployment). Furthermore, temperature and salinity are compared to measurements obtained from the microstructure sonde (MSS) [*Meyer et al.*, 2016], which was frequently used for profiling nearby. The MSS has itself been calibrated post-cruise against the ship's more accurate SBE CTD (A. Meyer *et al.*, Mixing rates and vertical heat fluxes north of Svalbard from Arctic winter to spring, submitted to *Journal of Geophysical Research*, 2017b). Using only data prior to 19 May, i.e., excluding the melting conditions, the mean difference between TIC and MSS measurements is 5 mK for temperature and 3×10^{-3} for salinity. There is no discernible difference in agreement with MSS between the two TIC-setups (Floe 1 versus Floes 2–3).

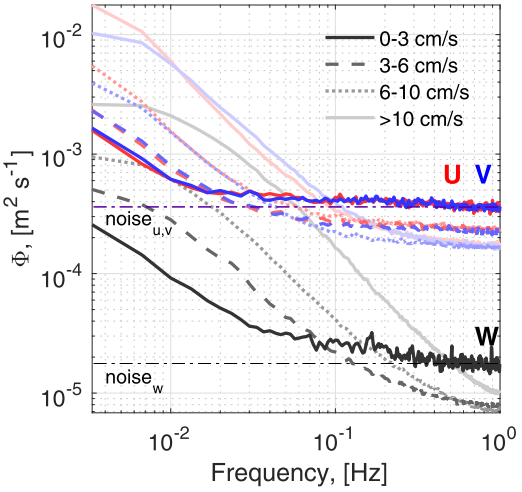

Figure 11. Frequency spectra of current velocity from the ADV, averaged in bins of mean current speed. Noise levels used in equation (A1) are indicated by horizontal lines.

A2. Noise Level

The SonTek ADVOcean user manual states a measurement accuracy for the ADV of ±1% or ±0.5 cm s^{-1}. The current meters depend on acoustic backscatter from particles suspended in the water. In the clear Arctic waters, particularly in winter, a lack of scatterers leads to low signal-to-noise ratios. We estimate the actual noise level of the current measurements from the velocity spectra, bin-averaged with respect to mean current speed (Figure 11). At high frequencies, white noise dominates over the signal, and we get an estimate of the noise level by integrating a white noise model spectrum (dotted lines in Figure 11) over the frequency domain,

$$\sigma_n = \int_0^1 \Phi_n df = \Phi_n|_0^1 \,, \qquad \text{(A1)}$$

$$\bar{u}_n = \sqrt{\sigma_n}. \qquad \text{(A2)}$$

Estimated noise levels for mean current speed <3 cm s^{-1} are $[u_n, v_n] \approx 2\times10^{-2}$ m s^{-1} and $w_n \approx 4\times10^{-3}$ m s^{-1}. The varying amount of scattering particles in the water does, however, call for a temporal varying noise estimate to be considered. From spectra of velocity for each 15 min segment, we only accept segments where average low-frequency (<0.02 Hz) spectral density is at least three times the average high-frequency (>0.1 Hz) levels. This ensures the dynamic range of the spectra, and the remaining segments are discarded as white noise.

The instrumentation and setup used in Floe 1 are identical to those used in *Randelhoff et al.* [2014] and suffer from similar noise issues. Following *Randelhoff et al.* [2014], we apply a first-order Butterworth low-pass filter with a cutoff frequency of 0.1 Hz to the Floe 1 current data. The cutoff frequency is chosen, based on spectral considerations, as the frequency where the white noise dominates, and is higher than that of *Randelhoff et al.* [2014] (0.0316 Hz). This fairly severe filtering lowers the fluxes uniformly, but the overall effect, not quantified here, depends on the turbulent length scale and mean advective velocity. While we preserve more of the variance relative to *Randelhoff et al.* [2014]'s filter, the resulting friction velocity and its variability are significantly reduced by this filtering. The effect of this on $\langle w'T' \rangle$ is a 9% average reduction, indicating that a small fraction of temperature-correlated variability is also removed.

We estimate the noise level of u_* from synthetic 15 min time series of u, v, and w, with variance equal to the noise obtained from spectra. The resulting u_{*n}=0.2 cm s^{-1} is an estimate of the covariance noise level for the experiment as a whole. Floe 2 data are from a low signal-to-noise ratio environment where we suspect covariances are dominated by noise (Floe 1 is filtered as described above). Noise level at Floe 2 is estimated visually as the lower range of observed values, $u_* \approx 0.5$ cm s^{-1}. The mean ratio u_*/u_{*s}=2.9 and 1.3, for Floe 2 and Floes 3–4, respectively. The larger discrepancy between u_* and u_{*s} on Floe 2 compared to Floes 3 and 4 indicate that the improvement using friction velocity from spectra over covariance is much larger in winter, when scatterer levels are low, compared to spring and summer.

A3. Systematic Quality Control

An objective set of criteria for automatic flagging of bad data is employed. Calculating covariances from point measurements require the Taylor's frozen field hypothesis to be satisfied, meaning that the turbulent structure can be considered "frozen" as it is advected past the measurement sensor

[*Thorpe*, 2007]. Each 15 min velocity time series segment is split into 1 min, half overlapping subsegments (29 data points), over which we calculate the mean and root-mean-squared quantities, further used in the following tests.

Taylor's hypothesis requires the flow to be stationary over the averaging period. To test for stationarity, we compare the 15 min time evolution of 1 min statistics (mean and root-mean-square, r.m.s.) to those calculated identically from synthetic Gaussian noise time series. If the cumulative time integral of the statistics is not significantly larger than that obtained from the noise, we deem that there is no trend or significant time variability in the statistics for the 15 min duration used in the covariance calculations, hence the stationarity assumption is fulfilled. Formally we require the integrated absolute mean velocity anomaly, i.e., the difference between 1 min average values and the 15 min mean, and integrated absolute r.m.s. velocity anomaly are both less than 2.5 times the values inferred identically from a Gaussian white noise of amplitude $u_n = 2\times10^{-2}$ m s^{-1} (instrument noise level). Because the Gaussian synthetic time series can differ for a given realization, we repeat the calculation 1000 times and use the average value. The 2.5 threshold is obtained by conducting similar analysis from unstationary synthetic time series with wave behavior or an imposed significant trend. Another concern for turbulence measurements is when the mean flow changes direction throughout the segment (again violating the stationarity assumption) and, in severe conditions, approaches the TIC from behind the sensors leading to sampling of unnatural turbulence at the wake of the flow. To exclude such segments, we require that the direction of the horizontal current should not deviate more than $\pm60^{\circ}$ from the main streamwise direction over a 15 min segment.

Swell is encountered in parts of the observations, notably toward the end of Floe 4, in relative proximity to the ice edge. Although fluxes measured during swell may be an interesting topic themselves, we chose to exclude these data from the present analysis. Careful analysis is needed to account for the wave orbital velocities and wave-related (nonturbulent) contribution to stress. The period of the swell was approximately 10 s. In order to identify swell, each segment is band-passed between 7 and 20 s, and the turbulence intensity in this range is compared to the turbulence intensity of the unfiltered data. We require that turbulence intensity for the raw data, $I_0 = \sqrt{\frac{1}{3}(u_{rms}^2 + v_{rms}^2 + w_{rms}^2)}$, is significantly greater than that of the band-passed, I_{BP}. Next we require I_{BP} to be sufficiently weak compared to the mean current velocity, $\bar{U}$, and the instrument noise u_n. Formally, we require that

$$\begin{aligned} I_0/I_{BP} &> 1.8, \\ \bar{U}/I_{BP} &> 1.8, \\ I_{BP} &< 4 \times u_n. \end{aligned} \tag{A3}$$

Together, these criteria are found to effectively flag segments where the assumptions for eddy covariance measurement of turbulence are suspect, noise or swell contaminates our measurements. Exact rejection limits are ad hoc, to ensure effective flagging of bad data while retaining good data.

A4. Covariance Segment Length

The choice of 15 min intervals is based on experience from numerous experiments [*McPhee*, 2008], and is a balance between capturing all the true covariance from turbulent eddies and avoiding longer term temporal changes.

The rapid melt in spring stratifies the otherwise typically well-mixed layer, resulting in increasing buoyancy frequency. Extra care must be taken if buoyancy frequency approaches our measurement interval of 15 min. We calculate the buoyancy frequency of the upper 6 m using the microstructure profiler data [*Meyer et al.*, 2016]. Typical buoyancy period is approximately 1 h (or less, i.e., well-mixed), but in June periods of 10 min and less are observed. During periods of short buoyancy periods, internal waves may affect the turbulent fluxes inferred using 15 min segments. Recalculations of turbulent heat fluxes using segment length down to 5 min, however, reveal no significant difference from 15 min segments. Any segments violating Taylor's hypothesis are already flagged by our systematic procedure, and we consider the remaining data of acceptable quality. To be consistent throughout, we retain 15 min calculations for the entire data set.

Acknowledgments
The field work has been supported by the Norwegian Polar Institute's Centre for Ice, Climate and Ecosystems (ICE) through the N-ICE project. Additional support was obtained from the Centre for Climate Dynamics at the Bjerknes Centre through grant BASIC: Boundary Layers in the Arctic Atmosphere, Seas and Ice Dynamics. AKP is supported by the Research Council of Norway, through the project 229786. AR's work was supported through the project "Carbon Bridge," a Polar Program (project 226415) funded by the Norwegian Research Council. We thank everyone involved in the field campaign for making this study possible. The comments from two reviewers helped clarifying and improving the manuscript. The following data sets were used in this study and are publicly available at the Norwegian Polar Data Centre: TIC data [*Peterson et al.*, 2016], microstructure sonde (MSS) [*Meyer et al.*, 2016], meteorological data [*Hudson et al.*, 2015], and ice thickness from hot wires [*Rösel et al.*, 2016].

References

Assmy, P., et al. (2017), Leads in arctic pack ice enable early phytoplankton blooms below snow-covered sea ice, *Sci. Rep.*, *7*, 40850, doi: 10.1038/srep40850.

Carmack, E. C., et al. (2015), Toward quantifying the increasing role of oceanic heat in sea ice loss in the new Arctic, *Bull. Am. Meteorol. Soc.*, *96*(12), 2079–2105, doi:10.1175/BAMS-D-13-00177.1.

Cole, S. T., M.-L. Timmermans, J. M. Toole, R. A. Krishfield, and F. T. Thwaites (2014), Ekman veering, internal waves, and turbulence observed under Arctic sea ice, *J. Phys. Oceanogr.*, *44*(5), 1306–1328, doi:10.1175/JPO-D-12-0191.1.

Fer, I. (2009), Weak vertical diffusion allows maintenance of cold halocline in the central Arctic, *Atmos. Ocean Sci. Lett.*, *2*(3), 148–152, doi: 10.1080/16742834.2009.11446789.

Fer, I. (2014), Near-inertial mixing in the central Arctic Ocean, *J. Phys. Oceanogr.*, *44*(8), 2031–2049, doi:10.1175/JPO-D-13-0133.1.

Fer, I., M. Müller, and A. K. Peterson (2015), Tidal forcing, energetics, and mixing near the Yermak Plateau, *Ocean Sci.*, *11*(2), 287–304, doi: 10.5194/os-11-287-2015.

Fer, I., A. K. Peterson, A. Meyer, and A. Randelhoff (2017), One-dimensional evolution of the upper water column in the Atlantic sector of the Arctic Ocean in winter, *J. Geophys. Res. Oceans*, doi:10.1002/2016JC012431, in press.

Gallaher, S. G., T. P. Stanton, W. J. Shaw, S. T. Cole, J. M. Toole, J. P. Wilkinson, T. Maksym, and B. Hwang (2016), Evolution of a Canada Basin ice-ocean boundary layer and mixed layer across a developing thermodynamically forced marginal ice zone, *J. Geophys. Res. Oceans*, *121*, 6223–6250, doi:10.1002/2016JC011778.

Granskog, M., P. Assmy, S. Gerland, G. Spreen, H. Steen, and L. H. Smedsrud (2016), Arctic research on thin ice: Consequences of Arctic sea ice loss, *Eos*, *97*, doi:10.1029/2016EO044097.

Hudson, S. R., M. A. Granskog, A. Sundfjord, A. Randelhoff, A. H. H. Renner, and D. V. Divine (2013), Energy budget of first-year Arctic sea ice in advanced stages of melt, *Geophys. Res. Lett.*, *40*, 2679–2683, doi:10.1002/grl.50517.

Hudson, S. R., L. Cohen, and V. Walden (2015), N-ICE2015 surface meteorology v2, Norwegian Polar Inst., doi:10.21334/npolar.2015.056a61d1.

Itkin, P., G. Spreen, S. R. Hudson, B. Cheng, M. Doble, N. Sennechael, C. Provost, J. Haapala, M. Nikolaus, L. Kaleschke, and J. Wilkinson (2015), N-ICE2015 buoy data, Norwegian Polar Inst., doi:10.21334/npolar.2015.6ed9a8ca.

Jeffries, M. O., J. E. Overland, and D. K. Perovich (2013), The Arctic shifts to a new normal, *Phys. Today*, *66*(10), 35, doi:10.1063/PT.3.2147.

Krishfield, R. A., A. Proshutinsky, K. Tateyama, W. J. Williams, E. C. Carmack, F. A. McLaughlin, and M.-L. Timmermans (2014), Deterioration of perennial sea ice in the Beaufort Gyre from 2003 to 2012 and its impact on the oceanic freshwater cycle, *J. Geophys. Res. Oceans*, *119*, 1271–1305, doi:10.1002/2013JC008999.

Lindsay, R., and A. Schweiger (2015), Arctic sea ice thickness loss determined using subsurface, aircraft, and satellite observations, *Cryosphere*, *9*(1), 269–283, doi:10.5194/tc-9-269-2015.

Maykut, G. A., and M. G. McPhee (1995), Solar heating of the Arctic mixed layer, *J. Geophys. Res.*, *100*(C12), 24,691–24,703, doi:10.1029/95JC02554.

McPhee, M. G. (1988), Analysis and prediction of short-term ice drift, *J. Offshore Mech. Arctic Eng.*, *110*(1), 94–100, doi:10.1115/1.3257130.

McPhee, M. G. (1992), Turbulent heat flux in the upper ocean under sea ice, *J. Geophys. Res.*, *97*(C4), 5365–5379, doi:10.1029/92JC00239.

McPhee, M. G. (1994), On the turbulent mixing length in the oceanic boundary layer, *J. Phys. Oceanogr.*, *24*(9), 2014–2031, doi:10.1175/1520-0485(1994)024¡2014:OTTMLI¿2.0.CO;2.

McPhee, M. G. (2002), Turbulent stress at the ice/ocean interface and bottom surface hydraulic roughness during the SHEBA drift, *J. Geophys. Res.*, *107*(C10), 8037, doi:10.1029/2000JC000633.

McPhee, M. G. (2008), *Air-Ice-Ocean Interaction: Turbulent Ocean Boundary Layer Exchange Processes*, pp. 1–215, Springer, New York, doi: 10.1007/978-0-387-78335-2.

McPhee, M. G., G. A. Maykut, and J. H. Morison (1987), Dynamics and thermodynamics of the ice/upper ocean system in the marginal ice zone of the Greenland Sea, *J. Geophys. Res.*, *92*(C7), 7017–7031, doi:10.1029/JC092iC07p07017.

McPhee, M. G., T. Kikuchi, J. H. Morison, and T. P. Stanton (2003), Ocean-to-ice heat flux at the North Pole environmental observatory, *Geophys. Res. Lett.*, *30*(24), 2274, doi:10.1029/2003GL018580.

McPhee, M. G., R. Kwok, and R. Robins (2005), Upwelling of Arctic pycnocline associated with shear motion of sea ice, *Geophys. Res. Lett.*, *32*, L10616, doi:10.1029/2004GL021819.

McPhee, M. G., J. H. Morison, and F. Nilsen (2008), Revisiting heat and salt exchange at the ice-ocean interface: Ocean flux and modeling considerations, *J. Geophys. Res.*, *113*, C06014, doi:10.1029/2007JC004383.

Meyer, A., et al. (2017), Winter to summer oceanographic observations in the Arctic Ocean north of Svalbard, *J. Geophys. Res. Oceans.*, doi: 10.1002/2016JC012391, in press.

Meyer, A., et al. (2016), N-ICE2015 ocean microstructure profiles (MSS90L), Norwegian Polar Inst., doi:10.21334/npolar.2016.774bf6ab.

Morison, J. H., M. G. McPhee, and G. A. Maykut (1987), Boundary layer, upper ocean, and ice observations in the Greenland Sea Marginal Ice Zone, *J. Geophys. Res.*, *92*(C7), 6987–7011, doi:10.1029/JC092iC07p06987.

Notz, D., M. G. McPhee, M. G. Worster, G. A. Maykut, K. H. Schlünzen, and H. Eicken (2003), Impact of underwater-ice evolution on Arctic summer sea ice, *J. Geophys. Res.*, *108*(C7), 3223, doi:10.1029/2001JC001173.

Onarheim, I. H., L. H. Smedsrud, R. B. Ingvaldsen, and F. Nilsen (2014), Loss of sea ice during winter north of Svalbard, *Tellus, Ser. A*, *66*(1), 1–9, doi:10.3402/tellusa.v66.23933.

Padman, L., and S. Erofeeva (2004), A barotropic inverse tidal model for the Arctic Ocean, *Geophys. Res. Lett.*, *31*, L02303, doi:10.1029/2003GL019003.

Padman, L., A. J. Plueddemann, R. D. Muench, and R. Pinkel (1992), Diurnal tides near the Yermak Plateau, *J. Geophys. Res.*, *97*(C8), 12,639–12,652, doi:10.1029/92JC01097.

Peterson, A. K., I. Fer, A. Randelhoff, A. Meyer, L. Håvik, L. H. Smedsrud, I. Onarheim, M. Muijlwick, A. Sundfjord, and M. G. McPhee (2016), N-ICE2015 ocean turbulent fluxes from under-ice turbulent cluster, Norwegian Polar Inst., doi:10.21334/npolar.2016.ab29f1e2.

Rainville, L., C. Lee, and R. Woodgate (2011), Impact of wind-driven mixing in the Arctic Ocean, *Oceanography*, *24*(3), 136–145, doi:10.5670/oceanog.2011.65.

Randelhoff, A., A. Sundfjord, and A. H. H. Renner (2014), Effects of a shallow pycnocline and surface meltwater on sea ice-ocean drag and turbulent heat flux, *J. Phys. Oceanogr.*, *44*(8), 2176–2190, doi:10.1175/JPO-D-13-0231.1.

Rösel, A., et al. (2016), N-ICE2015 ice thickness from hot wires, Norwegian Polar Inst., doi:10.21334/npolar.2016.263a317f.

Rudels, B., R. Meyer, E. Fahrbach, V. V. Ivanov, S. Østerhus, D. Quadfasel, U. Schauer, V. Tverberg, and R. A. Woodgate (2000), Water mass distribution in Fram Strait and over the Yermak Plateau in summer 1997, *Ann. Geophys.*, *18*(6), 0687–0705, doi:10.1007/s005850000216.

Rudels, B., E. P. Jones, U. Schauer, and P. Eriksson (2004), Atlantic sources of the Arctic Ocean surface and halocline waters, *Polar Res.*, *23*(2), 181–208, doi:10.1111/j.1751-8369.2004.tb00007.x.

Serreze, M. C., and J. C. Stroeve (2015), Arctic sea ice trends, variability and implications for seasonal ice forecasting, *Philos. Trans. R. Soc. A*, *373*(2045), 1–16, doi:10.1098/rsta.2014.0159.

Shaw, W. J., T. P. Stanton, M. G. McPhee, and T. Kikuchi (2008), Estimates of surface roughness length in heterogeneous under-ice boundary layers, *J. Geophys. Res.*, *113*, C08030, doi:10.1029/2007JC004550.

Shaw, W. J., T. P. Stanton, M. G. McPhee, J. H. Morison, and D. G. Martinson (2009), Role of the upper ocean in the energy budget of Arctic sea ice during SHEBA, *J. Geophys. Res.*, *114*, C06012, doi:10.1029/2008JC004991.

Sirevaag, A. (2009), Turbulent exchange coefficients for the ice/ocean interface in case of rapid melting, *Geophys. Res. Lett.*, *36*, L04606, doi: 10.1029/2008GL036587.

Sirevaag, A., and I. Fer (2009), Early spring oceanic heat fluxes and mixing observed from drift stations north of Svalbard, *J. Phys. Oceanogr.*, *39*(12), 3049–3069, doi:10.1175/2009JPO4172.1.

Stanton, T. P., W. J. Shaw, and J. K. Hutchings (2012), Observational study of relationships between incoming radiation, open water fraction, and ocean-to-ice heat flux in the Transpolar Drift: 2002-2010, *J. Geophys. Res.*, *117*, C07005, doi:10.1029/2011JC007871.

Stroeve, J. C., M. C. Serreze, M. M. Holland, J. E. Kay, J. Malanik, and A. P. Barrett (2012), The Arctic's rapidly shrinking sea ice cover: A research synthesis, *Clim. Change*, *110*(3–4), 1005–1027, doi:10.1007/s10584-011-0101-1.

Taskjelle, T., M. A. Granskog, A. K. Pavlov, S. R. Hudson, and B. Hamre (2016), Effects of an Arctic under-ice bloom on solar radiant heating of the water column, *J. Geophys. Res. Oceans*, doi:10.1002/2016JC012187, in press.

Thorpe, S. A. (2007), *An Introduction to Ocean Turbulence*, Cambridge Univ. Press, Cambridge, U. K.

Tietsche, S., D. Notz, J. H. Jungclaus, and J. Marotzke (2011), Recovery mechanisms of Arctic summer sea ice, *Geophys. Res. Lett.*, *38*, L02707, doi:10.1029/2010GL045698.

Paper II

4.2 One-dimensional evolution of the upper water column in the Atlantic sector of the Arctic Ocean in winter

Ilker Fer, Algot K. Peterson, Achim Randelhoff, and Amelie Meyer

Journal of Geophysical Research – Oceans, **122** (2017), doi:10.1002/2016JC012431.

II

AGU PUBLICATIONS

JGR

Journal of Geophysical Research: Oceans

RESEARCH ARTICLE

10.1002/2016JC012431

Special Section:
Atmosphere-ice-ocean-ecosystem Processes in a Thinner Arctic Sea Ice Regime: the Norwegian Young Sea ICE Cruise 2015 (N-ICE2015)

One-dimensional evolution of the upper water column in the Atlantic sector of the Arctic Ocean in winter

Ilker Fer[1], Algot K. Peterson[1], Achim Randelhoff[2,3], and Amelie Meyer[3]

[1]Geophysical Institute, University of Bergen and Bjerknes Centre for Climate Research, Bergen, Norway, [2]Institute for Arctic and Marine Biology, UiT The Arctic University of Norway, Tromsø, Norway, [3]Norwegian Polar Institute, Fram Centre, Tromsø, Norway

Abstract A one-dimensional model is employed to reproduce the observed time evolution of hydrographic properties in the upper water column during winter, between 26 January and 11 March 2015, in a region north of Svalbard in the Nansen Basin of the Arctic Ocean. From an observed initial state, vertical diffusion equations for temperature and salinity give the hydrographic conditions at a later stage. Observations of microstructure are used to synthesize profiles of vertical diffusivity, *K*, representative of varying wind forcing conditions. The ice-ocean heat and salt fluxes at the ice-ocean interface are implemented as external source terms, estimated from the salt and enthalpy budgets, using friction velocity from the Rossby similarity drag relation, and the ice core temperature profiles. We are able to reproduce the temporal evolution of hydrography satisfactorily for two pairs of measured profiles, suggesting that the vertical processes dominated the observed changes. Sensitivity tests reveal a significant dependence on *K*. Variation in other variables, such as the temperature gradient of the sea ice, the fraction of heat going to ice melt, and the turbulent exchange coefficient for heat, are relatively less important. The increase in salinity as a result of freezing and brine release is approximately 10%, significantly less than that due to entrainment (90%) from beneath the mixed layer. Entrainment was elevated during episodic storm events, leading to melting. The results highlight the contribution of storms to mixing in the upper Arctic Ocean and its impact on ice melt and mixed-layer salt and nutrient budgets.

Key Points:
- A 1-D model captures the upper 200 m hydrographic variability in winter in Nansen Basin, north of Svalbard
- Melting occurs in response to entrainment during episodic strong wind forcing
- Increase in mixed-layer salinity from freezing (10%) is significantly less than that due to entrainment (90%)

Correspondence to:
I. Fer,
ilker.fer@uib.no

Citation:
Fer, I., A. K. Peterson, A. Randelhoff, and A. Meyer (2017), One-dimensional evolution of the upper water column in the Atlantic sector of the Arctic Ocean in winter, *J. Geophys. Res. Oceans*, *122*, doi:10.1002/2016JC012431.

Received 5 OCT 2016
Accepted 15 JAN 2017
Accepted article online 11 FEB 2017

1. Introduction

Below an upper surface layer with temperature near its freezing point, the Arctic Ocean water column warms toward subsurface waters of Atlantic origin [*Carmack et al*., 2015; *Rudels*, 2015]. The heat content of the relatively warm layer can affect the presence and evolution of the sea ice cover provided that mixing processes acting along or across density surfaces allow this heat to reach the underside of sea ice. In the Canada Basin, between the cold upper layer and the warm Atlantic layer, a layer of temperature maximum forms another source of heat close to the sea ice, supplied by the intrusion of relatively fresh Pacific waters [*Toole et al*., 2010]. In the Eurasian Basin, the presence of the vertical salinity gradient below the polar mixed layer (the cold halocline layer) restricts the vertical mixing of oceanic heat [*Fer*, 2009, 2014]. In the Fram Strait gateway, along the warm boundary currents, and over topographic features, on the other hand, the turbulent ocean fluxes are elevated by 1 or 2 orders of magnitude [*Lenn et al*., 2009; *Sirevaag and Fer*, 2009; *Shaw and Stanton*, 2014]. The interplay between the vertical mixing processes, advection, ice drift, ice thermodynamics, and the subsequent evolution of the temperature and salinity structure in the upper ocean affect the oceanic heat flux reaching the ice undersurface.

The cold halocline layer in the Eurasian Basin is a perennial feature limiting vertical mixing. Thus, an important question is how much the different processes (e.g., brine rejection in winter, meltwater input in summer, and erosion through turbulent mixing at the base of the mixed layer) contribute to the maintenance of upper ocean stratification in the Arctic. Studies using one-dimensional (1-D) models including vertical turbulent processes to investigate the Arctic ocean halocline and upper ocean stratification have been insightful in this regard [*Davis et al*., 2016; *Ivanov et al*., 2016]. Evaluating the estimated contribution of various terms contributing to the heat budget for the upper ocean, *Polyakov et al*. [2013] concluded that their observations from drifting buoys away from boundary currents were dominated by vertical turbulent processes.

Direct observations of microstructure in winter are sparse in the Arctic Ocean, primarily because of logistical challenges. Notable studies reporting turbulence measurements and turbulent heat fluxes under Arctic sea ice in winter (December–March) are from the SHEBA drift [*Shaw et al*., 2009] and from the drift of an ice-tethered profiler, equipped with a velocity sensor capable of resolving turbulent fluctuations [*Cole et al*., 2014]. Both drifts were in the Beaufort Sea; hence, such winter observations have not been reported from the Eurasian Basin. If we include early spring (April), valuable microstructure observations were made between 2007 and 2014 from the drifting ice camps close to the North Pole [*Fer*, 2009, 2014; *Guthrie et al*., 2015], as well as from drifts north of Svalbard [*Padman and Dillon*, 1991; *Sirevaag and Fer*, 2009]. In situ data acquired during the "Norwegian young sea ICE" (N-ICE2015) campaign [*Granskog et al*., 2016] from January to July 2015, under a wide variety of forcing conditions make a valuable contribution to our present understanding of the ocean-ice-atmosphere system in the Atlantic sector of the Arctic Ocean, north of Svalbard. Here we present observations from a subset of the N-ICE2015 data, collected in winter (February–March 2015), in the Nansen Basin and close to the northern tip of Yermak Plateau.

The N-ICE2015 special section gathers a collection of papers from the experiment covering atmosphere physics, cryosphere, marine biology, and physical oceanography. For a general description of the oceanographic and current conditions see *Meyer et al*., [2017], the microstructure observations and vertical mixing in the water column (upper 300 m) are described in A. Meyer et al. (Mixing rates and vertical heat fluxes north of Svalbard from Arctic winter to spring, submitted to *Journal of Geophysical Research*, 2016), and the under-ice boundary layer turbulence measurements (1 m below the ice) are described in *Peterson et al.* [2017]. These studies present the observations from the entire duration of the experiment, including four different drift floes. Oceanic heat fluxes measured 1 m below the sea ice in the Nansen Basin were $O(1)$ W m^{-2} in winter, and increased by a factor of 2 during wind events [*Peterson et al*., 2017]. The drift in spring was confined to the Yermak Plateau and its slopes, where the combination of wind forcing with shallow Atlantic Water (AW) layer and proximity to open waters lead to rapid melting and large heat fluxes exceeding several 100 W m^{-2} [*Peterson et al*., 2017]. The microstructure observations in the water column were consistent with the findings from the under-ice boundary layer. Winter heat flux across the pycnocline in the Nansen Basin averaged to 3 W m^{-2} during calm conditions and increased significantly to 5 W m^{-2} with storms (A. Meyer et al., submitted manuscript, 2016). Steep topography enhanced dissipation rates by a factor 4 along the eastern slopes of the Yermak Plateau, and episodically increased the turbulent heat flux deeper in the water column. The hydrography was characterized by a strong pycnocline and deep (up to 100 m) mixed layer in winter over the Nansen Basin and the Yermak Plateau slopes. In the late spring, the mixed layer was shallow (less than 20 m deep) over the Yermak Plateau. The AW inflow north of Svalbard was found to be steered by topography, partly along the Svalbard coast and partly around the Yermak Plateau [*Meyer et al*., 2017]. Winter conditions were further sampled in detail using IAOOS platforms; see, e.g., *Koenig et al.* [2016] for hydrographic conditions and *Provost et al.* [2017] for evolution of snow and ice conditions using ice mass balance buoys. *Provost et al.* [2017] report intense sea-ice basal melt in midwinter over warm AW, and snow-ice formation following storms and/or basal ice melt.

In this paper we use winter data from the drift of Floe 1 and 2, to describe the evolution of the hydrography in the upper 200 m by one-dimensional processes, forced by idealized, time-dependent vertical diffusivity profiles inferred from microstructure measurements. We concentrate on the Nansen Basin and exclude effects of advection or proximity to warm AW. The motivation is that simple numerical modeling supplemented by basic information of wind forcing can be used to describe the vertical distribution of upper ocean hydrography from a measured initial state, using representative vertical diffusivity profiles for calm, moderate, and strong wind conditions. Once the dominant 1-D (vertical) processes are identified, our measurements will be useful in the context of the basin-wide seasonal cycle of the mixed-layer heat and freshwater content. Our results, however, are specific to the upper ocean hydrography and vertical mixing processes north of Svalbard, and general conclusions cannot be drawn before further justification of the results for other regions of the Arctic Ocean. Nevertheless, the findings will help better understand the under-studied wintertime entrainment of heat, salinity, and biogeochemical tracers, such as nutrients and oxygen, from deeper water, and are relevant in the broader context of large-scale circulation and tracer studies.

2. Methods

Using the Research Vessel Lance, an experiment was staged north of Svalbard (Figure 1) when four drift stations were occupied between January and June 2015. A brief description of the experiment with aims and motivation is given in *Granskog et al*. [2016]. We use measurements from the period 25 January to 14 March 2015, including 25 days of under-ice eddy-covariance measurements and 45 sets (124 casts) of microstructure profiling.

Data from two instruments are utilized: a vertical microstructure profiler (MSS) and a turbulence instrument cluster (TIC). In the following, details for each type of data collection and reduction are briefly summarized. For further details see A. Meyer et al. (submitted manuscript, 2016) and *Peterson et al.* [2017]. Data sets are available from *Meyer et al.* [2017] and *Peterson et al*. [2016]. Ancillary data used comprise the location of the vessel, 10 min averaged wind measurements from time series combining the on-ice weather station data and the data from ship's mast [*Hudson et al*., 2015; L. Cohen et al., Meteorological conditions in a thinner Arctic sea ice regime from winter through summer during the Norwegian young sea ICE expedition (N-ICE2015), submitted to *Journal of Geophysical Research*, 2016], and ice thickness survey and ice-coring (profile of ice temperature) conducted by the ice physics group [*Rösel et al*., 2016; *Gerland et al.*, 2017]. The ship-based wind sensor, mounted at 24 m height, was used to reconstruct gaps in the 10 m wind data from the on-ice weather mast, using the wind profile power law and an empirically derived power that depends on atmospheric stability, calculated as a function of wind speed measured at 24 m (L. Cohen et al., submitted manuscript, 2016). The ice drift velocity is inferred from the ship's GPS position. Instantaneous drift velocity, calculated from first differencing in time of the ship's position, includes inertial and tidal oscillations. Because the upper water column typically oscillates approximately in phase with the ice, the instantaneous drift is not representative of the shear contribution to turbulence production. Therefore, following *McPhee* [2008, Chap. 2.5], we use complex demodulation of daily segments to express the drift velocity as the sum of a mean part (used in our analysis) and oscillations from a combination of clockwise and counterclockwise rotating diurnal and semidiurnal (approximately inertial) components. The instantaneous and filtered drift speeds are shown in Figure 2.

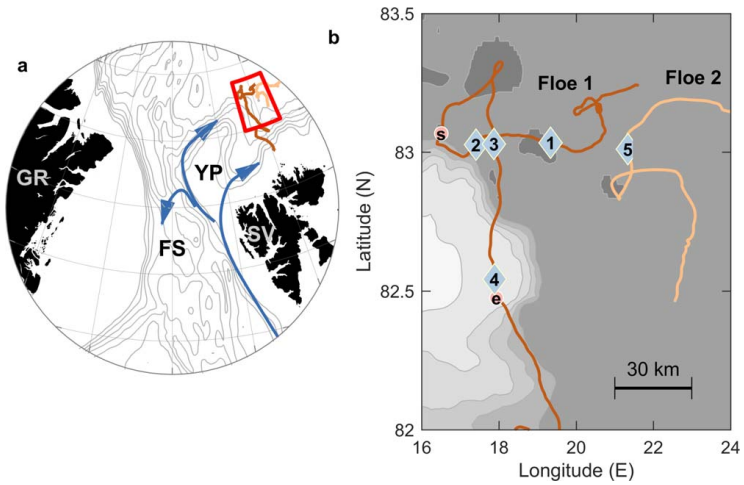

Figure 1. Location map and N-ICE2015 winter drift tracks. (a) The site in relation to Svalbard (SV), Greenland (GR), Fram Strait (FS), and Yermak Plateau (YP). The region marked in red is expanded in Figure 1b. Arrows show the main branches of warm Atlantic Water. Isobaths are drawn at 500 m intervals between 1000 and 6000 m using the 2 min global relief data (ETOPO). (b) Expanded view of the drift tracks (Floe 1, dark brown, and Floe 2 light brown) together with the microstructure locations (sets 1–5, diamonds), and the start and end location of the storm M2 (bullets with s and e). Isobaths are at 500 m intervals from 1 min ETOPO [*Amante and Eakins*, 2009].

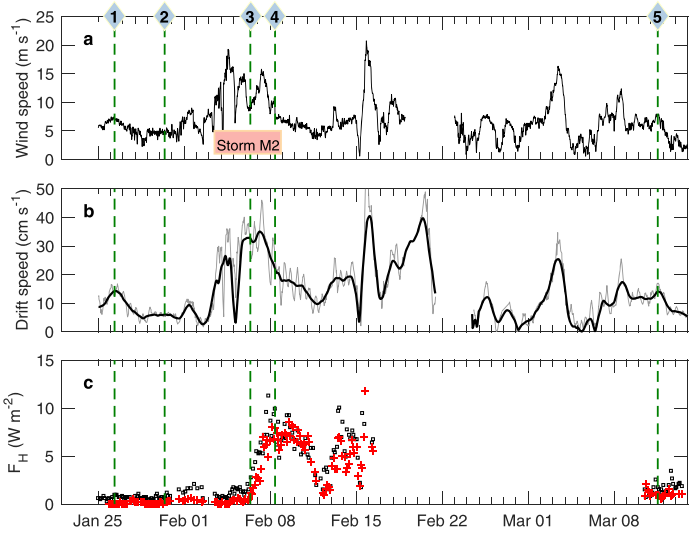

Figure 2. Conditions throughout the study period. Time series of (a) hourly-smoothed, 10 min averaged 10 m wind speed using merged ship-mast (adjusted from 24 m height to 10 m using the wind profile power law detailed in L. Cohen et al. (submitted manuscript, 2016)) and on-ice weather mast data, (b) instantaneous (gray) and filtered, background (black) ice drift speed after complex demodulation using diurnal and semidiurnal frequencies, and (c) turbulent ocean heat flux, F_H. Vertical dashed lines mark the times of microstructure sets 1–5 indicated on top. The storm period (M2) is highlighted in Figure 2a. No data are shown when the ship was repositioning in late February. Heat flux measurements are 3 h averages of 15 min covariances (black circles) and using a bulk parameterization (red).

2.1. Eddy-Covariance Measurements

Under-ice turbulence measurements were made using a TIC deployed 1 m below the ice undersurface. Detailed description of the setup is given by *Peterson et al.* [2017]. High-resolution time series measurements of 3-D velocity components and temperature are collected resolving the energy spectrum from energy containing eddies through the inertial subrange of turbulence. Calculations are based on 15 min segments over which the current components are rotated into the mean current direction (u), such that time averages of the cross-stream (v) and vertical (w) components vanish. The data set is systematically quality controlled before calculating momentum and turbulent heat fluxes (for details see *Peterson et al.* [2017]). Friction velocity at the measurement level is obtained from $u_*=[\langle u'w'\rangle^2+\langle v'w'\rangle^2]^{1/4}$, where primes denote deviation from the mean, and angle brackets denote temporal (15 min) averaging. Temperature measurements in the same measurement volume (2 cm^3) are used to calculate the vertical heat flux, $F_H=\rho c_p\langle w'T'\rangle$, where ρ is the density and c_p is the specific heat capacity of seawater. An alternative estimate of heat flux is obtained for each 15 min segment using a common parameterization dependent on temperature elevation above freezing and friction velocity as $F_{H,bulk}=\rho c_p \mathrm{St}\ u_*(T-T_f)$, where St = 0.0057 is the turbulent Stanton number [*McPhee*, 1992].

The subset of data used here comprises 2407 fifteen minute segments between 25 January and 14 March 2015, which were reduced to 1926 segments after quality control, corresponding to a total duration of approximately 20 days.

2.2. Microstructure Profiling

Vertical profiles of shear microstructure were obtained using an MSS90L profiler equipped with airfoil shear probes. Dissipation rate of turbulent kinetic energy (TKE) is calculated by integrating the vertical wave number spectrum of shear from each probe [*Lueck et al.*, 2002]. Estimates from each probe are corrected for the unresolved variance and a final value is obtained by averaging over the two probes. The processing methods are similar to earlier studies by our group [*Fer*, 2006, 2014] and are summarized in A. Meyer et al.

Table 1. Overview of Microstructure Profile Set Details

Set	Start Date (2015)	Start Time (UTC)	Lon (E)	Lat (N)	Duration (min)	Number of Casts
1	26 Jan	0828	19°20.2′	83°2.0′	45	4
2	30 Jan	0930	17°24.4′	83°1.6′	17	2
3	6 Feb	0847	17°52.2′	83°1.8′	9	3
4	8 Feb	0910	17°53.1′	82°32.6′	25	3
5	11 Mar	1300	21°20.1′	83°0.6′	25	2

(submitted manuscript, 2016). We use 1 m vertically averaged precision temperature and salinity profiles and vertical eddy diffusivity (K) profiles from this data set. The Conservative Temperature, Θ, and Absolute Salinity, S_A, are calculated using the thermodynamic equation of seawater [*IOC, SCOR, IAPSO*, 2010]. K is calculated using the *Osborn* [1980] model as $K=0.2\varepsilon N^{-2}$, assuming the common value of mixing efficiency. For well-mixed layers where N^2 approaches zero, the model is not applicable because it would lead to spuriously large values of K.

In the following analysis a subset of the microstructure profiles is used. The selected profiles are restricted to a region that justifies our assumption of vertical mixing by one-dimensional processes and exclude those affected by advection and proximity to AW. The idealized diffusivity profiles are constructed from 33 out of 45 sets (section 4.3). For numerical solutions, we concentrate on two pairs of profiles, each pair defining the initial and final profile to initiate and compare with the model result, respectively, for two cases separated by 7 days (sets 2 and 3) and 44 days (sets 1 and 5). Another profile (set 4) is used to emphasize the possible effects of advection or other 3-D processes. The details of the five sets of microstructure profiles used here are summarized in Table 1. Motivation for these choices is further given in section 3. Each set is an average profile over two to four casts conducted in a short duration of 10–45 min.

2.3. Salt and Enthalpy Budget at the Ice-Ocean Interface

The numerical solutions of the 1-D diffusion equations described in section 4 require external source terms for temperature and salinity at the upper boundary (ice-ocean interface). These source terms are obtained from the turbulent heat and salinity fluxes calculated from the enthalpy and salt balance at the ice-ocean interface in the under-ice boundary layer. A detailed description can be found in *McPhee* [2008, Chap. 6] and see also *McPhee et al.* [2008]. Here we summarize the sets of equations utilized in characterizing the ocean-ice interaction. The turbulent heat and salinity fluxes at the interface can be written in kinematic form as

$$\langle w'T'\rangle_0=\alpha_H u_{*0}(T_w-T_0), \tag{1}$$

$$\langle w'S'\rangle_0=\alpha_s u_{*0}(S_w-S_0), \tag{2}$$

where α_H and α_s are the turbulent exchange coefficients for heat and salt, respectively, and subscripts 0 and w indicate interface ($z=0$) and far-field seawater (typically in the mixed layer) values. The ratio, $R=\alpha_H/\alpha_s$, of the turbulent exchange coefficients is a measure of strength of heat transfer relative to the salt transfer, and hence of double diffusion. Note that the measurement level of 1 m is usually in the constant stress layer, such that friction velocity is representative of the ice-ocean interface stress. The interface friction velocity can also be approximated from the Rossby similarity drag relation [*McPhee*, 2008], when direct measurements are not available or representative of the drifting ice floe.

Isostatically balanced ice melt rate is $w_0=-(\rho_i/\rho)\dot{h}$, positive upward (melting conditions) where $\dot{h}$ is the ice growth rate (rate of change of ice thickness, positive for growing ice), ρ_i is ice density, and ρ is seawater density. The interface enthalpy conservation strikes a balance between conduction near the bottommost part of the ice, turbulent heat flux from the ocean, and latent heat from melting or freezing. In kinematic form (i.e., energy divided by ρ and specific heat capacity, c_p)

$$\langle w'T'\rangle_0-\dot{q}=w_0Q_L, \tag{3}$$

where the kinematic ice conduction is $\dot{q}=-\frac{k_i}{\rho c_p}\frac{dT_i}{dz}$; $Q_L=L_i/c_p$, and latent heat of fusion for sea ice, L_i, and thermal conductivity of sea ice, k_i, are both obtained from corrections to the fresh ice parameters [see *McPhee*, 2008]. The vertical gradient of ice temperature, $\frac{dT_i}{dz}$, close to the ice undersurface is the driver for conduction through the ice in the considered control volume.

The salt budget leads to a balance between the turbulent salinity flux from the ocean and the net vertical advection of salinity from ice melt or freeze

$$\langle w'S' \rangle_0 + w_0(S_i - S_0) = 0. \tag{4}$$

At the interface, it is often assumed that the salinity is determined by the freezing point temperature, e.g., $T_0 = T_f(S_0) = -mS_0$, with $m = 0.0549$. Finally, combining this set of equations, the so-called "three-equation approach" for the under-ice boundary layer leads to a quadratic equation for the interface salinity, S_0

$$mS_0^2 + aS_0 + b = 0, \tag{5}$$

with

$$a = T_w - \frac{\dot{q}}{\alpha_H u_{*0}} + \frac{Q_L}{R} - mS_i,$$

$$b = -S_i\left(T_w - \frac{\dot{q}}{\alpha_H u_{*0}}\right) - \frac{S_w Q_L}{R}.$$

In this study we use the three-equation approach to calculate the interface heat and salt fluxes at each time step of the numerical solutions and introduce these fluxes as source (or sink) terms into the diffusion equations (6), uniformly distributed over the mixed-layer depth. In summary (see also section 4.2), for prescribed values of S_i, dT_i/dz, R, α_H, u_{*0}, and mixed-layer temperature and salinity, we obtain the interface salinity S_0 from equation (5), and the interface temperature as the corresponding freezing point value. The interface heat flux follows from equation (1). Using the basal melt rate from equation (3), we finally obtain the salt flux at the interface from equation (4).

3. Observations

The period selected for analysis starts with calm conditions, weak winds of approximately 5 m s^{-1} and relatively slow ice drift velocity of about 0.05 m s^{-1}, persisting for 1 week duration, before the storm M2 picks up (Figure 2). We follow the definitions and characterizations of the N-ICE2015 experiment's storms provided by L. Cohen et al. (submitted manuscript, 2016). Start and end of storms correspond to periods when the 10 min averaged wind speed (at 10 m) was greater than 8 m s^{-1} continuously for at least 1 h in a time period of at least 3 h. A major storm (such as M2) is when the rate of pressure decrease exceeds 5 hPa in 6 h. Prior to the storm, oceanic heat fluxes in the under-ice boundary layer are close to the instrument lowest detection level and generally less than 1 W m^{-2} (Figure 2c). After 2.5 days into the storm, the oceanic fluxes start to increase gradually, reaching a peak value of 11 W m^{-2} 4.4 days after the storm starts, and remain large (>5 W m^{-2}) for approximately 2.5 days after the storm ceases. Heat fluxes return to low levels and then increase abruptly when the floe drifts over warm AW after February 11. The average value representative for the "high flux" period is 7 W m^{-2}, calculated between 2 and 11 February. The heat flux measurements from Floe 2 are limited, with 247 fifteen minutes segments between 10 and 14 March (approximately 2.5 days), which have an average heat flux of 2 W m^{-2}.

Wintertime heat fluxes observed here can be compared to available heat flux estimates from previous Arctic studies. In the Canada Basin, *Cole et al.* [2014] report time averaged (October 2009 to April 2010, ± one standard deviation) heat flux of 1.0 (±2.9) W m^{-2} based on covariance measurements at 6 m below ice. During the SHEBA drift in the Beaufort Gyre, average winter under-ice surface heat flux was 1.0 W m^{-2} [*Shaw et al.*, 2009]. Estimates using bulk parameterizations ($F_{H,bulk}$ described in section 2.1) were reported using data from drifting buoys. *Krishfield and Perovich* [2005] conclude that $F_{H,bulk}$ is not negligible in winter, but averages less than 2 W m^{-2} in the Beaufort Gyre and is approximately 3 W m^{-2} in the Transpolar Drift. *Jackson et al.* [2012] report that through winter, the average mixed-layer temperature is often marginally above the freezing temperature, leading to typical heat fluxes of the order 1.0 W m^{-2}. Storms during winter, however, result in events with heat flux of 10–50 W m^{-2}, primarily as the release of heat from the near surface temperature maximum (NSTM), which delays the sea ice growth and episodically melts sea ice during winter [*Jackson et al.*, 2012]. These high flux events are comparable to, but larger than the average value in our high flux period, probably because of the lack of a NSTM in our study region.

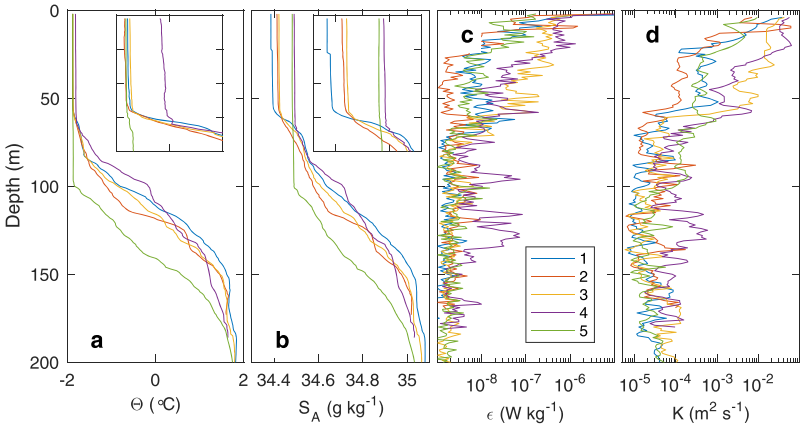

Figure 3. Vertical profiles from sets 1 to 5, measured by the microstructure profiler. Each profile is an average over several casts in the set (see Table 1). Missing values of K in weakly stratified segments are linearly interpolated. Insets are enlarged views in the upper 80 m, with ticks 20 m in the vertical and 0.1°C or 0.1 g kg^{-1} in the horizontal.

In the analysis period, the microstructure profile sets 1–5 (Figure 2 and Table 1) are chosen for discussion. These sets correspond to sets number 2, 5, 11, 12, and 37 of the cruise log. The choice of the sets is motivated by our goal to restrict the analysis to regions where the oceanic response can be attributed to vertical mixing through 1-D processes, forced by wind and affected by surface buoyancy fluxes induced by melting or freezing. Profiles of temperature, salinity, dissipation rates, and eddy diffusivity for sets 1–5 are shown in Figure 3. Sets 1 and 5, separated only by 30 km but 44 days in time, are located in the deep Nansen Basin, unaffected by the presence of AW branch or topography. Sets 1 and 2, on the other hand, are affected by the presence of a front or advection since the substantial increase of salinity in the upper 100 m (Figure 3, insets) in this short time span cannot be explained by vertical processes alone (see sections 5 and 6). Sets 2 and 3, however, are approximately colocated, separated by 1 week duration, with no influence of advection apparent in the temperature and salinity profiles. The profiles of temperature and salinity from sets 3 and 4 show a striking evolution during the storm and swift-drift period where the Absolute Salinity in the mixed layer increases by 0.07 g kg^{-1}, and Conservative Temperature by 0.06°C in two days. Strong vertical mixing during storm leads to rapid and substantial entrainment of warm and saline waters into the mixed layer; however, the increase in Θ and S_A in the mixed layer cannot be explained without including frontal or advection processes. Sets 2 and 3 and sets 1 and 5, on the contrary, are colocated and away from AW influence or fronts; hence, we can study the change in the heat content and salinity using 1-D mixing and entrainment of AW from below.

As further confirmation of the 1-D balance and that mixed-layer temperature and salinity changes are largely due to vertical entrainment, we calculate the change in Θ and S_A averaged between the ice-ocean interface and the $\sigma_\theta = 27.75$ density surface (typically located between 100 and 135 m), between pairs of sets. The choice of a deep isopycnal integrates the effects of mixing at the base of the mixed layer. Because mixing results in a redistribution of water properties vertically, as opposed to a net change, small changes in Θ and S_A indicate dominantly vertical processes whereas relatively large values imply important effect of advection and other processes. For sets 1–5 and 2–3 (used for the 1-D numerical solutions), the change in Θ and S_A is less than 10^{-3} °C d^{-1} or 10^{-3} g kg^{-1} d^{-1}, whereas these values increase by a factor of 5–10 for sets 1–2 and sets 3–4.

In section 5, we first present the evolution from set 2 to 3, a period spanning from calm conditions to 3 days into the storm M2. Next, we concentrate on set 1 to 5 in the Nansen Basin, reproducing the vertical structure of set 5 using 1-D processes, after 44 days of forcing applied to the initial profile, set 1.

4. One-Dimensional Solutions

4.1. Diffusion Equations

We formulate and obtain the solutions for the hydrography in terms of potential temperature, θ, and salinity, S, to be consistent with ice thermodynamics calculations. The solutions are then converted to S_A and Θ for presentation and comparison with observations. One-dimensional diffusion equations for θ and S are

$$\frac{\partial \theta}{\partial t} = \frac{\partial}{\partial z}\left(K\frac{\partial \theta}{\partial z}\right) + S^{\theta},$$
$$\frac{\partial S}{\partial t} = \frac{\partial}{\partial z}\left(K\frac{\partial S}{\partial z}\right) + S^{S}, \tag{6}$$

where all variables, including vertical diffusivity, K, are functions of time, t, and depth (vertical distance from ice, positive upward), and $S^{\theta,\ S}(t,z)$ are the external sources (or sinks) for temperature and salinity (e.g., as a result of heat lost to ice melt or salinity release by freezing, calculated from the ice thermodynamics and described in detail in section 4.2). Solutions are obtained starting from given initial profiles of θ and S, using 1 m vertical and 1 h temporal resolution. At the upper boundary, we apply zero flux (ice-ocean fluxes of heat and salt are distributed over the mixed layer via the source terms, see section 4.2), and at the lower boundary, the bottommost (θ, S) value from the previous time step. Solutions at the final time step of the duration of interest are compared to the observed profiles (the time evolution is not presented). Final profiles are not sensitive to a factor of 2 change to time step or vertical resolution; further sensitivity to different parameter choices is discussed in section 6. Calculations of the source terms and the prescribed K profiles are described in the subsequent subsections.

4.2. Calculations of the Source Terms

The source terms are obtained from the ice thermodynamics, using the interface heat and salt fluxes from the three-equation approach (section 2.3). Temperature gradient in the lowest part of the ice is assigned using temperature profiles from ice core measurements (Figure 4). While there are differences in ice temperature profiles from different floes, the vertical gradient in the bottommost 25 cm is similar, and a line fit to data from three cores yields $dT_i/dz = -5$ K m^{-1}. We assume ice salinity $S_i = 7$ and use the typical temperature near the bottom of ice cores of $T_i = -2.1$°C. We use $R = 33$ and $\alpha_H = 1.3 \times 10^{-2}$ inferred from direct flux measurements in March north of Svalbard [*Sirevaag*, 2009], which are likely representative of the conditions studied here (sensitivity results are given in section 6). The friction velocity, u_{*0}, is obtained from

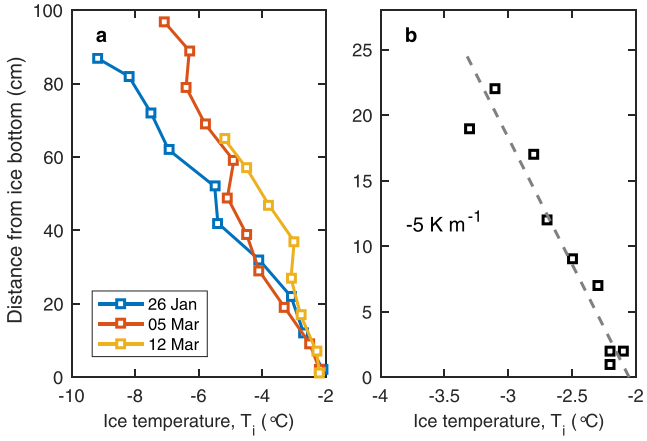

Figure 4. Profiles of ice temperature obtained from ice cores [*Gerland et al.*, 2017]. (a) Entire profile with distance referenced to ice bottom, and (b) zoom in to the bottommost 25 cm together with a least squares fit to a first order polynomial. The slope indicates the estimated ice temperature vertical gradient close to the ice-ocean interface.

the Rossby similarity using the filtered drift speed (removing diurnal and inertial variability) and common values of $A = 1.91$, $B = 2.12$, and $z_0 = 10^{-2}$ m [*McPhee*, 2008]. We do not use the friction velocity measured by the TIC because there is a large gap in the covariance data set between 16 February and 10 March, and also because the floes drift over waters and regions where processes other than vertical mixing can be important, which will have signature on the covariance measurements. By using Rossby similarity and the filtered drift speed, we obtain a more representative forcing for the basin conditions. Using calculations from periods when both estimates are available, average (± one standard deviation) value over daily, half-overlapping windows is 0.007 (±0.004) m s^{-1} for the Rossby similarity and 0.005 (±0.002) m s^{-1}, for the covariance calculations.

Given dT_i/dz, R, α_H, u_{*0}, $m = 0.0549$, and the far-field (at 10 m, in the mixed layer) temperature and salinity, we obtain the interface salinity, S_0, from equation (5). Interface temperature is the corresponding freezing point value, and the interface heat flux follows from equation (1). The basal melt rate, w_0, is then calculated from equation (3) and the salt flux at the interface from equation (4). The resulting interface heat and salt fluxes at each time step are introduced as source (or sink) terms into the diffusion equations (6), uniformly distributed over the mixed-layer depth. For example, during freezing conditions the interface salt flux is a source of salinity to the mixed layer, whereas a positive heat flux (upward across the ice-ocean interface) is a sink for the temperature in the mixed layer. The depth of the mixed layer (z_{ML}) is obtained as the depth where the salinity exceeds the top 2 m average value by 0.1 g kg^{-1}. This method is very similar to the definition from *Peralta-Ferriz and Woodgate* [2015] who used a threshold criterion of potential density of 0.1 kg m^{-3} (for the mixed-layer salinity and temperature values in this study, the salinity excess of 0.1 g kg^{-1} corresponds to approximately 0.08 kg m^{-3}). Increasing and reducing the threshold by 0.05 g kg^{-1}, respectively, leads to 9 m deeper and 5 m shallower z_{ML}, on average. The heat sink term obtained from this calculation is taken up by the ice for melting. This is only a fraction of the oceanic heat delivered to the surface and is accounted for as described in section 4.4.

4.3. Idealized Diffusivity Profiles

We construct idealized profiles of K, from the microstructure measurements collected in the vicinity of sets 1–5, and exclude locations where topography, proximity to AW, and ice edge can affect the vertical mixing (A. Meyer et al., submitted manuscript, 2016a). The stations used are marked in the inset of Figure 5. We use

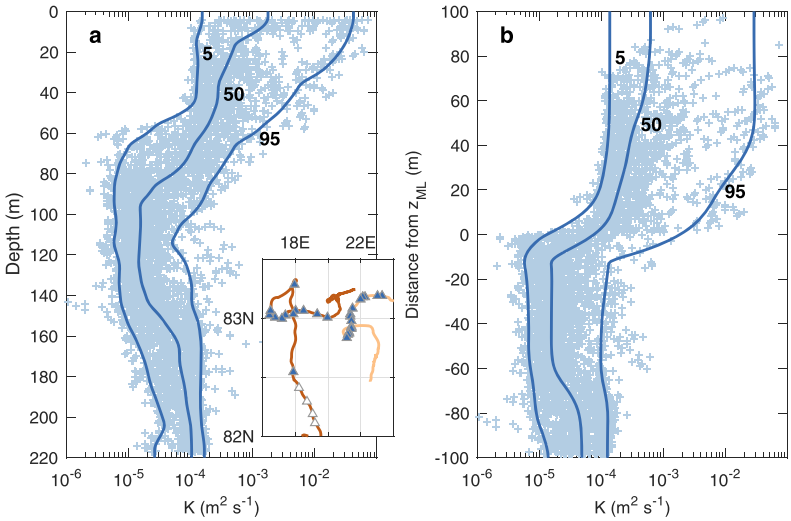

Figure 5. Idealized eddy diffusivity profiles with vertical axis referenced to (a) depth (relative to underside of ice) and (b) distance relative to the base of the mixed layer. Positive values are upward, increasing toward the underside of ice. The profiles from Figure 5b are used in the numerical solutions. All data points from set-averaged profiles (each set includes two to five subsequent casts) are shown (crosses) together with the 5, 50, and 95 percentiles in 10 m thick vertical bins (thick lines). The inset shows a zoom in to the drifts of Floes 1 and 2, all microstructure set positions (white triangles) and the sets used in deriving the idealized profiles (blue triangles).

33 sets out of the 45 collected between 25 January and 14 March 2015: 12 sets (43 casts) from Floe 1, and 21 sets (49 casts) from Floe 2. All K measurements from these sets are shown in the profiles of Figure 5a together with 5, 50, and 95 percentiles in 10 m vertical bins. The vertical diffusivity averaged vertically down to the base of the mixed layer correlates with wind stress, hence u_{*0} (correlation coefficient between wind and $\log_{10}(K)$ is $r = 0.66$, with 34 data points). We therefore can use wind forcing to assign K profiles selectively averaged to be representative of weak, normal, and strong forcing conditions. We use thresholds 5 and 15 m s^{-1} to delineate weak (less than 5 m s^{-1}) and strong wind (greater than 15 m s^{-1}) conditions, approximately corresponding to the 5 and 95 percentiles between 25 January and 14 March 2015. The weak, moderate, and strong wind conditions are represented by the diffusivity profiles K_5, K_{50}, and K_{95}, respectively. The sensitivity to K is presented in section 6. At every hour, the wind speed averaged over the preceding 12 h is used to pick the K profile. The friction velocity is the time average of hourly values over the same 12 h window. The friction velocity used is consistent with the subinertial Rossby similarity approach because we used filtered (demodulated using 24 and 12 h period) drift velocity. The time average is preferable to the instantaneous wind speed and u_{*0}, given the idealized nature of the forcing, and that the K profile should be representative of the temporal history of wind forcing.

The depth of the mixed layer (z_{ML}) varies, and the vertical reach of elevated mixing should be accounted for in assigning time-variable K profiles. We therefore reference the vertical distance to the depth of the mixed layer ($z_r = z_{ML} - z$, positive upward) for each profile and calculate K_5, K_{50}, and K_{95} in 10 m thick bins. Bins with less than 25 data points are excluded. The resulting profiles are then interpolated to 1 m vertical resolution (of z_r) and smoothed over 5 points. One-dimensional solutions are obtained by using these profiles, after mapping z_r onto the actual depth, using the mixed-layer depth from the previous time step.

4.4. Other Details

In order to be consistent with ice thermodynamics calculations, the initial S_A and Θ profiles are converted to salinity in practical scale and potential temperature, and converted back to Absolute Salinity and Conservative Temperature after solving the diffusion equations, in order to compare with the final profiles of set 3 or 5 as applicable.

A positive interface heat flux obtained from the calculations described above is the amount required by ice melt at the ice-ocean interface. The heat sink in the mixed layer can be larger, particularly if additional sensible heat is lost to atmosphere, through the ice or through leads. Thin sea ice and open water cause vigorous surface fluxes compared to the drift station in complete pack ice, in winter leading to increased salt flux into ocean and sensible heat loss to the atmosphere [*Maykut*, 1982]. *Maykut and McPhee* [1995], using data from the AIDJEX experiment, show that heat extracted from the ocean varies largely (35%) between stations separated by 100–200 km, with the main source of variability attributed to the amount of opening by dynamic activity of the sea ice. Only a fraction ϕ of the mixed-layer heat content is thus lost to ice melt. Over a homogeneous ice field (i.e., excluding the heat loss through openings and leads), *Rudels et al*. [1999] suggested a natural control mechanism whereby ϕ is optimized to keep the ice melt rate at a minimum. Using the temperature difference between upper layer and the warm layer below, ΔT, and the salinity of the warm layer, S_w, the fraction of heat going to ice melt is

$$\phi = \frac{2\alpha L}{c_p(\beta S_w - \alpha \Delta T)}, \tag{7}$$

where α and β are the thermal expansion and haline contraction coefficients of seawater, respectively, and L is the latent heat of melting. For $S_w = 34.9$ and $\Delta T = 3°C$, ϕ is approximately 0.16. In the calculations, at each time step, the heat sink is multiplied by $1/\phi$. The salinity source term is applicable only when there is ice freezing and convection. For these conditions, we assume convection occurs over a fraction, F, of the representative area and multiply the salinity source term by a factor of $F = 0.6$ (chosen because of better agreement with observations; sensitivity is discussed in section 6).

The imposed fractions ϕ and F lead to a mixed layer that cools more and freshens less than what ice-ocean heat and salt fluxes would prescribe. This adjustment, however, is crucial because (i) the upper ocean heat content is not controlled by the heat loss to ice melt alone, but also includes a part that is lost to the atmosphere, and (ii) neither heat loss nor convection occurs homogenously over an area representative of the study site. Leads in the pack ice allow rapid ice formation and escape of oceanic heat to the atmosphere.

During the study period, leads opened up sporadically and quickly refroze (P. Itkin et al., Thin ice and storms: A case study of sea ice deformation from buoy arrays deployed during N-ICE2015, submitted to *Journal of Geophysical Research*, 2016), such that we deem their contribution to regulating surface heat and salt fluxes crucial.

5. Results

Over the 1 week that separates sets 2 and 3, the mixed-layer depth remained approximately constant at 58–60 m, the mixed-layer averaged temperature increased by 0.01°C, and salinity by 0.007 g kg^{-1}. The vertical profiles of Θ and S_A are compared to the numerical solution after 7 days in Figure 6 (compare orange and red curves). The evolution can be explained by vertical processes dependent on our choice of parameters and the sensitivity discussed in section 6. The evolution between sets 1 and 5 over 44 days are more striking (Figure 7). Mixed-layer depth increased from 56 to 100 m, and the pycnocline deepened by approximately 20 m. Mixed-layer salinity has increased by 0.094 g kg^{-1} while temperature increased by 0.002°C, staying close to freezing. In both cases, the changes in the mixed layer are well replicated by the one-dimensional model. A shortcoming of the numerical solution is the lack of a vertical convective adjustment scheme to ensure a sharp mixed-layer base. The vertical diffusivity leads to a diffuse transition from the mixed layer to the pycnocline; the temperature and salinity characteristics in the upper half of the mixed layer, however, are in very good agreement with the observations. The discrepancy between the observed and modeled depth of the pycnocline can be considered to be within the short-term variability such as internal waves.

A direct comparison with a snapshot observed profile suffers from not sufficiently averaging over internal wave displacements and other short-term variability. In order to account for the vertical heave inherent in the observations, in Figures 6 and 7 we destrain the observed profiles by linearly stretching or squashing the vertical coordinate to maintain the $\sigma_\theta = 27.75$ density surface at a fixed depth (of the initial profile, 105 m for set 1 and 117 m for set 2). This isopycnal is chosen to be close to z_{ML} but away from the effects of mixing at the base of the mixed layer. This procedure assumes that internal wave and eddy displacements are zero at the surface and increase linearly with depth below—a reasonable approximation in the upper water column. Destraining results in upward displacements of -7 and -2 m in the final profile of observation and model, respectively, for the 7 day run, and 25 and 13 m for the 44 day run. In the figures we also indicate a typical vertical displacement of the pycnocline of ± 10 m for reference. This is 3–5 times less than

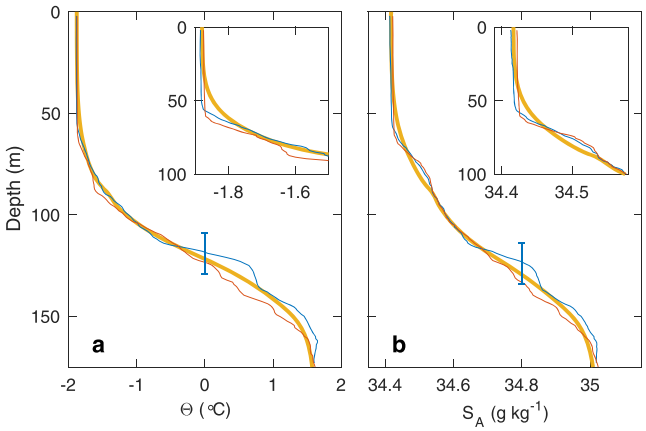

Figure 6. Vertical profiles of (a) Conservative Temperature and (b) Absolute Salinity for set 2 (initial condition, 30 January, blue), set 3 (6 February, red), and the solution obtained from the time-dependent diffusion equations over the time separation of approximately 7 days (thick orange curve). The insets zoom in to the upper 100 m. The vertical error bar is placed arbitrarily to indicate, for reference, a typical ± 10 m vertical displacement of temperature and salinity surfaces from internal waves. The vertical axis is the depth for the initial profile, but destrained (see text) depth for the final profiles.

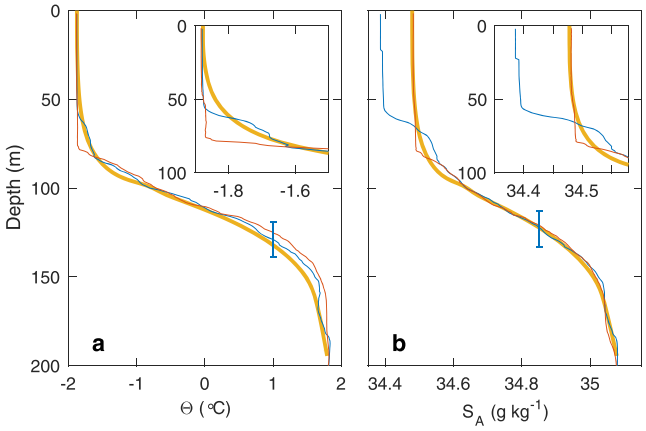

Figure 7. Same as Figure 6 but for set 1 (blue) and 5 (red). Time separation is approximately 44 days.

the vertical displacements observed in the upper 200 m over the southern Yermak Plateau [*Fer et al*., 2010], and can be considered as a representative value for the study area. In the Canada Basin, typical vertical displacements are smaller: Using ice-tethered profiler data for years 2005–2014, *Dosser and Rainville* [2016] obtain typical wave amplitudes (for near-inertial waves below the mixed layer, in the upper 200 m) that decrease from approximately 2 m to less than 1 m between 72°N and 82°N latitude.

Over the 44 day simulation period, vertical mixing was forced 15% of the time by weak wind (K_5 profile) and 7% of the time strong wind (K_{95} profile) conditions. Main results for this experiment are summarized in Table 2. Salinity increase in the mixed layer was 0.1 g kg^{-1} (very close to the observed value); 10% of this is attributed to increase from brine release during freezing, calculated from the salinity source term. Because we do not apply convective adjustment, but simply distribute the salinity source throughout the mixed layer, the remaining 90% can be attributed to entrainment from beneath the mixed layer. Freezing conditions ($w_0 < 0$) occurred 70% of the time. Over the freezing periods, w_0 averaged to -1.2 (± 0.5) 10^{-8} m s^{-1}, or -0.10 (± 0.05) cm d^{-1}. This can be compared to the total (ice and snow) thickness growth estimates from transects on Floes 1 and 2 (Figure 8). The observed ice and snow thickness growth rate (not identical to w_0) is 3–4 times larger. This is not conclusive as the discrepancy can be accounted for, for example, by an increase in snow thickness, but suggests that the model produces growth rates of the right order. Melting conditions occurred in response to strong entrainment events during strong wind forcing, in four abrupt episodes, two events during storm M2, and between 15 and 16 February and 3 and 4 March. Averaged over melting periods, w_0 was 0.3 (± 0.2) cm d^{-1}. Salinity increase in the mixed layer due to entrainment from below during these episodes accounted for 70% of the total increase (Table 2).

Table 2. Overview of Results From the 44 Day Run[a]

	Total	Freezing Periods	Melting Periods
Duration (day)	44	70%	30%
w_0 (cm d^{-1})		−0.1	0.3
$\Delta\Theta$ (°C)		40%	60%
0–25 m	0.005		
0-z_{ML}	0.090		
ΔS_A (g kg^{-1})		30%[b]	70%
0–25 m	0.092		
0-z_{ML}	0.100		

[a]Total increase in the Conservative Temperature and Absolute Salinity relative to the initial profile, averaged over the upper 25 m or over the mixed-layer depth, z_{ML}, over the total duration are listed together with corresponding percent increase over the freezing and melting periods only. The percent of time with freezing and melting conditions, and the corresponding average basal melt rates, w_0, are also given.
[b]Of the 30%, 10% is due to brine release (from the source term) and 90% from entrainment because of vertical mixing.

As a consequence of the diffuse mixed-layer base, the lower part of the mixed layer shows a signature of elevated entrainment of heat and salt compared to

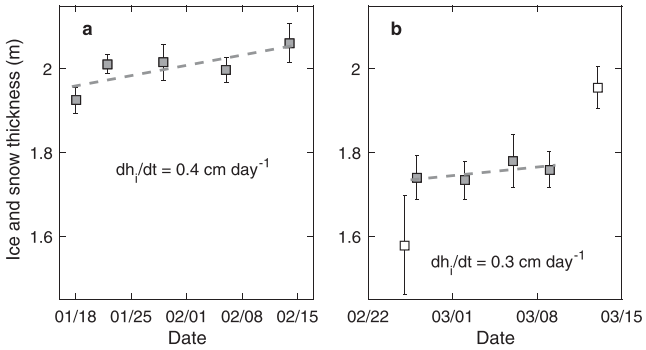

Figure 8. Total ice thickness (ice plus snow) growth rate estimates from electromagnetic induction sounding transects [*Rösel et al.*, 2016] on (a) Floe 1 and (b) Floe 2. Only subsets of floe data relevant to this study are used (e.g., Floe 1 excludes the part when drifting over Atlantic Water and transects over first year ice). Data points are the median values of typically 1000 measurements obtained from one transect. Error bars are standard errors assuming (arbitrarily) every 100th data point is independent. Linear least squares fits are shown together with the slope. The open markers in Figure 8b are excluded from the fit because those surveys include various types of ice and are not representative of the standard repeat transect.

the observations. Averaged over the mixed layer, temperature increase is 0.09°C, much larger than the observed 0.002°C, primarily due to the increase in the lower part of the mixed layer. When averaged only in the uppermost 25 m, the temperature increase is 0.005°C, much closer to the observations. The corresponding figure for salinity is 0.092 g kg^{-1}, in excellent agreement with observations (0.094 g kg^{-1}), and only slightly lower than the full mixed-layer depth average of 0.1 g kg^{-1} from the model. This suggests that the effect of diffuse mixed-layer base does not influence salinity as much as it does temperature, which is probably explained by the under-ice boundary layer temperature kept at freezing point. This constraint maintains a large mixed layer to pycnocline temperature difference. On the other hand, the relatively saline pycnocline water is entrained and redistributed into the mixed layer, reducing the mixed layer to pycnocline salinity difference relative to the initial state, leading to a thinner diffuse salinity layer.

6. Sensitivity

The calculations using the simplified model are based on choices of several parameters that deserve a sensitivity analysis. The aim of the additional calculations presented here with altered values of selected parameters is not to assess the upper ocean response to perturbations (such as freshening, increased forcing, etc.), but to identify how sensitive our results and findings are to a large (factor of 2–10) change on the choices made. The parameters can be grouped in relation to ice-ocean interface and thermodynamics (ice temperature gradient, heat exchange coefficient, and double diffusion strength), forcing (wind and vertical diffusivity), and fractions relating to leads and openings. Wind speed does not come directly into the analysis, but is used as a proxy for the vertical diffusivity chosen to be dependent on the wind speed. We therefore present detailed cases of sensitivity to vertical diffusivity.

The double diffusion strength imposed by R does not lead to notable changes in the mixed-layer temperature and salinity properties (Figure 9). The results however are sensitive to the heat exchange coefficient: a reduction of α_H by a factor of 2 leads to warmer temperatures by 0.028°C (averaged in the upper 50 m); while this does not affect the salinity, doubling of α_H leads to slightly higher (0.005 g kg^{-1}) salinity. Overall, the choices of α_H and R thus do not affect our results significantly.

Vertical diffusivity, on the other hand, changes the vertical structure significantly. We tested idealized profiles of K (time dependent, chosen using the same wind speed thresholds), multiplied by a factor of 5 and by a factor of 0.2, for the entire water column, as well as a factor of 5 increase only in the mixed layer (5 × K-ML in Figure 10). Additionally, we obtained solutions for time-constant K prescribed by the moderate K_{50} profile, independent of the wind speed. The results are summarized in Figure 10. Strong vertical mixing leads to substantial deepening of the mixed layer and entrainment into the mixed layer, exceeding the

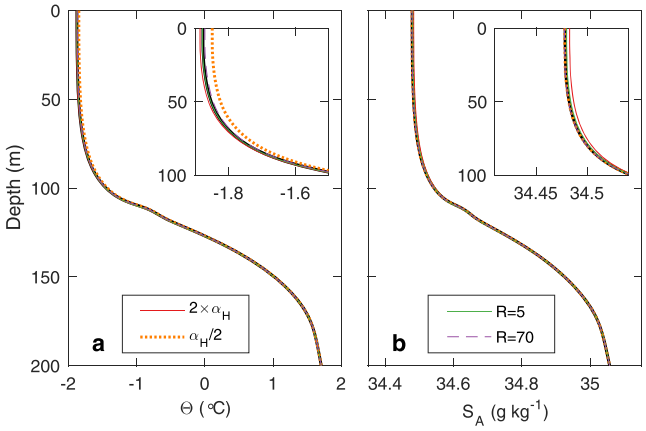

Figure 9. Sensitivity to parameters α_H and R. Profiles of (a) Conservative Temperature and (b) Absolute Salinity are shown. Black line, not included in the legend, is the reference solution shown in Figure 7. The legends are valid for all panels. The axis limits are the same for Figures 9–11 but note that the limit of the salinity inset is different than in Figure 7.

observed values by a large factor, particularly for salinity estimates (see Figure 10b, light green trace off scale in the inset). Entrainment is less when only the mixed layer K is increased; however, the final profile is still inconsistent with the observations. The constant K_{50} profile results in a shallower mixed layer compared to the observations (or to the reference solution in black which captures the observations fairly well). The sensitivity analysis implies that the time variable, wind-dependent K forcing is needed to faithfully capture the evolution in the upper water column.

Finally, the sensitivity of the results to the prescribed temperature gradient in the lower part of ice, and to the choices of fractions ϕ and F, is examined (Figure 11). Compared to the role played by vertical diffusivity, the effect of these parameters in the salinity profile is small, but slightly more important than the effect of α_H and R. When brine rejection is allowed in the entire surface area ($F = 1$), the salinity in the mixed layer is

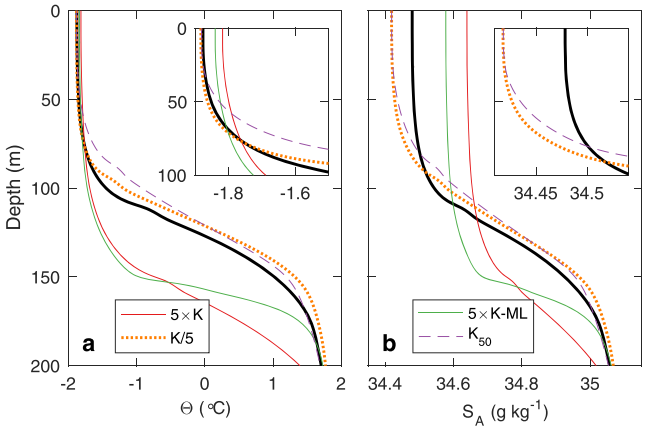

Figure 10. Same as Figure 9 but for sensitivity to vertical diffusivity. Solutions are obtained for 5 and 1/5 times the reference K profile, which is time variable and dependent on the wind speed, and for the reference K profile increased by a factor of 5 in the mixed layer only (5×K-ML). Additionally the solution is presented for a constant diffusivity profile equal to K_{50}.

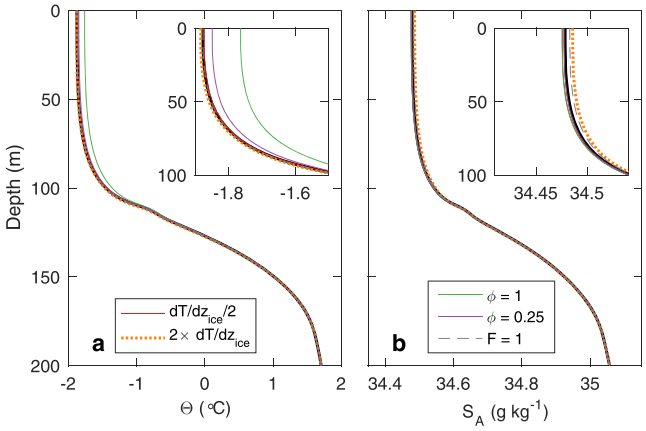

Figure 11. Same as Figure 9 but for sensitivity to ice temperature gradient, fraction ϕ, and the area fraction F.

0.005 g kg^{-1} larger. Doubling of the ice temperature gradient leads to even higher salinities (Figure 11, increase of 0.007 g kg^{-1} from the reference case). Of the parameters related to thermodynamics, double diffusion and area fractions, the fraction ϕ controls the mixed-layer temperatures. This is induced through control on the heat source term. When all of the heat available is allowed to melt sea ice ($\phi = 1$), temperature in the mixed layer is warmer by more than 0.1°C.

7. Discussion

Three essential features evolve from set 1 to 5: Salinity in the mixed layer increases, the mixed layer deepens, and the upper halocline freshens (Figure 7). Set 5 was located further away from the Yermak Plateau and from the influence of AW, compared to set 1. We therefore expect set 5 to be affected by certain trends: First, AW is expected to lie deeper at set 5, and second, winter mixed layers become increasingly deeper as one moves away from the immediate margins of the Eurasian Basin [*Meyer et al.*, 2017]. However, the increased influence of less saline Arctic water masses away from the basin margins would imply a relatively fresh mixed layer; the opposite is clearly the case, and this feature can thus not be explained as a consequence of spatial variation.

Our 1-D modeling captures all of these three features. We are thus confident that the majority of the change from set 1 to 5 is temporal. The rather small dependence of the model results on ice-ocean interaction related parameters further indicates that the bulk of the time evolution stems from diapycnal mixing in the water column. In fact, brine rejection from freezing ice accounts for only 10% of the mixed-layer salinity increase. The entrainment into the mixed layer is dominated by winter storms (>15 m/s; see Figure 2) rather than by buoyancy fluxes at the ice-ocean interface. A similar observation was made in the cold wake of a hurricane where most of the sea surface temperature change was due to entrainment by vertical mixing rather than air-sea heat fluxes [*D'Asaro et al.*, 2007].

The simple model applied here can be compared to more physically and dynamically based (e.g., on gradient Richardson number based mixing) models such as the Price-Weller-Pinkel [*Price et al.*, 1986] model with superimposed thermodynamics sea ice layer applied to summer and winter cases in the central Canada Basin [*Toole et al.*, 2010], or the local turbulence closure scheme of *McPhee* [1999]. The ability of the simple one-dimensional model to describe the observed evolution of the upper water column supports the hypothesis that in Arctic basins away from the ice edge, warm boundary currents and significant freshwater input, vertical processes are primarily responsible for shaping the temperature and salinity distribution, rather than lateral movement of water masses. Lateral mixed-layer restratification processes were observed to

be active in the Canada Basin [*Toole et al*., 2010], e.g., due to eddies in the upper water column [*Timmermans et al*., 2008], which cannot be captured by any of the one-dimensional models. Since observations reported here were made in winter, freshwater from sea ice melt is not considered. In spring and summer, however, freshwater increases stratification in the surface layer, which inhibits mixing. During melting conditions, the influence of double diffusion increases, significantly reducing the ocean-to-ice heat flux [*McPhee et al*., 1987; *Sirevaag*, 2009]. Our sensitivity results, however, do not show substantial changes in the mixed-layer temperature and salinity for a wide range of R and a factor of 2 change of the heat exchange coefficient.

In the Eurasian Basin, the perennial pycnocline is a bottleneck for the mixing of tracers between the mixed layer and the underlying warm and nutrient-rich AW. Thus in the Atlantic sector of the Arctic Ocean, nutrient fluxes are subject to similar dynamics as heat fluxes, and we can expect similar patterns for the vertical nutrient flux and the heat flux. Our results give indications on how much halocline water was entrained into the mixed layer between sets 1 and 5. As *Randelhoff and Guthrie* [2016] noted, in the Atlantic inflow area to the Arctic ocean, nitrate concentration is mixed conservatively with density over the relevant depth range; the same holds for nitrate concentration as a function of salinity. Regression of nitrate concentration against Absolute Salinity determined from a CTD bottle cast on 26 January, the same day the microstructure set 1 was sampled, shows excellent correlation ($R^2 = 0.99$, S_A range between 34.4 and 35.1, nitrate concentration range between 4 and 15 μM, variance of residual is 0.2 μM^2). Our results on entrainment of salinity and heat are directly applicable to entrainment of nitrate without further consideration of possibly not colocated pycnoclines and nutriclines as is the case, e.g., in the Canadian Basin. We can thus argue for a correlation between the upward flux of nutrients and the mixed-layer salinity increase due to entrainment during the same period.

The large mixed layer deepening from 60 to 100 m between set 1 and 5, and entrainment were dominated by the few winter storms which lead to upper pycnocline dissipation rates far above the usually rather quiescent values observed in the Arctic Ocean [*Fer*, 2009, 2014]. *Polyakov et al*. [2013] estimate an annual average upward heat flux of 1 W m^{-2} from the upper pycnocline in the central Eurasian Basin, and contrast this with a January–April average of 3–4 W m^{-2}. This corroborates a substantial seasonal cycle in entrainment of Atlantic Water. Similarly, enhanced vertical mixing (from storms and convection) through fall and winter has been shown to be a major driver in the seasonal replenishment of upper ocean heat and nutrient inventories [*Nishino et al*., 2015; *Randelhoff et al*., 2015, 2016]. *Randelhoff and Guthrie* [2016] report back-of-the-envelope calculations of convective entrainment of nitrate assuming that the wintertime brine rejection balances summertime sea ice melt. Our results indicate that wind-driven entrainment (as opposed to brine rejection induced, convective entrainment) can in fact contribute significantly to the annual mixed-layer density budget. For the N-ICE2015 study area, this has two implications. First, the convection driven entrainment is presumably even smaller than that given by *Randelhoff and Guthrie* [2016]. Second, upper halocline waters have to be renewed either through a convective-advective mechanism [*Rudels et al*., 1996] to achieve an interannual steady state, or by upward diffusion of deeper halocline waters during summer when surface meltwater restricts vertical mixing to above upper halocline waters [*Randelhoff et al*., 2017].

8. Concluding Remarks

A one-dimensional model is presented to describe the evolution of the hydrography in the upper 200 m in the Atlantic sector of the Arctic Ocean, in the Nansen Basin north of Svalbard. The model is forced by idealized, time-dependent vertical diffusivity profiles inferred from microstructure measurements. Two pairs of stations are examined, separated by 7 and 44 days in time, respectively, when the effects of advection and lateral processes were negligible. The model reproduces the observed changes well for both sets. The deepening of the pycnocline over 44 days is qualitatively captured by the model; however, the base of the mixed layer is diffuse compared to the observed profiles. The changes observed in the two pairs of stations in the Nansen Basin are dominated by vertical mixing processes. The sensitivity analysis implies that the time variable, wind-dependent forcing is needed to faithfully capture the evolution in the upper water column.

For the studied period between 26 January and 11 March 2015, 10% of the salinity increase in the mixed layer is attributed to increase from brine release during freezing which occurred 70% of the time, whereas the remaining 90% can be attributed to entrainment from beneath the mixed layer. Melting conditions occurred

in response to entrainment events during episodic strong wind forcing. Salinity increase in the mixed layer during these episodes accounted for 70% of the total increase. We conclude that the increase in salinity as a result of freezing is significantly less than that due to entrainment (approximately 10% versus 90%), and the latter is affected by episodic wind events (70% versus 30%). The study is specific to the upper ocean hydrography and vertical mixing processes north of Svalbard, and general conclusions cannot be drawn; nevertheless, the findings have implications for wintertime entrainment of temperature, salinity, and biogeochemical tracers from deeper water, and are relevant in the broader context of large-scale circulation and tracer studies.

Acknowledgments

The field work and A.M. have been supported by the Norwegian Polar Institute's Centre for Ice, Climate and Ecosystems (ICE) through the N-ICE project. A.K.P. is supported by the Research Council of Norway, through the project 229786. Additional support was obtained from the Centre for Climate Dynamics at the Bjerknes Centre through the BASIC project. A.R. was supported through CARBON BRIDGE (project 226415) funded by the Norwegian Research Council. We thank Miles McPhee for making the TIC instrumentation available, the ice physics group for making the ice core and EM data available, and the atmospheric forcing group for making the wind data available. We thank the captains, crews, and sciences parties for their help in making this study possible. Comments from two reviewers helped improve the manuscript substantially. Data used in this study are publicly available at the Norwegian Polar Data Centre: MSS data [*Meyer et al.*, 2016], TIC data [*Peterson et al.*, 2016], surface meteorology data [*Hudson et al.*, 2015], ice core data [*Gerland et al.*, 2017], and EM31 total (snow and ice) thickness data [*Rösel et al.*, 2016].

References

Amante, C., and B. W. Eakins (2009), ETOPO1 1 arc-minute global relief model: Procedures, data sources and analysis, *NOAA Tech. Memo. NESDIS NGDC-24*, Natl. Geophys. Data Cent., NOAA, USA, doi:10.7289/V5C8276M.

Carmack, E., et al. (2015), Towards quantifying the increasing role of oceanic heat in sea ice loss in the new Arctic, *Bull. Am. Meteorol. Soc.*, *96*, 2079–2105, doi:10.1175/BAMS-D-13-00177.1.

Cole, S. T., M.-L. Timmermans, J. M. Toole, R. A. Krishfield, and F. T. Thwaites (2014), Ekman veering, internal waves, and turbulence observed under Arctic Sea Ice, *J. Phys. Oceanogr.*, *44*, 1306–1328, doi:10.1175/JPO-D-12-0191.1.

D'Asaro, E. A., T. B. Sanford, P. P. Niiler, and E. J. Terrill (2007), Cold wake of Hurricane Frances, *Geophys. Res. Lett.*, *34*, L15609, doi:10.1029/2007GL030160.

Davis, P. E. D., C. Lique, H. L. Johnson, and J. D. Guthrie (2016), Competing effects of elevated vertical mixing and increased freshwater input on the stratification and sea ice cover in a changing Arctic Ocean, *J. Phys. Oceanogr.*, *46*, 1531–1553, doi:10.1175/Jpo-D-15-0174.1.

Dosser, H. V., and L. Rainville (2016), Dynamics of the changing near-inertial internal wave field in the Arctic Ocean, *J. Phys. Oceanogr.*, *46*, 395–415, doi:10.1175/jpo-d-15-0056.1.

Fer, I. (2006), Scaling turbulent dissipation in an Arctic fjord, *Deep Sea Res., Part II*, *53*, 77–95.

Fer, I. (2009), Weak vertical diffusion allows maintenance of cold halocline in the central Arctic, *Atmos. Oceanic Sci. Lett.*, *2*, 148–152.

Fer, I. (2014), Near-inertial mixing in the Central Arctic Ocean, *J. Phys. Oceanogr.*, *44*, 2031–2049, doi:10.1175/JPO-D-13-0133.1.

Fer, I., R. Skogseth, and F. Geyer (2010), Internal waves and mixing in the Marginal Ice Zone near the Yermak Plateau, *J. Phys. Oceanogr.*, *40*, 1613–1630.

Gerland, S., M. A. Granskog, J. King, and A. Rösel (2017), *N-ICE2015 Ice Core Physics: Temperature, Salinity and Density*, Norw. Polar Inst., Norway, doi:10.21334/npolar.2017.c3db82e3.

Granskog, M. A., P. Assmy, S. Gerland, G. Spreen, H. Steen, and L. H. Smedsrud (2016), Arctic research on thin ice: Consequences of Arctic sea ice loss, *Eos*, *97*, 22–26, doi:10.1029/2016EO044097.

Guthrie, J. D., I. Fer, and J. H. Morison (2015), Observational validation of the diffusive convection flux laws in the Amundsen Basin, Arctic Ocean, *J. Geophys. Res. Oceans*, *120*, 7880–7896, doi:10.1002/2015JC010884.

Hudson, S. R., L. Cohen, and V. P. Walden (2015), N-ICE2015 Surface Meteorology, Norw. Polar Inst., Norway, doi:10.21334/npolar.2015.056a61d1.

IOC, SCOR, IAPSO (2010), The international thermodynamic equation of seawater - 2010: Calculations and use of thermodynamic properties, in *Manuals and Guides No. 56*, Intergov. Oceanogr. Comm., UNESCO, France.

Ivanov, V., V. Alexeev, N. V. Koldunov, I. Repina, A. B. Sando, L. H. Smedsrud, and A. Smirnov (2016), Arctic Ocean heat impact on regional ice decay: A suggested positive feedback, *J. Phys. Oceanogr.*, *46*, 1437–1456, doi:10.1175/Jpo-D-15-0144.1.

Jackson, J. M., W. J. Williams, and E. C. Carmack (2012), Winter sea-ice melt in the Canada Basin, Arctic Ocean, *Geophys. Res. Lett.*, *39*, L03603, doi:10.1029/2011GL050219.

Koenig, Z., C. Provost, N. Vilacieros-Robineau, N. Sennéchael, and A. Meyer (2016), Winter ocean-ice interactions under thin sea ice observed by IAOOS platforms during N-ICE2015: Salty surface mixed layer and active basal melt, *J. Geophys. Res. Oceans*, *121*, 7898–7916, doi:10.1002/2016JC012195.

Krishfield, R. A., and D. K. Perovich (2005), Spatial and temporal variability of oceanic heat flux to the Arctic ice pack, *J. Geophys. Res.*, *110*, C07021, doi:10.1029/2004JC002293.

Lenn, Y. D., et al. (2009), Vertical mixing at intermediate depths in the Arctic boundary current, *Geophys. Res. Lett.*, *36*, L05601, doi:10.1029/2008GL036792.

Lueck, R. G., F. Wolk, and H. Yamazaki (2002), Oceanic velocity microstructure measurements in the 20th century, *J. Oceanogr.*, *58*, 153–174.

Maykut, G. A. (1982), Large-scale heat exchange and ice production in the central Arctic, *J. Geophys. Res.*, *87*(C10), 7971–7984, doi:10.1029/JC087iC10p07971.

Maykut, G. A., and M. G. McPhee (1995), Solar heating of the Arctic mixed layer, *J. Geophys. Res.*, *100*(C12), 24,691–24,703.

McPhee, M. G. (1992), Turbulent heat flux in the upper ocean under sea ice, *J. Geophys. Res.*, *97*(C4), 5365–5379.

McPhee, M. G. (1999), Parameterization of mixing in the ocean boundary layer, *J. Mar. Syst.*, *21*, 55–65.

McPhee, M. G. (2008), *Air-Ice-Ocean Interaction: Turbulent Ocean Boundary Layer Exchange Processes*, 215 pp., Springer, New York.

McPhee, M. G., G. A. Maykut, and J. H. Morison (1987), Dynamics and thermodynamics of the ice/upper ocean system in the marginal ice zone of the Greenland Sea, *J. Geophys. Res.*, *92*(C7), 7017–7031.

McPhee, M. G., J. H. Morison, and F. Nilsen (2008), Revisiting heat and salt exchange at the ice-ocean interface: Ocean flux and modeling considerations, *J. Geophys. Res.*, *113*, C06014, doi:10.1029/2007JC004383.

Meyer, A., et al. (2016), N-ICE2015 Ocean Microstructure Profiles (MSS90L), Norw. Polar Inst., Norway, doi:10.21334/npolar.2016.774bf6ab.

Meyer, A., et al. (2017), Winter to summer hydrographic and current observations in the Arctic Ocean north of Svalbard, *J. Geophys. Res. Oceans*, doi:10.1002/2016JC012391, in press.

Nishino, S., Y. Kawaguchi, J. Inoue, T. Hirawake, A. Fujiwara, R. Futsuki, J. Onodera, and M. Aoyama (2015), Nutrient supply and biological response to wind-induced mixing, inertial motion, internal waves, and currents in the northern Chukchi Sea, *J. Geophys. Res. Oceans*, *120*, 1975–1992, doi:10.1002/2014JC010407.

Osborn, T. R. (1980), Estimates of the local rate of vertical diffusion from dissipation measurements, *J. Phys. Oceanogr.*, *10*, 83–89.

Padman, L., and T. M. Dillon (1991), Turbulent mixing near the Yermak Plateau during the coordinated Eastern Arctic Experiment, *J. Geophys. Res.*, *96*(C3), 4769–4782.

Peralta-Ferriz, C., and R. A. Woodgate (2015), Seasonal and interannual variability of pan-Arctic surface mixed layer properties from 1979 to 2012 from hydrographic data, and the dominance of stratification for multiyear mixed layer depth shoaling, *Prog. Oceanogr.*, *134*, 19–53, doi:10.1016/j.pocean.2014.12.005.

Peterson, A. K., A. Randelhoff, I. Fer, A. Meyer, L. Håvik, L. H. Smedsrud, I. Onarheim, M. Muijlwick, A. Sundfjord, and M. G. McPhee (2016), N-ICE2015 Ocean Turbulent Fluxes From Under-Ice Turbulent Cluster, Norw. Polar Inst., Norway, doi:10.21334/npolar.2016.ab29f1e2.

Peterson, A. K., I. Fer, M. G. McPhee, and A. Randelhoff (2017), Turbulent heat and momentum fluxes in the upper ocean under Arctic Sea Ice, *J. Geophys. Res. Oceans*, doi:10.1002/2016JC012283, in press.

Polyakov, I. V., A. V. Pnyushkov, R. Rember, L. Padman, E. C. Carmack, and J. M. Jackson (2013), Winter convection transports atlantic water heat to the surface layer in the eastern Arctic Ocean, *J. Phys. Oceanogr.*, *43*, 2142–2155, doi:10.1175/JPO-D-12-0169.1.

Price, J. F., R. A. Weller, and R. Pinkel (1986), Diurnal cycling: Observations and models of the upper ocean response to diurnal heating, cooling, and wind mixing, *J. Geophys. Res.*, *91*(C7), 8411–8427.

Provost, C., N. Sennéchael, J. Miguet, P. Itkin, A. Rösel, Z. Koenig, N. Villacieros-Robineau, and M. A. Granskog (2017), Observations of flooding and snow-ice formation in a thinner Arctic sea ice regime during the N-ICE2015 campaign: Influence of basal ice melt and storms, *J. Geophys. Res. Oceans*, doi:10.1002/2016JC012011, in press.

Randelhoff, A., and J. D. Guthrie (2016), Regional patterns in current and future export production in the central Arctic Ocean quantified from nitrate fluxes, *Geophys. Res. Lett.*, *43*, 8600–8608, doi:10.1002/2016GL070252.

Randelhoff, A., A. Sundfjord, and M. Reigstad (2015), Seasonal variability and fluxes of nitrate in the surface waters over the Arctic shelf slope, *Geophys. Res. Lett.*, *42*, 3442–3449, doi:10.1002/2015GL063655.

Randelhoff, A., I. Fer, A. Sundfjord, J.-É. Tremblay, and M. Reigstad (2016), Vertical fluxes of nitrate in the seasonal nitracline of the Atlantic sector of the Arctic Ocean, *J. Geophys. Res. Oceans*, *121*, 5282–5295, doi:10.1002/2016JC011779.

Randelhoff, A., I. Fer, and A. Sundfjord (2017), Turbulent upper-ocean mixing affected by meltwater layers during Arctic summer, *J. Phys. Oceanogr.*, doi:10.1175/jpo-d-16-0200.1, in press.

Rudels, B. (2015), Arctic Ocean circulation, processes and water masses: A description of observations and ideas with focus on the period prior to the International Polar Year 2007-2009, *Prog. Oceanogr.*, *132*, 22–67, doi:10.1016/j.pocean.2013.11.006.

Rudels, B., L. G. Anderson, and E. P. Jones (1996), Formation and evolution of the surface mixed layer and halocline of the Arctic Ocean, *J. Geophys. Res.*, *101*(C4), 8807–8821.

Rudels, B., H. J. Friedrich, D. Hainbucher, and G. Lohmann (1999), On the parameterisation of oceanic sensible heat loss to the atmosphere and to ice in an ice-covered mixed layer in winter, *Deep Sea Res., Part II*, *46*, 1385–1425.

Rösel, A., et al. (2016), N-ICE2015 Total (Snow and Ice) Thickness Data From EM31, Norw. Polar Inst., Norway, doi:10.21334/npolar.2016.70352512.

Shaw, W. J., and T. P. Stanton (2014), Vertical diffusivity of the Western Arctic Ocean halocline, *J. Geophys. Res. Oceans*, *119*, 5017–5038, doi:10.1002/2013JC009598.

Shaw, W. J., T. P. Stanton, M. G. McPhee, J. H. Morison, and D. G. Martinson (2009), Role of the upper ocean in the energy budget of Arctic sea ice during SHEBA, *J. Geophys. Res.*, *114*, C06012, doi:10.1029/2008JC004991.

Sirevaag, A. (2009), Turbulent exchange coefficients for the ice/ocean interface in case of rapid melting, *Geophys. Res. Lett.*, *36*, L04606, doi:10.1029/2008GL036587.

Sirevaag, A., and I. Fer (2009), Early spring oceanic heat fluxes and mixing observed from drift stations north of Svalbard, *J. Phys. Oceanogr.*, *39*, 3049–3069.

Timmermans, M.-L., J. Toole, A. Proshutinsky, R. Krishfield, and A. Plueddemann (2008), Eddies in the Canada Basin, Arctic Ocean, observed from ice-tethered profilers, *J. Phys. Oceanogr.*, *38*, 133–145, doi:10.1175/2007jpo3782.1.

Toole, J. M., M. L. Timmermans, D. K. Perovich, R. A. Krishfield, A. Proshutinsky, and J. A. Richter-Menge (2010), Influences of the ocean surface mixed layer and thermohaline stratification on Arctic Sea ice in the central Canada Basin, *J. Geophys. Res.*, *115*, C10018, doi:10.1029/2009JC005660.

Paper III

4.3 Observations of brine plumes below Arctic sea ice

Algot K. Peterson

Ocean Science Discussions, (2017), doi:10.5194/os-2017-27.

III

Ocean Sci. Discuss., doi:10.5194/os-2017-27, 2017
Manuscript under review for journal Ocean Sci.
Discussion started: 8 May 2017

Ocean Science
Discussions
Open Access
EGU

Observations of brine plumes below Arctic sea ice

Algot K. Peterson[1,2]

[1]Geophysical Institute, University of Bergen, Norway
[2]Bjerknes Centre for Climate Research, Norway

Correspondence to: Algot K. Peterson (algot@uib.no)

Abstract. In sea ice, interconnected pockets and channels of brine are surrounded by fresh ice. Over time, brine is lost by gravity drainage and flushing. The timing of salt release and its interaction with the underlying water can impact subsequent sea ice melt. Turbulence measurements 1 m below melting sea ice north of Svalbard reveal anti-correlated heat and salt fluxes. From the observations, 131 salty plumes descending from the warm sea ice are identified, confirming previous observations from a Svalbard fjord. The plumes are likely triggered by oceanic heat through bottom melt. Calculated over a composite plume, oceanic heat- and salt fluxes during the plumes account for 6% and 9% of the total fluxes, respectively, while only lasting in total 0.5% of the time. The observed salt flux accumulates to 7.6 kg m^{-2}, indicating nearly full desalination of the ice. Bulk salinity reduction between two nearby ice cores agree with accumulated salt fluxes to within factor of two. The increasing fraction of younger, more saline ice in the Arctic suggests an increase in desalination processes with the transition to the 'new Arctic'.

1 Introduction

In the Arctic Ocean, sea ice is an effective barrier for exchange between the ocean and atmosphere. The presence of sea ice is, however, depending on a delicate balance between the atmospheric and oceanic heat fluxes. The inflowing Atlantic water contains enough heat to melt the Arctic sea ice in a few years (Turner, 2010), and a small change in oceanic heat flux can have huge implications for the heat balance at the interface. Understanding the processes that control vertical heat fluxes under the sea ice is important to understand the response of sea ice to a changing climate (Carmack et al., 2015). The interplay between heat and salt exchange at the ice-ocean interface can work to enhance or reduce sea ice melt in the Arctic Ocean (Sirevaag, 2009).

While sea ice in bulk is a source of fresh water to the upper ocean, the sea ice consists of fresh ice surrounding pockets of liquid brine, connected through a network of channels and capillaries (Petrich and Eicken, 2010). The brine remains at its salinity-determined freezing point, in thermal equilibrium with the surrounding ice, and brine salinity and volume adjusts to temperature changes by growing or melting fresh ice.

Over time, salt is lost from the sea ice. Timing of the salt release and how the salt is distributed in the water column is important in the evolution of the Arctic mixed layer. The main desalination processes of sea ice are gravity drainage and flushing of surface meltwater and melt ponds (Notz and Worster, 2009). While melt ponds are present only in advanced stages of melt, gravity drainage occurs throughout the seasons. Ice permeability is a controlling factor for gravity drainage, increasing

Ocean Sci. Discuss., doi:10.5194/os-2017-27, 2017
Manuscript under review for journal Ocean Sci.
Discussion started: 8 May 2017

with temperature as the ice warms (Golden et al., 1998). When sea ice warms to within a certain critical temperature range, full depth brine convection and desalination can occur, even before the onset of melt (Jardon et al., 2013). Furthermore, gravity drainage has been successfully modeled using a 1D sea ice model, and can be triggered both by atmospheric heat and bottom melt from oceanic heat (Griewank and Notz, 2013).

Despite theoretical understanding and successful modeling of spring-time brine convection, observations are sparse. Brine drainage in response to atmospheric warming may have been the cause of observed salinity anomalies below sea ice in Storfjorden (Jardon et al., 2013). Still, the main evidence so far has been observations of saline plumes descending from warming landfast sea ice in a Svalbard fjord (Widell et al., 2006). It has been hypothesized that this form of desalination can occur on drifting Arctic sea ice, but so far this has remained unverified. The existence of such plumes can be important to the desalination of sea ice, subsequent distribution of salinity in the upper water column, and could thus affect the otherwise strong surface stratification typical below melting ice.

The first observations of brine plumes released from drifting sea ice in the Arctic Ocean are presented here. The observations are collected in June 2015, in the MIZ north of Svalbard (Figure 1). The data is a subset of a previously reported under-ice turbulence data set (Peterson et al., 2017, 2016), and is part of the Norwegian Young Sea Ice Cruise (N-ICE2015, Granskog et al., 2016).

2 Data and methods

2.1 Turbulence instrument cluster

Under-ice turbulence measurements were made using a turbulence instrument cluster (TIC), deployed 1 m below the ice undersurface, relying on eddy-covariance to calculate turbulent fluxes of momentum and scalars from point measurements of temperature, salinity and currents. The cluster is fixed on a mast which is deployed through a hole in the sea ice, suspended on a wire which allows adjustment of the instrument depth. The concept is well-proven, and processing follows previous studies (McPhee, 2002; McPhee et al., 2008). Detailed description of the setup is given in Peterson et al. (2017), briefly summarized below. Horizontal and vertical currents are rotated into the mean current direction (u), such that cross-stream (v) and vertical (w) current averages zero for a given 15-minute segment. The data gaps visible in Figure 2 are due to two corrupt data files.

Heat flux is calculated from the covariance of temperature and vertical velocity,

$$F_H = \rho_w c_p \langle w'T' \rangle, \tag{1}$$

where ρ_w is the water density and c_p is the specific heat capacity of the water, angled brackets indicate a temporal mean, and primes indicate detrended values (fluctuations about a 15-minute mean value). The heat flux is positive when warmer water is brought upward, and cold downward. Similarly, salinity flux is calculated as

$$F_S = \langle w'S' \rangle, \tag{2}$$

Ocean Sci. Discuss., doi:10.5194/os-2017-27, 2017
Manuscript under review for journal Ocean Sci.
Discussion started: 8 May 2017

Ocean Science
Discussions
Open Access
EGU

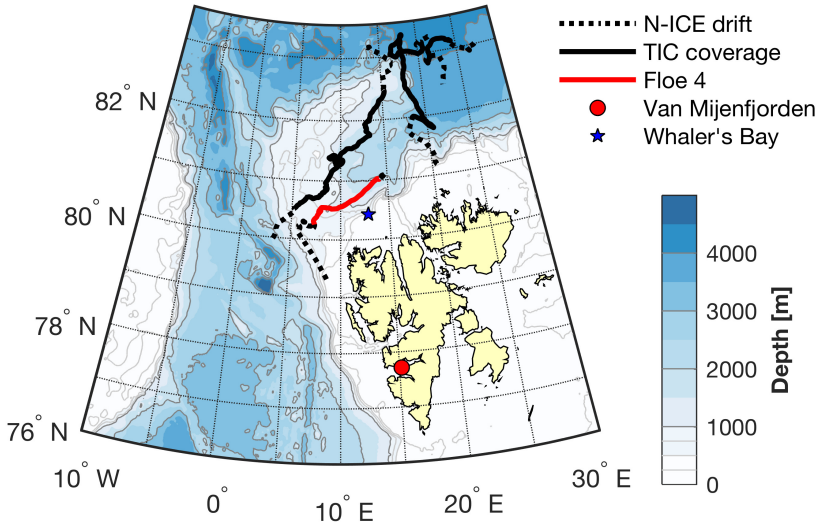

Figure 1. Overview of the study region north of Svalbard, showing the whole N-ICE2015 drift track, emphasizing parts covered by TIC measurements, and the Floe 4 subset (red), which is studied here. The positions of the Van Mijenfjorden study (Widell et al., 2006) and Whaler's Bay (Sirevaag, 2009) are shown for reference.

where F_S is positive when more saline water is brought upward, and fresher water moves down. Accumulated salt flux (units kg m^{-2}) is calculated by adding up 15-minute salt fluxes (m s^{-1}) multiplied by the segment's duration (s), using salinity in kg m^{-3}.

Covariance of horizontal to vertical velocity gives the components of Reynold's stress, presented here as friction velocity,

$$u_* = \sqrt{\tau} = \left[\langle u'w'\rangle^2 + \langle v'w'\rangle^2\right]^{1/4}, \quad (3)$$

where τ is the kinematic Reynolds stress magnitude.

The TIC data and the derived fluxes have been subjected to an extensive quality control, which is described in full in Peterson et al. (2017). The systematic approach is taken to ensure the validity of Taylor's hypothesis, which is crucial to the turbulent flux calculations. Each 15-min segment is split in 1-min half-overlapping subsegments, for which mean and root-mean-square values are calculated. This is compared to artificial Gaussian data, and is used to identify variability in the flow that may violates Taylor's hypothesis, such as trends, rapid change in current direction and swell. Segments that do not meet the criteria indicate unsteady flow, and are excluded from the analysis.

Ocean Sci. Discuss., doi:10.5194/os-2017-27, 2017
Manuscript under review for journal Ocean Sci.
Discussion started: 8 May 2017

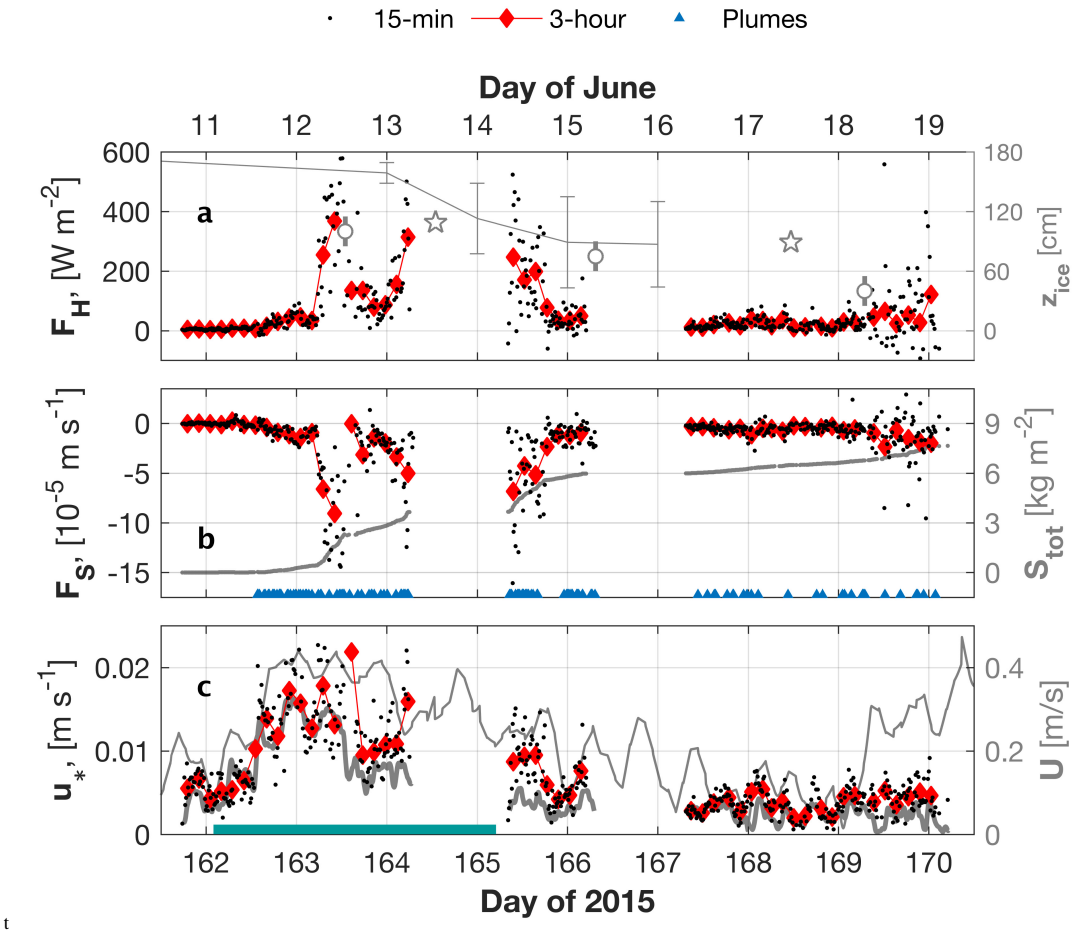

t

Figure 2. Turbulent fluxes of (a) heat and (b) salt, and (c) friction velocity are shown as 15-minute data points (dots) and 3-hour bin-averages (diamonds). In (a), sea ice thickness is shown from manual measurements in the TIC hole (circles), hot wires (line) and two ice cores (stars). (b) Identified plumes are indicated by blue triangles, and the cumulative salt flux, S_{tot} is given in kg m^{-2} (gray). The sea ice drift speed (thin) and along-stream current (TIC, thick) are shown in (c) (gray), and timing of a passing storm is indicated by the green line (defined by Cohen et al.)).

Ocean Sci. Discuss., doi:10.5194/os-2017-27, 2017
Manuscript under review for journal Ocean Sci.
Discussion started: 8 May 2017

2.2 Auxiliary data

The TIC data are supplemented by atmospheric data from a 10 m tall weather mast (Cohen et al.; Hudson et al., 2015), and navigational data from the research vessel Lance, which was anchored to the same ice floe during the drifts, approximately 300-400 m away.

Environmental data from the upper ocean is obtained from profiles of temperature and salinity made using a microstructure sonde (MSS, Meyer et al.). The profiles were typically collected in sets of three casts, repeated three times daily. Casts were made through a hydrohole about 50 m from the TIC site. Data was validated against the ship-borne CTD (conductivity, temperature, depth) and corrected for sensor drift. The data were analyzed using the Thermodynamic Equation of SeaWater 2010 (TEOS-10, McDougall and Barker, 2011) and Conservative Temperature (Θ) and Absolute Salinity (S_A) are used throughout.

Ice cores were sampled throughout the campaign, for different ice types and sampling variables (Granskog et al., 2017). Two co-located ice cores with both temperature and salinity measurements were collected on the same ice floe as the flux measurements, and are used in this study. Brine volume is calculated as $\Phi = S_{bu}/S_{br}$, where S_{bu} is the bulk salinity, and brine salinity is calculated using the linear relation $S_{br} = -T_{ice}/0.05411$, which is adequate for warm ice (Notz et al., 2005).

In addition to the total height of the two ice cores, sea ice thickness is measured manually in the TIC hydrohole, and in a grid of hot wires (Figure 2). The manual measurements were read from a ruler (pers. comm., Amelie Meyer, January 2017). Due to large, but unknown uncertainty, the measurements in Figure 2a are arbitrarily assigned $\pm$15 cm error bars. A set of four hot wires were set up in an area of deformed sea ice, initially nearly 2 m thick (Rösel et al., 2016). The error bars in Figure 2a is the standard deviation of the wires. Because of the spatial variability and uncertainties of the different measurements, all ice thickness should be interpreted with care.

3 Environmental setting

Observations were made from a drifting ice floe in the MIZ between June 10 to 19 (Figures 1 & 3). The drift took place over the Yermak Plateau, where a branch of the warm West Spitsbergen Current flows across the plateau (Meyer et al., 2017). Over 9 days, the floe drifted 185 km, with an average drift speed of 23 cm s^{-1}, while water depths shoaled from about 2000 m to less than 1000 m over the Yermak Plateau. The floe had an approximate diameter of 1200 m, and likely consisted of only first year ice (Granskog et al., 2017). The TIC mast was deployed approximately 250 m from the floe edge. The ice drift was mostly parallel to the ice edge (Figure 3).

Temperature at 1 m below the ice averaged to $\Delta T = 0.6°$C above freezing, lowest on June 11 ($\Delta T = 0.1°$C) and highest (1.6°C) during the storm on June 13. Atlantic water flows along the topographic slope (Meyer et al., 2017), and is often found at depths shallower than 30 m (defined as T$> 0°$C, Figure 3). Toward the end of the drift a warm intrusion is also observed at 5 to 10 m depth.

Stratification (Figure 3b) in the upper 35 m varies significantly over the drift in and out of warmer waters. The mixed layer depth gradually changes from quite deep (>30 m) in the beginning of the drift, to non-existing at the end, varying with drift to and from areas where warm Atlantic water flows closer to the surface. First, there is a transition from waters of weak

Ocean Sci. Discuss., doi:10.5194/os-2017-27, 2017
Manuscript under review for journal Ocean Sci.
Discussion started: 8 May 2017

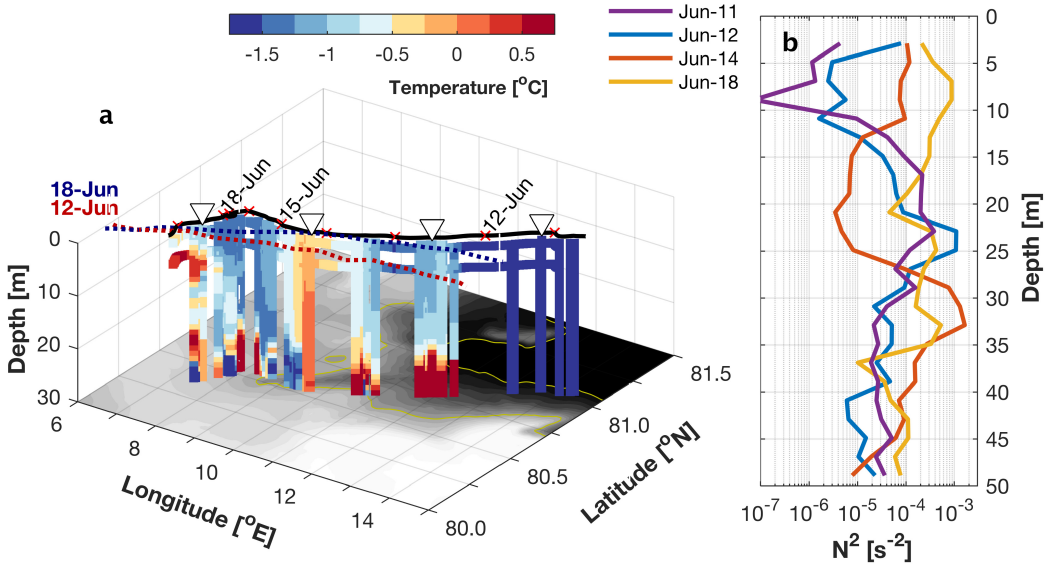

Figure 3. Ocean and sea ice conditions over the course of the drift. (a) Drift track between June 10 to June 19 (black) with daily ticks (crosses). Conservative Temperature in the top 30 m from MSS profiles (vertical) and TIC (horizontal) is shown in colors. The ice edge (50% concentration) is shown for June 12 and 18. Water depth is indicated in shading, with yellow isolines at 1000 m and 2000 m. Triangles mark the location of (b) four profiles of stratification (N^2) in the upper 50 m.

stratification (June 11) to gradually stronger surface stratification. On June 12, The top of the pycnocline is about 20 m, reaching 27 m on June 14. Towards the end of the drift, there is strong stratification continuously up to the surface, and there is no mixed layer present on June 18.

Although sea ice thickness measurements are coarse, significant melt is evident over the drift (Figure 2a). The measurements in the TIC hydrohole indicate a reduction from ∼100 cm to ∼40 cm between June 12 to 18. Less melt was seen from the ice cores, with a reduction from 109 cm to 89 cm between June 13 to 17. Hot wires measured a decrease from 174 cm to 87 cm over the measurements, although with a very large difference between sensors (variance of up to 46 cm). The ice around the hydrohole is likely melting faster compared to some distance away, and a representative sea ice reduction is likely somewhere between hydrohole and ice core values. Still, by the end of the measurements on June 19, the ice was only a few decimeters thick, and the floe was disintegrating.

Ocean Sci. Discuss., doi:10.5194/os-2017-27, 2017
Manuscript under review for journal Ocean Sci.
Discussion started: 8 May 2017

Ocean Science Discussions
Open Access
EGU

4 Results

Eddy co-variance measurements from 1 m below the ice under-surface reveal anti-correlated turbulent heat and salt fluxes (Figure 2, $r = -0.94$), at a time of rapid bottom melt. Oceanic heat fluxes are directed towards the ice, and reach several hundred W m^{-2} in response to a passing storm. Salt fluxes are directed down from the ice, exceeding -10^{-4} m s^{-1}. Downward flux of salt is typical of freezing conditions, such as that observed in refreezing leads in the pack ice north of Alaska (McPhee and Stanton, 1996). During melting conditions, heat and salt fluxes are more typically both positive, as fresh meltwater is fluxed downward, and is replaced by warmer water from below.

The observed heat- and salt fluxes result from relatively cool, saline water above warmer, fresher water, which is an inherently unstable configuration that cannot be sustained over time. Unstable conditions can occur during a frontal passage, where the observation point (ice floe) drifts from cool and saline water into an area of warmer, fresher water (McPhee et al., 1987; Sirevaag, 2009). When the floe drifts into recently ice-free waters, freshened from sea ice melt and warmed by the sun, cool water moving with the ice floe could be dragged over warm water, setting up an instability with appropriate gradients. The floe drifts over recently ice-free waters on two occasions, and for shorter periods such overturning might be expected, most notably in the last hours on June 12, concurrent with the decreasing flux magnitudes. However, the negative relationship between heat and salt fluxes is sustained over several days, during both increasing and decreasing temperatures, signaling a process which is continually feeding the instability. Negative correlation between the fluxes is consistent throughout the measurements. The turbulent heat flux is a likely forcing agent, as both fluxes increase with drift speed (Figure 2c) and upper ocean temperature (Figure 3a).

Brine released from warm sea ice is a possible explanation, consistent with negative salt flux and positive heat flux. Resemblance to the observations in the fjord study by Widell et al. (2006) inspired the search for an inferred, mean plume structure. Events are identified in a similar manner, requiring at least five consecutive points where $w' < 0$, $S' > 1 \times 10^{-5}$ and the salt flux magnitude, $|w'S'|$, exceeds 10^{-4} m s^{-1} or at least five times the root mean square value over the 15-minute segment. A 60 second window centered on the peak $w'S'$ value is used to construct a mean plume ensemble. For each iteration, the 15-minute window is moved 5 minutes in order to also detect plumes otherwise falling on the edge of a window. Duplicate events are removed, leaving 131 identified plumes for the ensemble average, shown in Figure 4. Averaging is done using a bootstrap calculation (Emery and Thomson, 2001), which resamples the data 1000 times to obtain an estimate of the average value occurring by chance. The mean plume and its 95% confidence interval from bootstrap calculations are shown in Figure 4. The shading represents percentiles of the data as a display of the variability between plumes.

The inferred plume is approximately symmetric in time about its peak. Anomalies in temperature and salinity gradually increase toward their peak values over about 10-15 s before they decrease again at the same pace. Vertical velocity perturbations, and thus also the fluxes, increase more abruptly, reaching a peak of 2-6 cm s^{-1} in about 7 s, before returning to near-zero. Horizontal velocity typically retards by around 5 cm s^{-1} during the plumes. Temperature and salinity anomalies deviate somewhat from symmetry, averaging positive (2.1×10^{-3} °C and 4.0×10^{-3}) before the plume, approaching zero after. There is, however, considerable variation between individual events, and these are just characteristics of the mean structure. Individual

Ocean Sci. Discuss., doi:10.5194/os-2017-27, 2017
Manuscript under review for journal Ocean Sci.
Discussion started: 8 May 2017

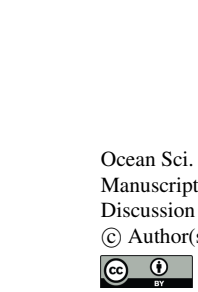

Ocean Science
Discussions
Open Access
EGU

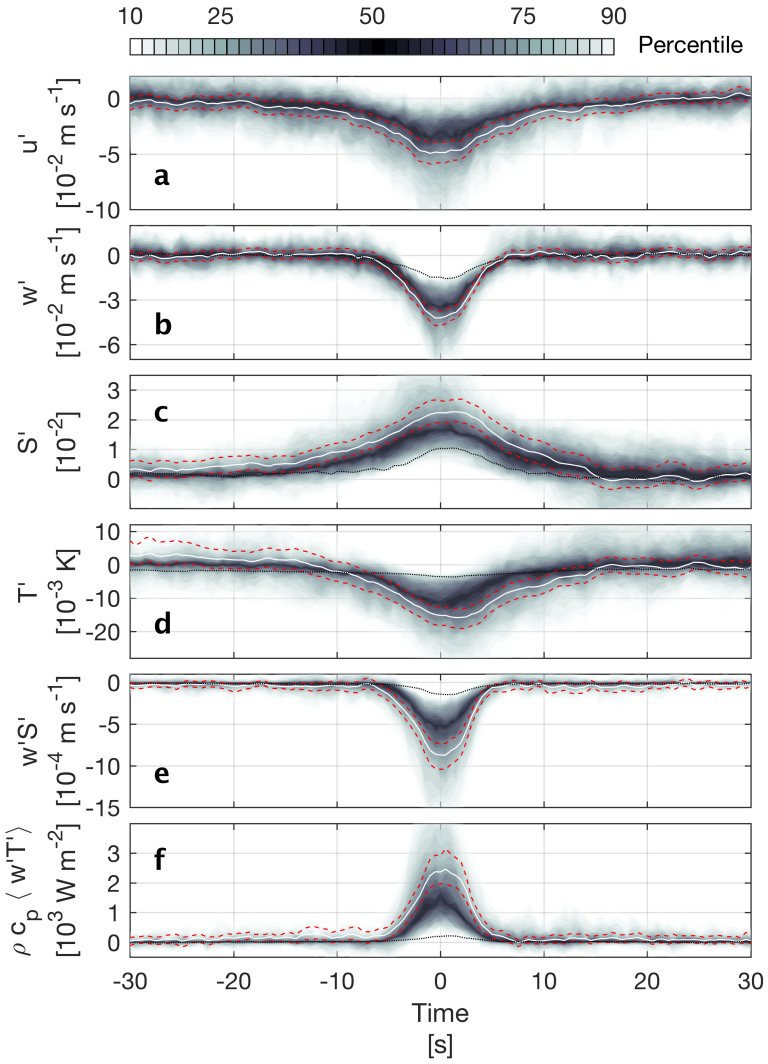

Figure 4. Composite of 131 plumes, identified using the peak in $\langle w'S' \rangle$, presented in a 60 second window. Spread in the data is shown as percentiles (shading), overlain by the mean (white) and its 95% confidence interval from bootstrap calculations (dashed red). Variables are fluctuations of (a) horizontal and (b) vertical velocity, (c) salinity (d) temperature, and turbulent fluxes of (e) salt and (f) heat. The results from Widell et al. (2006) are shown for reference (black dotted lines).

Ocean Sci. Discuss., doi:10.5194/os-2017-27, 2017
Manuscript under review for journal Ocean Sci.
Discussion started: 8 May 2017

Ocean Science Discussions
Open Access
EGU

Location/study	Statistic	w' [cm s^{-1}]	S' [10^{-3}]	T' [mK]	F_S [10^{-4} ms^{-1}]	F_H [W m^{-2}]
Open leads (McPhee and Stanton, 1996)	1-h mean				-0.15	5.9
Van Mijenfjorden (Widell et al., 2006)	Plume peak	-1.6	10	-3.7	-1.5	215
Whaler's Bay (Sirevaag, 2009)	Mean				0.19	268
	Overall mean				-0.19	75
Yermak Plateau	Plume mean	-2.0	18	-11	-3.7	1058
	Plume peak	-4.2	23	-15.8	-8.7	2465

Table 1. Statistics of fluctuations and turbulent fluxes in the present study over the Yermak Plateau in comparison with other Arctic studies of turbulent heat and salt fluxes.

plumes typically have sharper interfaces, and the smooth transitions in Figure 4 is partly due to averaging. Salt- and heat fluxes averaged over the 14 s surrounding the inferred plume peak are $F_S = -3.7 \times 10^{-4}$ m s^{-1} and $F_H = 1058$ W m^{-2}, respectively. The values observed here are up to one order of magnitude greater than those found by Widell et al. (2006) (See Table 1).

The impact of drift velocity on the plume observations is investigated in Figure 5. Drift speed does not relate linearly with the maximal heat flux in the plumes. In fact many of the most intense plumes observed (highest F_H) are during weak or moderate current speed. The peak in vertical velocity does, not surprisingly, increase with increasing current speed (Figure 5b). Drift speed also relates to the deviation in temperature from freezing, $\Delta T = T - T_f$, calculated from mean S_A and Φ over the 14 s surrounding the peak in vertical velocity. For low drift speed, many of the plume observations actually carry supercooled water. Supercooling decreases with drift speed, and is not observed for plumes where the mean current exceeds $\sim$25 cm s^{-1}. Plumes associated with high maximum heat fluxes are more often supercooled than not.

From an ice coring site located approximately 100 m from the measurement site (Granskog et al., 2016), but on the same ice floe, two ice cores sampled on June 13 and 17 give some insight (Figure 6). The ice core on June 13 shows 109 cm thick ice, with a 30 cm snow layer on top. The ice is rather warm, with a minimum temperature of -2.5°C in the interior of the ice, increasing towards the surface (-1.3°C) and the ice-ocean interface (-1.7°C). The 'C'-shaped temperature profile is indicative of a gradual warming from above. This is confirmed by atmospheric measurements, reporting temperate conditions throughout the measurements on the floe, with temperatures ranging from -2 to +2°C at 10 m height between June 7 to 20 (Cohen et al.). The snow layer was thick ($\sim$30 cm), slowing heat exchange with the ice (Granskog et al., 2017).

Comparison of the two ice cores reveals a decrease in bulk salinity from 6.4 to 4.8 in four days, but also a decrease in thickness of 20 cm, together causing a change in salt content of 2.8 kg m^{-2} (calculated by multiplying bulk salinity with ice thickness). The accumulated salt release during the flux observations was 7.6 kg m^{-2}, summed over available measurements between June 11 to 19 (Figure 2b). This is equivalent to a salinity decrease of 5 for 1.5 m thick ice. The salt flux observed here is approximately equivalent to the total salt content of the June 13 ice core. About half of the salt flux was observed before the ice core was sampled, so desalination had already taken place before coring. The salt flux observed after the time of coring

Ocean Sci. Discuss., doi:10.5194/os-2017-27, 2017
Manuscript under review for journal Ocean Sci.
Discussion started: 8 May 2017

Ocean Science
Discussions
Open Access
EGU

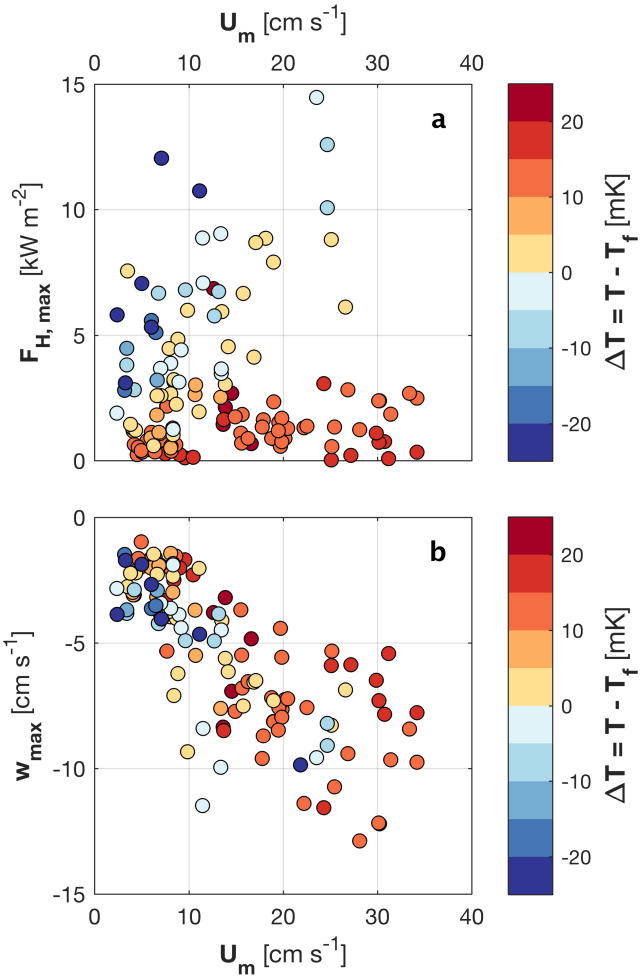

Figure 5. Mean horizontal current (U_m) vs. instantaneous (a) maximum heat flux and (b) minimum vertical current speed. Circles are color coded for temperature above freezing ($\Delta T = T - T_f$), calculated using mean Absolute Salinity and Conservative Temperature (McDougall and Barker, 2011). Mean values are calculated over the 14 s surrounding the peak vertical current speed of each identified plume.

Ocean Sci. Discuss., doi:10.5194/os-2017-27, 2017
Manuscript under review for journal Ocean Sci.
Discussion started: 8 May 2017

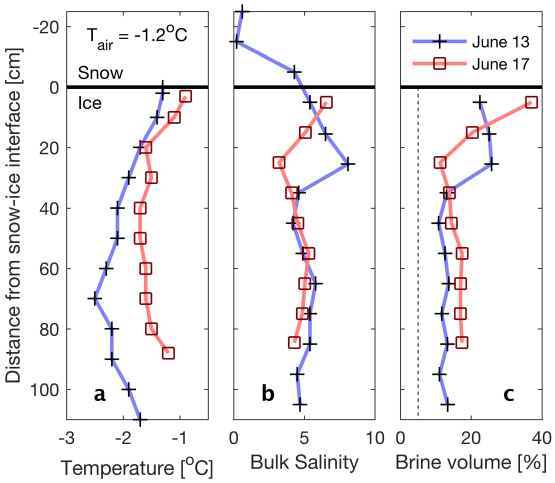

Figure 6. Vertical profiles of sea ice (a) temperature, (b) bulk salinity and (c) brine volume fraction. The ice cores are sampled about 100 m from the measurement site on June 13 and 17. Average temperatures are -1.9°C and -1.4°C, and bulk salinities are 6.4 and 4.8 for June 13 and 17, respectively. The typical 5% threshold required for gravity drainage (Cox and Weeks, 1975) is indicated (c, dotted line).

accounts for 57% of the total salt content of the ice core on June 13. The salt flux measured between the time of the two cores is 2.8 kg m^{-2}, the same amount as the change in salt content of the two ice cores. However, gaps in the time-series point to a discrepancy between ice cores and observed salt flux. Assuming the salt flux during the measurement gaps equal to the mean of available measurements, the accumulated salt flux between the two ice cores is approximately twice the observed reduction in the ice cores. The discrepancy might be linked to spatial inhomogeneity in ice composition and melt rates, variability between individual ice cores, or errors in the flux measurements (Section 6). Agreement between measured fluxes and salinity in ice cores within a factor of two supports that the salt flux can originate in brine release from the sea ice.

Calculated over the 14 s surrounding the peak salinity flux in the mean plume structure, the 131 identified events account for 0.7 m s^{-1}, or 9% of the observed total salt release, within a duration of 31 minutes (0.5% of the time), illustrating the intensity of the events. The heat flux averaged over the composite plume is 1058 W m^{-2}, and the plumes account for 6% (4.7 W m^{-2}) of the average observed heat flux between noon June 11 until the end of measurements on June 19. However, the plumes can additionally cause mixing of the surface layers, which could counteract stabilizing effects of bottom melt. The overall effect of the plumes on heat fluxes is thus difficult to quantify. Upper ocean hydrography profiles (Figure 3, Meyer et al., 2016) do not provide conclusive evidence, as advection and mixed layer deepening from wind forcing obscures any effect from the plumes.

Percolation or flushing of melt ponds could influence the measurements. Although the first melt pond was noted on June 9, they remained at a very early stage throughout the measurement period reported here. The pond fraction reached an estimated

Ocean Sci. Discuss., doi:10.5194/os-2017-27, 2017
Manuscript under review for journal Ocean Sci.
Discussion started: 8 May 2017

10% coverage. Mostly, ponds had formed at deformation areas where freeboard was negative, and were thus flooded with sea water rather than actual melt ponds (pers. comm., A. Rösel, January 14, 2017). Salinity measurements from three melt ponds revealed an Absolute Salinity of 20-29 g kg^{-1} (Shestov, 2017). The ice core from June 13 (Figure 6) had a 2 cm negative freeboard, and the deepest snow layer had a salinity of 4.3. Based on this, and noting the high permeability of the ice (high liquid fraction, Figure 6c), percolation may have played a role in the desalination process, but is not pursued further here.

The combined heat flux from above and below finally melted the sea ice. Substantial melt is also evident from the different ice thickness measurements (Figure 2a). At the end of the flux measurements there were only a few decimeters of ice left, and the floe disintegrated as the instruments were recovered on June 19. Over the course of the measurements, bottom melt caused an overall reduction in salinity measured at 1 m by approximately 1.

5 Discussion

The observations of saline plumes presented here extend the findings of Widell et al. (2006), and are the first observations of such plumes from drifting Arctic sea ice. While the structure is similar to the observations from Van Mijenfjorden (Widell et al., 2006), which were made with the same instrumentation on landfast ice, the magnitudes observed here are much greater, with peak values of salt and heat fluxes in the average plume of $F_S = -8.7 \times 10^{-4}$ m s^{-1} and $F_H = 2465$ W m^{-2} (See Table 1). While the measurements by Widell et al. (2006) were made during little (or no) ice melt, the present observations were made under during severe melting, which may be the primary difference between the two studies. The fjord study concluded that oceanic heat from the tidal inflow likely triggered brine release from the temperate ice (Widell et al., 2006).

During melting conditions, desalination can happen by gravity drainage or flushing (Notz and Worster, 2009). Flushing can occur when there is an overhead pressure from meltwater at the surface. The negative freeboard in the ice core and saline melt ponds indicate that there was in fact overhead seawater at the surface, which may have caused, or at least increased, desalination.

Gravity drainage occurs when the buoyancy of the brine exceeds the dissipative effects of thermal diffusion and viscosity within the sea ice. Atmospheric cooling in winter causes higher brine salinity, and thus density, in the upper part of the ice column. This makes the brine unstable, and convection within the ice takes place when the ice is sufficiently permeable (Notz and Worster, 2009). As the ice warms in spring, permeability increases as illustrated in Figure 7. The brine fraction in the ice cores exceeds 10% throughout the ice (Figure 6c), both well above the typical 5% threshold required for gravity drainage (Cox and Weeks, 1975). The instability needed for full-depth brine convection in the ice can be triggered either by atmospheric or oceanic heat, or a combination of the two (Griewank and Notz, 2013). The temperature at the ice-ocean interface is always at its salinity-determined freezing point, and warming from below can only be caused by freshening at the interface by ice melt.

Ice melts at the ocean interface when the heat supplied by the ocean exceeds the conductive heat flux in the ice. The high oceanic heat fluxes are caused by a combination of the passing storm, presence of warm Atlantic water near the surface and the high mobility of the sea ice driving mixing (Peterson et al., 2017; Meyer et al., 2017), and accounts for much of the observed melt. As the interface freshens, the interface's salinity-determined temperature $T_f(S)$ increases (Figure 7). T_f remains high as

Ocean Sci. Discuss., doi:10.5194/os-2017-27, 2017
Manuscript under review for journal Ocean Sci.
Discussion started: 8 May 2017

long as the fresh water is allowed to remain at the interface, or enough new melt water is supplied. Additionally, fresh water supplied by melting at the ice-ocean boundary increases the density deficit between the lower part of the ice and of the brine, which may increase the potential for gravity drainage.

The various ice thickness data (Figure 2a) show that significant melt was indeed occurring, up to as much as 25 cm day^{-1} during the observation period. Furthermore, the present observations show positive temperature anomalies prior to the plume events (Figure 4c). The positive temperature anomaly before the plumes, the sustained positive heat fluxes (Figure 2a) and rapid melt suggest that oceanic heat plays a key role through ice melt, required for triggering repeated convection events.

The difference in salt content between the two ice cores is mostly ($\sim$75%) due to reduction in ice thickness. The rapid ice melt is thus cause of most of the salt release, and likely the reason for the large difference between values observed here and those of Widell et al. (2006), where little or no ice melt took place. In addition to gravity drainage or flushing of brine, the brine pockets become directly exposed as melt progresses, and sink past the measurement volume. Considering most of the ice volume is lost during the measurements, is is not surprising if most of the original brine content in the ice is lost. It is, however, surprising that measurements at 1 m below the ice are of the same order of magnitude as the total desalination, which calls for an investigation of possible measurement errors or biases (Section 6).

Since the salt flux observed within the 131 identified plumes only account for 9% of the total salt flux, most of the salt flux takes place outside these plumes. Many more plumes are likely present nearby, but do not reach, or cross, the measurement volume. Such plumes would bring higher salinity water somewhere above the TIC, rather than being immediately mixed in with the fresh water at the ice-ocean interface. Subsequent mixing would be observed as a negative salt flux, although not identified as a plume. This may be the reason why salt fluxes are consistently negative, event though direct plume observations are more sporadic.

Brine released from sea ice would initially be at its salinity-determined freezing point, in balance with the surrounding ice. As the brine descends from the ice, it may thus be supercooled relative to its surroundings. When the horizontal velocity (and u_*) is greater, shear mixes and dilutes the released salt plumes more than during calm conditions. This is consistent with the observation of less supercooling with higher mean current, as seen in Figure 5. This also adds up with higher vertical velocity coinciding with higher horizontal velocity, as a large vertical velocity perturbation is typically manifest of strong turbulent mixing.

6 Error sources and biases

Salinity is calculated from a SeaBird Electronics SBE4 conductivity cell. The dependence of salinity on both conductivity and temperature can introduce spurious salt fluxes because of difference in response time between the temperature sensor and the conductivity cell. The standard SBE4 was chosen for flux calculations rather than the SBE7 micro-conductivity sensor, because the SBE7 reported suspicious values for part of the record. McPhee and Stanton (1996) made a comparison of a ducted conductivity cell (SBE4) with a fast-response micro-conductivity sensor (SBE7), and showed that most of the covariance occurred at lower frequencies. About 75% of the salinity flux was resolved by the SBE4. The present observations are obtained

Ocean Sci. Discuss., doi:10.5194/os-2017-27, 2017
Manuscript under review for journal Ocean Sci.
Discussion started: 8 May 2017

Ocean Science
Discussions
Open Access
EGU

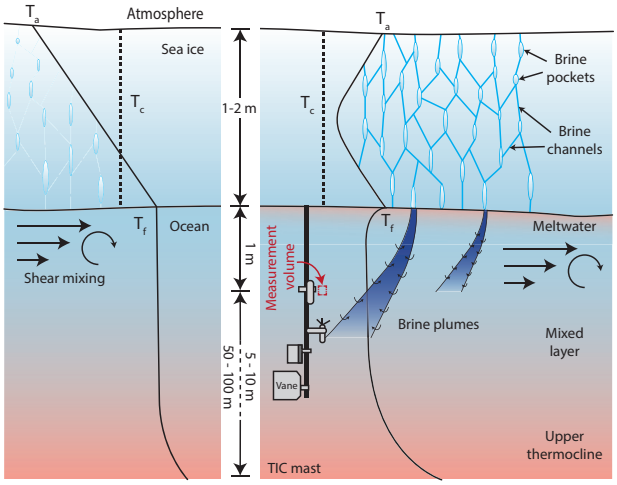

Figure 7. To the left is an early spring situation where the upper ocean is near freezing, and temperature in the ice is still below the critical temperature T_c, which must be exceeded for gravity drainage to occur. When the atmosphere warms the ice, permeability of the sea ice increases, and gravity drainage can occur. The brine plumes are triggered by meltwater below the ice, by directly exposing brine pockets, or by elevating the freezing point temperature T_f at the interface. The TIC mast is shown for reference, with measurement volume at 1 m below the ice.

during moderate to strong forcing (5-35 cm s^{-1} drift speed), which improves response time of the conductivity cell. It is advisable to interpret the observed fluxes with this uncertainty in mind, but note that the fluxes from the ducted conductivity are more likely an underestimate than an overestimate.

Considering the possibility of a baroclinic signal from the edge of the ice floe contaminating the measurements, the vertical modal structure is calculated from the profiles of buoyancy frequency shown in Figure 3b. The phase velocity of the first baroclinic vertical mode is 0.25-0.43 m s^{-1} for the four profiles. Taking the closest distance to the floe edge of ∼200 m, this implies a time scale for a signal originating at the floe edge of around 10 min. This is comparable to the segment length used for flux calculations (15 min), which could violate the validity of Taylor's hypothesis here. However, the systematic quality control described in Section 2 was designed to identify any violation of Taylor's hypothesis, and would thus have been excluded from the analysis.

Increased buoyancy frequency during the summer drift could affect the flux measurements. While the typical buoyancy period was about 1 h for the most of the drift (January through May), periods around 10 min and less were seen in June. Oscillations with periods on the order of the 15 min segment length could affect turbulent fluxes. However, recalculating the data set using 5 min segments revealed no significant differences, and Peterson et al. (2017) concluded that the systematic quality control had already flagged any contaminated segments.

Ocean Sci. Discuss., doi:10.5194/os-2017-27, 2017
Manuscript under review for journal Ocean Sci.
Discussion started: 8 May 2017

The hydrohole, through which the turbulence mast is deployed, can be suspected to affect measurements, and lateral heating may have caused faster melt in some radius around the hole. Still, the horizontal component of the flow is larger than the vertical, and observations made at the TIC represent conditions at the ice interface some distance away. Taking a vertical velocity anomaly of 2-5 cm s^{-1}, and the mean horizontal component of $\Delta U \sim$10 cm s^{-1} (difference between drift velocity and current measured at 1 m, Figure 2), a plume signal moves some 2-5 m in the horizontal over the 1 m vertical distance from the ice-ocean interface. The swiftest vertical speeds are also typically associated with large horizontal speed (Figure 5). This indicates that even for the large vertical speed seen in the plumes, influence from processes around the hydrohole is typically not expected.

The exact distance between the TIC measurement volume and the ice undersurface may be important for the absolute values observed, as one would expect plumes to gradually dissolve with distance from the ice. The manual measurements of ice thickness are accompanied by adjustments of the instrument depth. After each ice thickness measurement, the instrument was elevated to account for the ice melt. Interpreted from notes of these adjustments, the measurement volume was always at the correct depth within the range of the measurement uncertainty. In Figure 2a, the uncertainty is arbitrarily set to ± 15 cm.

Overall, salinity decreases by about 1 over the course of the drift, as measured by the instrument at 1 m. At the same time, the accumulated salt flux accounts for an increase in salinity of 1.7, if distributed over the 4.7 m average mixed layer depth (Meyer et al., 2017). The apparent inconsistency is caused by the separation in time-scales. Over longer time-scales, freshwater from ice melt is fluxed downwards, but is not apparent in the turbulence record because each 15-minute segment is detrended before fluxes are calculated. The comparison between accumulated salt flux and the salt contents of the ice core indicates that most of the brine in the ice convects down past the surface layer, rather than blending in with the fresh meltwater at the interface. Thus, it appears brine plumes as observed here affect the timing of the salt release, alter how the salt from sea ice is distributed in the water column, and can be an important factor influencing mixing during sea ice melt.

7 Concluding Remarks

Desalination of sea ice similar to that observed here likely occurs in the MIZ in spring in general, where enough heat is present to trigger such events. The present desalination appears to be forced by a combination of flushing, gravity drainage and direct release of salt through rapid melt caused by oceanic heat flux. In the interior Arctic Ocean, triggering by ocean heat flux is less likely, and brine release in the quantities reported here are more likely a MIZ phenomenon. With the transition towards a more seasonal ice cover in the Arctic, the fraction of first year ice is increasing (Meier et al., 2014). First year ice is more saline (Petrich and Eicken, 2010), with an equivalently greater potential for brine drainage. While this could indicate that saline first year ice can melt faster than fresher multi-year ice, in otherwise similar conditions, the transition to more FYI comes with increased fresh water run-off and increased upper ocean stratification (Nummelin et al., 2016). Desalination appears as a significant process in sea ice melt, although small in comparison to frontal processes and solar heating. Understanding desalination processes may still be increasingly more important in the ”new Arctic”, and requires more targeted field campaigns.

Ocean Sci. Discuss., doi:10.5194/os-2017-27, 2017
Manuscript under review for journal Ocean Sci.
Discussion started: 8 May 2017

Data availability. The following data sets are used in this study and are publicly available at the Norwegian Polar Data Centre: Turbulence instrument cluster data (Peterson et al., 2016), microstructure sonde (MSS) profiles (Meyer et al., 2016), meteorological data (Hudson et al., 2015), ice thickness from hot wires (Rösel et al., 2016) and ice core data (Gerland et al., 2017).

Competing interests. The author declares no competing interests.

Acknowledgements. The field work has been supported by the Norwegian Polar Institute's Centre for Ice, Climate and Ecosystems (ICE) through the N-ICE project. The author would like to thank everyone involved in the field work, and Amelie Meyer in particular, for keeping the instruments going until the very end. Thanks to Ilker Fer, Dirk Notz, Martin Vancoppenolle and Mats Granskog for useful discussions and input, and to Miles McPhee for making the instrumentation available. The author is supported by the Research Council of Norway, through the project 229786, with additional support from the Centre for Climate Dynamics at the Bjerknes Centre through the grant BASIC: Boundary Layers in the Arctic Atmosphere, Seas and Ice Dynamics.

Ocean Sci. Discuss., doi:10.5194/os-2017-27, 2017
Manuscript under review for journal Ocean Sci.
Discussion started: 8 May 2017

References

Carmack, E. C., Polyakov, I. V., Padman, L., Fer, I., Hunke, E., Hutchings, J. K., Jackson, J., Kelley, D. E., Kwok, R., Layton, C., Melling, H., Perovich, D. K., Persson, O., Ruddick, B., Timmermans, M.-L. L., Toole, J. M., Ross, T., Vavrus, S., and Winsor, P.: Toward quantifying the increasing role of oceanic heat in sea ice loss in the new Arctic, Bulletin of the American Meteorological Society, 96, 2079–2105, doi:10.1175/BAMS-D-13-00177.1, 2015.

Cohen, L., Hudson, S. R., Walden, and Granskog, M. A.: Meteorological conditions in a thinner Arctic sea ice regime from winter through summer during the Norwegian young sea ICE expedition (N-ICE2015), Journal of Geophysical Research, p. submitted.

Cox, G. F. N. and Weeks, W. F.: Brine Drainage and Initial Salt Entrapment in Sodium Chloride Ice, CRREL Research Report, p. 85, http://acwc.sdp.sirsi.net/client/search/asset/1015040, 1975.

Emery, W. J. and Thomson, R. E.: Data Analysis Methods in Physical Oceanography, Elsevier, 2 edn., 2001.

Gerland, S., Granskog, M. A., King, J., and Rösel, A.: N-ICE2015 ice core physics: temperature, salinity and density [Data set], doi:10.21334/npolar.2017.c3db82e3, 2017.

Golden, K. M., Ackley, S. F., and Lytle, V. I.: The percolation phase transition in sea Ice, Science, 282, 2238–2241, doi:10.1126/science.282.5397.2238, 1998.

Granskog, M. A., Assmy, P., Gerland, S., Spreen, G., Steen, H., and Smedsrud, L. H.: Arctic Research on Thin Ice: Consequences of Arctic Sea Ice Loss, Eos, 97, doi:10.1029/2016EO044097, 2016.

Granskog, M. A., Rösel, A., Dodd, P. A., Divine, D. V., Gerland, S., Martama, T., Leng, M. J., Martma, T., and Leng, M. J.: Snow contribution to first-year and second-year Arctic sea ice mass balance north of Svalbard, Journal of Geophysical Research - Oceans, pp. 2017–2033, doi:10.1002/2016JC012398, 2017.

Griewank, P. J. and Notz, D.: Insights into brine dynamics and sea ice desalination from a 1-D model study of gravity drainage, Journal of Geophysical Research: Oceans, 118, 3370–3386, doi:10.1002/jgrc.20247, 2013.

Hudson, S. R., Cohen, L., and Walden, V.: N-ICE2015 surface meteorology, doi:10.21334/npolar.2015.056a61d1, 2015.

Jardon, F. P., Vivier, F., Vancoppenolle, M., Lourenço, A., Bouruet-Aubertot, P., and Cuypers, Y.: Full-depth desalination of warm sea ice, Journal of Geophysical Research: Oceans, 118, 435–447, doi:10.1029/2012JC007962, 2013.

McDougall, T. J. and Barker, P. M.: Getting started with TEOS-10 and the Gibbs Seawater (GSW) Oceanographic Toolbox, 2011.

McPhee, M. G.: Turbulent stress at the ice/ocean interface and bottom surface hydraulic roughness during the SHEBA drift, Journal of Geophysical Research, 107, 8037, doi:10.1029/2000JC000633, 2002.

McPhee, M. G. and Stanton, T. P.: Internal waves and velocity fine structure in the Arctic Ocean, Journal of Geophysical Research, 101, 6409–6428, doi:10.1029/91JC01071, 1996.

McPhee, M. G., Maykut, G. A., and Morison, J. H.: Dynamics and thermodynamics of the ice/upper ocean system in the marginal ice zone of the Greenland Sea, Journal of Geophysical Research, 92, 7017, doi:10.1029/JC092iC07p07017, 1987.

McPhee, M. G., Morison, J. H., and Nilsen, F.: Revisiting heat and salt exchange at the ice-ocean interface: Ocean flux and modeling considerations, Journal of Geophysical Research, 113, C06 014, doi:10.1029/2007JC004383, 2008.

Meier, W. N., Hovelsrud, G. K., van Oort, B. E., Key, J. R., Kovacs, K. M., Michel, C., Haas, C., Granskog, M. A., Gerland, S., Perovich, D. K., Makshtas, A., and Reist, J. D.: Arctic sea ice in transformation: A review of recent observed changes and impacts on biology and human activity, Reviews of Geophysics, 52, 185–217, doi:10.1002/2013RG000431, 2014.

Meyer, A., Fer, I., Sundfjord, A., and Peterson, A. K.: Mixing rates and vertical heat fluxes north of Svalbard from Arctic winter to spring, Journal of Geophysical Research, p. in press, doi:10.1002/2016JC012441.

Meyer, A., Fer, I., Sundfjord, A., Peterson, A. K., Smedsrud, L. H., Muijlwick, M., Randelhoff, A., Håvik, L., Koenig, Z., Onarheim, I., Davies, P., Miguet, J., and Kusse-Tiuz, N.: N-ICE2015 ocean microstructure profiles (MSS90L) [Data set], doi:10.21334/npolar.2016.774bf6ab, 2016.

Meyer, A., Sundfjord, A., Fer, I., Provost, C., Villacieros Robineau, N., Koenig, Z., Onarheim, I. H., Smedsrud, L. H., Duarte, P., Dodd, P. A., Graham, R. M., Schmidtko, S., and Kauko, H. M.: Winter to summer oceanographic observations in the Arctic Ocean north of Svalbard, Journal of Geophysical Research: Oceans, p. in press, doi:10.1002/2016JC012391, 2017.

Notz, D. and Worster, M. G.: Desalination processes of sea ice revisited, Journal of Geophysical Research: Oceans, 114, 1–10, doi:10.1029/2008JC004885, 2009.

Notz, D., Wettlaufer, J. S., and Worster, M. G.: A non-destructive method for measuring the salinity and solid fraction of growing sea ice in situ, Journal of Glaciology, 51, 159–166, doi:10.3189/172756505781829548, 2005.

Nummelin, A., Ilicak, M., Li, C., and Smedsrud, L. H.: Consequences of future increased Arctic runoff on Arctic Ocean stratification, circulation, and sea ice cover, Journal of Geophysical Research: Oceans, 121, 617–637, doi:10.1002/2015JC011156, 2016.

Peterson, A. K., Fer, I., Randelhoff, A., Meyer, A., Håvik, L., Smedsrud, L. H., Onarheim, I., Muijlwick, M., Sundfjord, A., and McPhee, M. G.: N-ICE2015 ocean turbulent fluxes from under-ice turbulent cluster [Data set], doi:10.21334/npolar.2016.ab29f1e2, 2016.

Peterson, A. K., Fer, I., McPhee, M. G., and Randelhoff, A.: Turbulent heat and momentum fluxes in the upper ocean under Arctic sea ice, Journal of Geophysical Research - Oceans, 122, 1–18, doi:10.1002/2016JC012283, 2017.

Petrich, C. and Eicken, H.: Growth, Structure and Properties of Sea Ice, in: Sea Ice, edited by Thomas, D. N. and Dieckmann, G. S., chap. 2, pp. 23–77, John Wiley & Sons, 2nd edn., 2010.

Rösel, A., Bratrein, M., King, J. A., Itkin, P., Divine, D., Ervik, Å., Gallet, J.-C., Gierisch, A., Haapala, J., Oikkonen, A., Liston, G. E., Nicolaus, M., Polashenski, C. M., Spreen, G., Gerland, S., Granskog, M. A., and Perovich, D.: N-ICE2015 ice thickness from hot wires [Data set], doi:10.21334/npolar.2016.263a317f, 2016.

Shestov, A.: Field report on the Ridge activity during N-ICE2015, Leg 6, Tech. rep., UNIS, 2017.

Sirevaag, A.: Turbulent exchange coefficients for the ice/ocean interface in case of rapid melting, Geophysical Research Letters, 36, L04 606, doi:10.1029/2008GL036587, 2009.

Turner, J. S.: The Melting of Ice in the Arctic Ocean: The Influence of Double-Diffusive Transport of Heat from Below, Journal of Physical Oceanography, 40, 249–256, doi:10.1175/2009JPO4279.1, 2010.

Widell, K., Fer, I., and Haugan, P. M.: Salt release from warming sea ice, Geophysical Research Letters, 33, L12 501, doi:10.1029/2006GL026262, 2006.

Paper IV

4.4 Near-inertial internal wave variability from one-year duration moored measurements near the Yermak Plateau, Arctic Ocean

Algot K. Peterson and Ilker Fer

Manuscript in preparation.

IV

Near-inertial internal wave variability from one-year duration moored measurements near the Yermak Plateau, Arctic Ocean

Algot K. Peterson and Ilker Fer

Geophysical Institute, University in Bergen and Bjerknes Centre for Climate Research, Bergen, Norway.

Correspondence to: Algot K. Peterson (algot@uib.no)

Abstract. We present observations of the near-inertial wave field from three moorings deployed for one year on the southwestern slope of the Yermak Plateau. The moorings were deployed in the path of the West Spitsbergen Current, near the marginal ice zone in a tidally active region. Near-inertial horizontal kinetic energy is sporadically elevated, particularly at the surface, in response to wind forcing, but also in intermediate and deep layers. We find an energetic clockwise polarized component, and a stronger polarization closer to the surface, both indicative of surface generation by wind. Examples of wind-generated near-inertial waves are presented. Wave lengths and velocities are found comparable to previous studies. The aspect ratio is steeper than in other studies, likely related to smaller lateral scale of the low pressure systems at high latitudes. At depth, elevated near-inertial internal wave energy can be wind-generated remotely, propagating past our moorings, or by tidal currents over rough topography. The diurnal K_1 and the semi-diurnal (near-inertial) M_2 components are the most energetic. Characteristic beam paths of a near-inertial tidal beam propagating from the shelf break are consistent with observed elevated HKE at intermediate depths.

1 Introduction

While near-inertial wave (NIW) energy under pack ice is typically 1-2 orders of magnitude lower than the values in the open ocean (Levine et al., 1985), observations have indicated an increasing seasonality in near-inertial internal wave-field, related to the decline in Arctic sea ice extent and thickness (Rainville and Woodgate, 2009; Martini et al., 2014; Dosser et al., 2016). The reduced sea ice extent has been accompanied by an increase in ice drift speed (Rampal et al., 2009; Spreen et al., 2011). The energy transfer from atmosphere to ocean has been found to be most effective over a partial sea ice cover (Schulze and Pickart, 2012; Martin et al., 2014), due to the increased drag from freely moving ice keels (Pite et al., 1995; Skyllingstad et al., 2003). On the other hand, Martin et al. (2016) found that younger, thinner sea ice leads to reduced ocean surface stress with time, because smooth sea ice gives less drag. In a comparison of historical and recent microstructure measurement campaigns in the Arctic Ocean, Guthrie et al. (2013) found no general increase in internal wave energy and mixing rates over three decades. The net effect of recent changes in the Arctic Ocean on the internal wave field is still not accurately known (Carmack et al., 2015).

Ocean current shear levels in the water column are higher over regions of rough topography compared to the abyssal plains (D'Asaro and Morison, 1992). One such region is the Yermak Plateau (YP), a topographic feature north of Svalbard, identified as a place of vigorous mixing (Padman and Dillon, 1991; Fer, 2014). The YP is typically co-located with the marginal ice

zone, where energy transfer to the ocean is more effective. Furthermore, the YP lies north of the critical latitudes (where the internal wave frequency equals the local inertial frequency) for the dominant semidiurnal M_2 (74°30'N) and diurnal K_1 and O_1 (30°) tides. Internal tidal waves at these frequencies are thus evanescent and must dissipate their energy locally (Vlasenko et al., 2005).

Along the slopes of Svalbard and the YP flows the West Spitsbergen Current (WSC), carrying warm Atlantic Water into the Arctic Ocean. The WSC through Fram Strait has an average temperature of 3.1 ± 0.1°C with a net volume transport of 6.6 ± 0.4 10^6 m^3 s^{-1}, estimated from an array of moorings between 1997-2010 (Beszczynska-Möller et al., 2012). Turbulent mixing brings up heat from underlying warm Atlantic Water, and observations in the area have repeatedly reported large vertical heat fluxes under the ice (e.g., McPhee et al., 2003; Sirevaag and Fer, 2009; Peterson et al., 2017).

We present observations of the NIW field from yearlong deployment of three moorings north of Svalbard, on the southwestern slope of the YP, where the WSC enters the Arctic Ocean. This study aims to characterize the nature of the wave field, and specifically targeting the influence of wind-generated near-inertial internal waves in a tidally active region.

2 Data and methods

2.1 Moorings

Data were collected on the southwestern slope of the Yermak Plateau, north-west of Svalbard, between 11 September 2014 and 13 August 2015 (Figures 1 and 2b) using sensors attached to three mooring lines. The moorings are named M8, M12, and M15 with the figures corresponding to the approximate isobath in 100 m where the mooring was deployed (e.g., M8 is at 800 m). This naming convention is chosen for clarity and differs from the data report (Peterson and Fer, 2017).

The moorings were equipped to measure currents, temperature and pressure at a rate of 1 hour^{-1} of higher, covering a large fraction of the water column, hence resolving the near-inertial internal wave motions. Currents were measured using acoustic Doppler current profilers (ADCPs, RDI 75, 150 and 300kHz Sentinel Workhorse) and current meters (Anderaa SeaGuard). Temperature, salinity and pressure were sampled using Sea-Bird Scientific (SBE) temperature loggers (SBE56) and conductivity-temperature-depth recorders (CTD, SBE37 and SBE39). See Table 2 and Figure 2a for details on instrument distribution on the moorings.

Occasional blow-down of the mooring lines in response to strong currents were corrected for by using the pressure record from the SBE37 and SBE39 instruments. For each hourly time step, pressure is linearly interpolated to the other instruments positions, based on the nominal target distance from the pressure sensors along the wire. Instruments sampling at frequencies higher than 1 h^{-1} were bin averaged before linear interpolation to a common grid of 1 h temporal and 5 m vertical resolution.

Before producing the gridded data set, each sensor was quality controlled individually and checked for consistency against nearby instruments, as well as against CTD profiles collected prior to the mooring recovery. When necessary, small constant offset corrections were applied to conductivity and temperature records to yield a smooth time-averaged profile. Occasional long-term blocking of conductivity cells occurred, and these data were excluded. The compass of four ADCPs malfunctioned. For these instruments, the currents are rotated to align with the nearest overlapping current measurements from an independent

Table 1. Mooring deployment and recovery details. Total depth is estimated from the deepest pressure gauge, mooring line setup and echo depth. Echo depth is as measured by the RV Håkon Mosby upon recovery of the moorings. Mooring name indicates the isobath in 100 m where the mooring was deployed. The name used in the data report (Peterson and Fer, 2017) is given in brackets.

Mooring	**M8** (Y2)	**M12** (Y3)	**M15** (Y1)
Longitude	5E 48.733	5E 56.333	5E 57.541
Latitude	80N 03.876'	79N 44.093'	79N 37.209'
Total depth	840 m	1225 m	1560 m
Echo depth	863 m	1327 m	1609 m
Deployed (UTC)	10.09.2014 09:05	11.09.2014 10:47	10.09.2014 18:55
Recovered (UTC)	13.08.2015 08:00	13.08.2015 13:00	13.08.2015 17:00

instrument, or by matching direction of currents in the nearest bins of upward and downward pointing ADCP pairs on the same buoy. Further details can be found in the data report (Peterson and Fer, 2017).

2.2 Near-inertial internal waves

2.2.1 Dispersion relation for internal waves

The dispersion relation for linear near-inertial internal waves of the form $\exp(i[\omega_i t - kx - ly - mz])$, propagating in an ocean of constant stratification N, is

$$\omega_i^2 = f_{\text{eff}}^2 + \frac{N^2 k_H}{k_H^2 + m^2}, \tag{1}$$

where ω_i is the intrinsic frequency, k_H and m are the horizontal and vertical wavenumbers, respectively (Cuypers et al., 2013). The relative vorticity, ζ, of sub-inertial motions modifies the Coriolis frequency f, such that $f_{\text{eff}} = f + \zeta/2$ (Mooers, 1975), where $\zeta = \frac{\partial v}{\partial x} - \frac{\partial u}{\partial y}$. For a propagation angle $\beta = k_H/m$ to the vertical, we can derive the vertical group velocity

$$c_{gz} = \frac{\partial \omega_i}{\partial k_H} = -\frac{(N^2 - f^2)\beta^3}{\left(k_H(1+\beta^2)^{3/2}(f^2 + N^2\beta^2)^{1/2}\right)}. \tag{2}$$

The corresponding horizontal group velocity is then given by $c_{gH} = -c_{gz}/\beta$.

2.2.2 Near-inertial frequencies

The inertial frequency is approximately semidiurnal at the mooring location ($f = 1/12.17$ cph, cycles per hour), and in fact lies between the principal lunar ($M_2 = 1/12.42$ cph) and solar ($S_2 = 1/12.00$ cph) frequencies. This complicates untangling of the near-inertial signal from the semidiurnal tide.

The near-inertial signal is isolated by applying a band-pass filter to the baroclinic currents. The baroclinic current is approximated by removing the depth-averaged current from each profile. We use a second-order Butterworth filter with 11-13 hours passband and 9-15 hours stopband, encompassing both the local inertial frequency and the semidiurnal tidal frequencies.

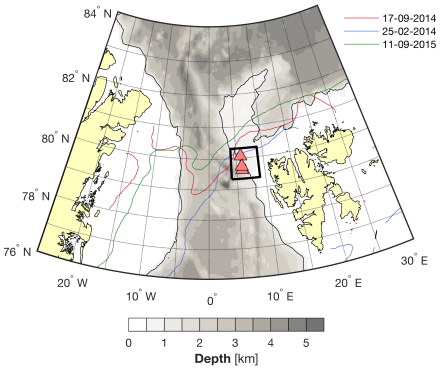

Figure 1. Overview map of the study region in Fram Strait between Greenland and Svalbard. Mooring locations are marked with triangles, and the region shown in Figure 2 is indicated by the black box. Isobaths are from 1 arc-minute resolution ETOPO Global Relief Model (Amante and Eakins, 2009), with the 1000 m contour highlighted (black). Sea ice extent from 2014/15 minimum and the 2015 maximum are shown (colored lines).

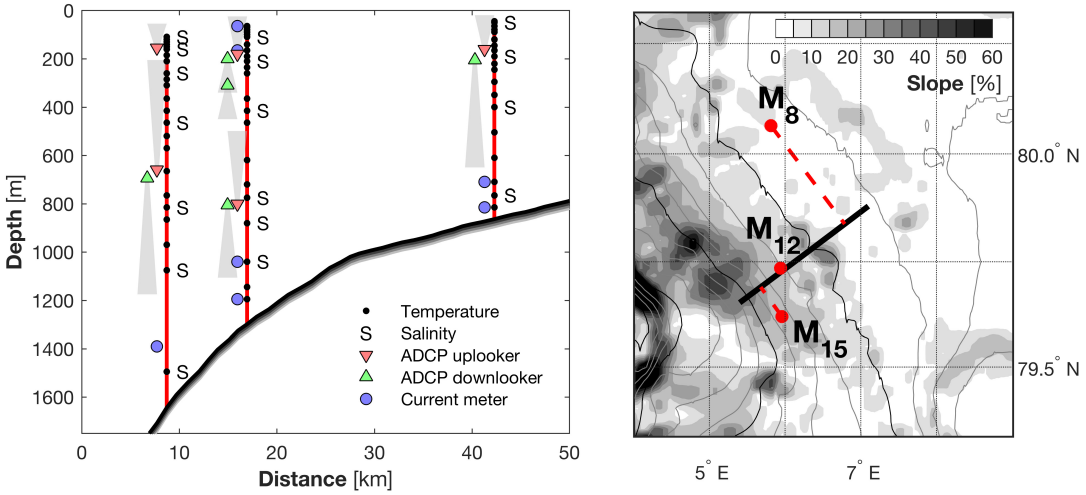

Figure 2. Overview of the mooring array. (a) Vertical section of the moorings, with sensor distribution indicated. (b) Map of the mooring locations (red dots), overlain contours of water depth every 250 m (gray) and 1000 m (black) from ETOPO-1. Shading scales with the topographic slope. The section shown in (a) is indicated by the black line.

Table 2. Mooring instrument details. Height is measured in meters above bottom (m.a.b.), and corrected using mooring line lengths and pressure record from instruments. Parameters are temperature (T), conductivity (C), pressure (P), horizontal velocity (U), vertical velocity (W) and dissolved oxygen (O). Instruments are given with their serial numbers (SN), and superscript U/D indicates up/downlooking ADCPs, respectively. Parameters marked by an asterisk (*) are only sampled by the instruments that are also marked (e.g., SBE37 SN8000 did not sample pressure).

Mooring	**Height (m.a.b)**	**Parameter**	**Instrument**
M8 (Y2)	793, 768, 738, 713, 693, 643, 618, 568, 513, 253, 153, 48	T	SBE56 (SN: 4313, 4252, 4330, 4314, 4328, 4312, 4326, 1965, 1953, 4334, 4321, 4315)
	803*, 673*, 463, 98*	C, T, P*	SBE 37 (SN: 5448*, 5451*, 8000, 5452*)
	692^{U}	U, W	RDI 150 kHz (SN: 17226)
	690^{D}	U, W	RDI 75 kHz (SN: 18447)
	48	T, C, U	RCM7 (SN: 10983)
	808		SS37 ORE
M12 (Y3)	177, 602, 702, 857, 962, 1062, 1087, 1132, 1182, 1122, 1132, 1237, 1247	T	SBE56 (SN: 4320, 4310, 4319, 4317, 4311, 4318, 4316, 4232, 4327, 4200, 4335, 4203, 4333)
	273*, 447, 552, 907, 1117*, 1217*	C, T, P*	SBE37 (SN: 7373*, 7222*, 7821, 7335, 8971*, 5446*)
	503^{U}, 1128^{U}	U, W	RDI 150 kHz (SN: 18595, 17227)
	501^{D}, 1012^{D}, 1126^{D}	U, W	RDI 300 kHz (SN: 17319, 10149, 15331)
	122, 1152*, 1252*	C, T, P, U, O*	SeaGuard (SN: 240, 1321*, 1318*)
	287	U, T	RCM7 (SN: 11064)
M15 (Y1)	639, 744, 844, 944, 1089, 1194, 1299, 1324, 1399, 1424, 1459, 1469, 1479, 1489	T	SBE56 (SN: 1340, 1955 1347 1962 1951 1328 1954 1948 4331 4329 4332 4322 4323 4325)
	1039, 1244	T, P	SBE39 (SN: 6144, 6146)
	114*, 534, 794*, 1144, 1349*, 1449*, 1499*	C, T, P*	SBE37 (SN: 6097*, 7334*, 8970*, 8975, 7372*, 8973, 6018*)
	1449^{U}	U, W	RDI 300 kHz (SN: 13771)
	941^{D}, 943^{U}	U, W	RDI 75 kHz (SN: 21447, 21444)
	219, 444	T, C, U	RCM7 (SN: 4223, 1586)

In the presence of a mean flow, Doppler shifting causes the intrinsic (Lagrangian) frequency to differ from the observed (Eulerian) frequency:

$$\omega_i = \omega_o + \mathbf{k_H} \cdot \mathbf{U}, \tag{3}$$

where boldface types represent vectors of horizontal wavenumber and currents. The ratio of near-inertial horizontal kinetic energy (E_K) to near-inertial available potential energy (E_P) relates the intrinsic inertial frequency to the effective Coriolis frequency as

$$r = \frac{\omega_i}{f_{\text{eff}}} = \sqrt{\frac{R+1}{R-1}}, \tag{4}$$

where $R = E_K/E_P$ (Cuypers et al., 2013; Fofonoff, 1969).

Near-inertial internal waves are generated by winds at the surface, or at these latitudes, by semidiurnal tidal currents over bottom topography. Their initial direction of propagation from the generation site is thus opposite, which can be used to determine the origin of observed near-inertial signals in the ocean. The Earth's rotation causes the velocity vectors of an internal wave to rotate clockwise (CW) in time. Rotation with depth is thus CW for waves with downward energy propagation, and counter-clockwise (CCW) for upward energy propagation (Leaman and Sanford, 1975). The direction of phase propagation is the opposite.

2.2.3 Complex demodulation

The temporal change of CW and CCW rotary amplitude and phase of a particular frequency component of the velocity time series can be obtained from complex demodulation of the complex velocity time-series (Emery and Thomson, 2001, pp 402-404). Single or multiple waves can be fit to sequential segments of the time series using least-squares algorithms. The segment size is typically at least twice the length corresponding to the target frequency of the wave of interest. To resolve multiple frequency demodulations, the theoretical considerations set the minimum segment length to that corresponding to the inverse of the frequency difference of two waves. This analysis is particularly useful in identifying frequencies of observed NIWs which can vary depending on Doppler shifting and the latitude or background vorticity of where a storm generated inertial waves.

The observed inertial frequency, ω_o, varies in time and also between the mooring locations. In order to identify ω_o accurately at each mooring, we run the complex demodulation for a set of densely spaced NIWs with frequencies at $0.1f$ intervals between $0.8f$ and $1.3f$. To resolve $0.1f$, a minimum segment length of 20 days is required. We demodulate the baroclinic current averaged in the upper 150 m using 30 d segments, shifted by 12 h, providing the amplitude and phase evolution for the set of waves. At each time step ω_o is identified as the frequency with the greatest amplitude. Over the one-year deployment duration, the observed inertial frequency varies between $0.89f$ and $1.10f$, and a variation of up to 15% is found between the moorings. This step gives us a time series of ω_o at hourly resolution, for each mooring.

Once the dominant near-inertial frequency is identified, complex demodulation technique is used once more on the baroclinic currents, at each vertical level. This time demodulation was done for a single frequency, i.e., the ω_o at the observation time.

Typically 1-day length segment is sufficient for this analysis. We opted to use 6-hour moving 5-day windows, over which we assume that the NIWs are coherent (ω_o at the mid-time of each 5-day window is used). The results are not sensitive to the choice of 1 or 5 day segment length. For each mooring, full-depth time series of rotary component amplitude and phases are obtained.

2.2.4 Stratification

Stratification is given by buoyancy frequency, calculated as $N^2 = \frac{g}{\rho_0}\frac{\partial \sigma_0}{\partial z}$, where $g = 9.81$ m s^{-2} is the gravitational acceleration, and we use a reference density $\rho_0 = 1028$ kg m^{-3} and the vertical gradient of potential density $\sigma_0(z)$.

Differences in stratification with depth causes internal waves to refract as they propagate. This effect is commonly mitigated using "Wentzel-Kramers-Brillouin", or WKB stretching, of the vertical coordinate (Leaman and Sanford, 1975), using a constant reference stratification, N_0. Furthermore, in order to use the theory and equations given for constant stratification in Sections 2.2.1 and 2.2.2, we make the WKB-approximation, whereby the velocity and energy are scaled by the observed stratification profile $N(z)$. The WKB-approximation assumes that the background stratification varies slowly and smoothly over a vertical scale larger than that of the wave.

The stretched depth is calculated as

$$z_{\mathrm{WKB}} = \int_0^z \frac{N(z')}{N_0} dz'. \tag{5}$$

The velocity components are scaled by multiplying by a factor of $[N_0/N(z)]^{1/2}$, energy by a factor of $[N_0/N(z)]$. The reference stratification is $N_0 = 1$ cph, obtained as the annual average of the depth average over the upper 500 m, over three moorings.

3 Environmental setting

Winds from ERA-interim reanalysis (Figure 3a) show several strong wind events through the deployment. There is a seasonal cycle in wind forcing, with generally stronger winds in winter, with the exception of January. Storms occur throughout, with strongest winds typically from the northeast. A seasonal cycle, with a dip in January, is also apparent for surface wind stress Figure 4a. Wind speed mean rate of change and wind speed variance are also quite variable through the year Figure 4, and the former also exhibits a seasonal cycle, with more variability in the winter months.

Sea ice concentration in the mooring area is highly variable, and without a clear seasonal cycle (Figure 3b). The mooring locations are never entirely ice covered, with a maximum ice concentration of $\sim$50% at M8. Sea-ice is advected to the mooring locations by wind forcing (Figure 3a), with northerly winds consistently increasing ice concentrations. Although air temperatures averaging to -10°C in winter (Nov-Mar), the local ice production is never sufficient to create a full ice cover.

The AW is carried north-westwards along the topographic slope by the barotropic current (Figure 5). The M12 (middle) mooring shows the most consistent direction, with an average barotropic current over the whole deployment of 8 cm s^{-1}. While

the M8 mooring had virtually the same barotropic current speed, the net northward velocity is only 3 cm s^{-1}. There is a strong seasonal cycle in barotropic current, with higher velocities observed in winter months (November-April). On a monthly scale variations in barotropic currents are out of phase on several occasions, notably between January-April, indicating meandering of the boundary current. This leads to a higher horizontal shear in the barotropic current (Figure 4c).

The full current record from M12 is shown in Figure 3c and d, confirming the typical north-westerly current direction, but significant baroclinic components can be identified from time to time, both as surface- and bottom intensification. This is also evident by the elevation in near-inertially band-passed horizontal kinetic energy (HKE) at M12 (Figure 3e). Corresponding time-series of current speed and near-inertial HKE are shown for moorings M8 and M15 in Figures A1 and A2, respectively.

Vertical shear of the current is calculated between 70 m and 500 m depth (Figure 4d). While vertical shear is positive throughout in M8 and M12, the monthly averages are negative in February through April for M15. A negative vertical shear means that currents at 70 m are stronger than those at 500 m.

4 Tidal analysis

A tidal analysis is made from the observations, using the four major constituents K_1, O_1, M_2 and S_2. The amplitude of the constituents vary through the year, and tidal analysis is run over 30-day windows to make a time series of the tidal forcing through the year. The analysis window length is sufficient to resolve the constituents. Details of the analysis and the temporal variation of the constituents are given in Appendix B.

The mooring observations and our tidal predictions are compared to results from the high-resolution Arctic Ocean tidal inverse model AOTIM-5 (Padman and Erofeeva, 2004). See the detailed comparison in Appendix B. Figure 6 shows a 14 day excerpt. The model includes the four most energetic components, which were also used in our tidal prediction. Tidal elevation is generally in good agreement with the deepest pressure record from M15 (SBE37, SN6018), with tidal elevations of up to 1 m. AOTIM results are also in agreement with the tidal prediction, with a close agreement in phase. The discrepancy in amplitude between tidal prediction ('t_tide') and the observations and AOTIM is larger during neap tide. The difference between the tidal analysis and the pressure record comes from the contribution from other tidal frequencies and from variations in atmospheric forcing. From a comparison between the modeled tidal current speed and the observed barotropic current we see that the strong background current is modulated by the tidal forcing (Figure 6b). The tidal signal is also apparent in the vertical isopycnal displacement (Figure 6c), but will typically also be altered by internal waves.

5 Near-inertial internal waves

Frequency spectra of the baroclinic horizontal velocity at two levels measured at M15 are shown in Figure 7. The currents at 150 m are more energetic than at 750 m, and at low frequencies the CCW variance dominates over CW. The peaks at near-inertial (f, M_2) and diurnal (K_1) frequencies stand out in the CW component, but are absent in the CCW. Because CW rotation

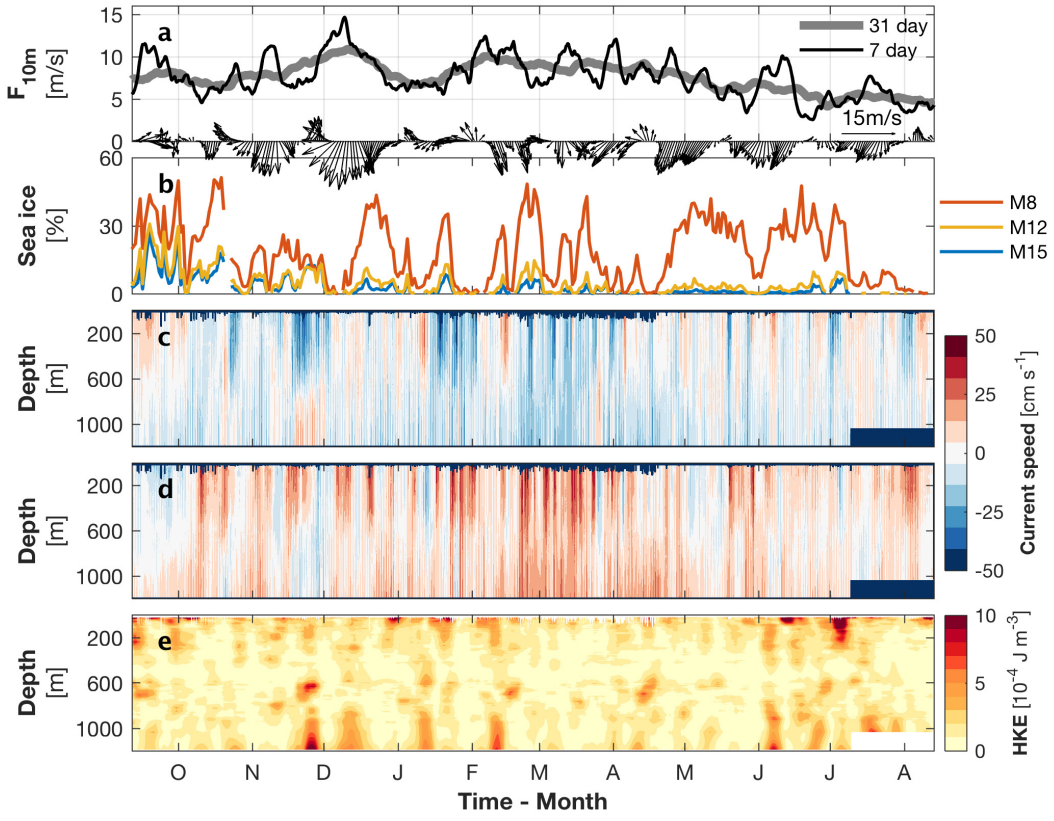

Figure 3. Time-series of (a) wind speed and 7-day running mean wind arrows from 6-hourly ERA-Interim reanalysis, (b) satellite-derived sea ice concentration interpolated to the mooring locations, (c) East and (d) North baroclinic currents and e) horizontal kinetic energy, HKE at M12. Sea ice concentrations are obtained from the Norwegian Meteorological Institute.

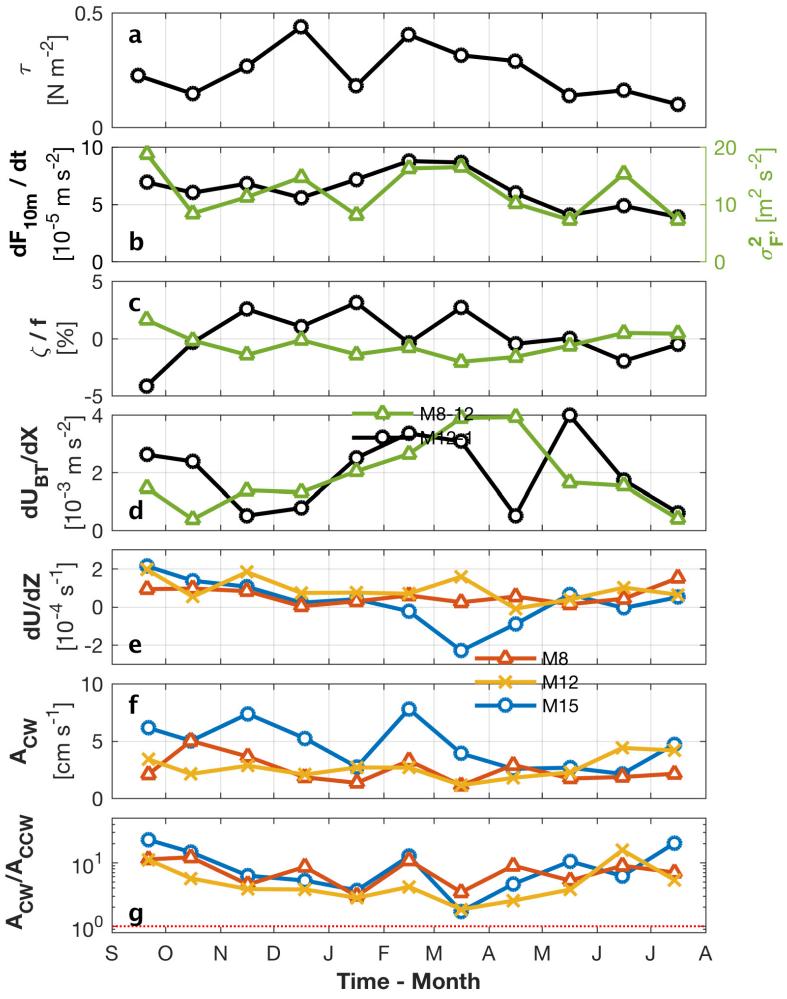

Figure 4. Monthly averaged time series of forcing and response variables. Wind forcing is from ERA-Interim reanalysis, showing (a) surface wind stress and (b) wind speed rate of change (black) and variance (green). Shear is calculated (c) laterally in barotropic currents between the moorings, and (d) vertically between 70 and 500 m for each mooring. Demodulated currents at near inertial frequency, shown as (e) clockwise rotating amplitude and (f) the ratio of clockwise/counterclockwise amplitudes, averaged between 100 to 150 m.

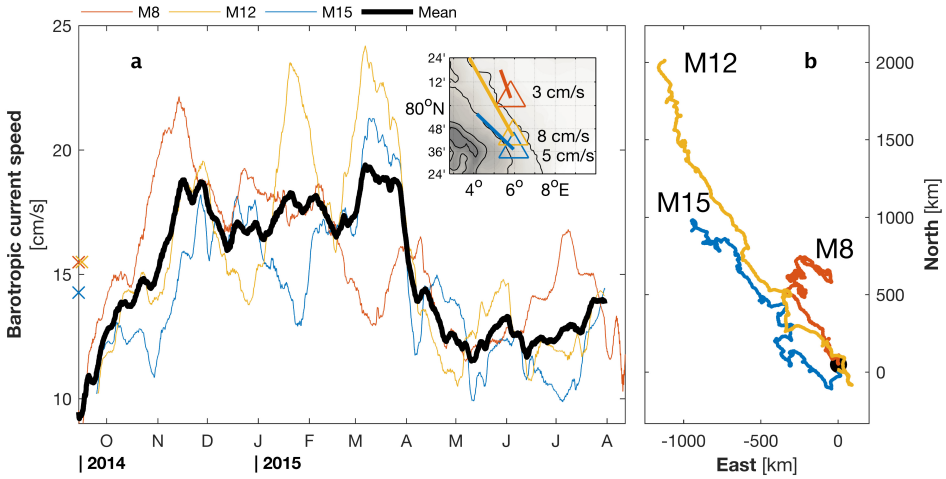

Figure 5. Barotropic currents calculated between 100 m and 500 m at each of the mooring locations. (a) Time series for each mooring and the average of the three (thick line), smoothed with a 28 day running average. Average speed is indicated by crosses on the left axis. The deployment-averaged barotropic current is shown as arrows in the inset map. (b) Progressive vector-diagram of barotropic currents.

indicates downward propagating energy, we use complex demodulation (Section 2.2.3) to separate the rotating components at the observed near-inertial frequency.

Current amplitude of CW rotation sporadically shows significant peaks (Figure 8). Amplitudes are typically highest closer to the surface, and usually dominate over the CCW rotating component, as was also noted from the spectra (Figure 7). As suggested from the CW rotation, time-series at individual depth shows that the peaks propagate downward with time. This is particularly pronounced in February, when both CW amplitude and CW/CCW ratio show the peak appearing sequentially later deeper levels. The CW polarization is however weaker than that found at lower latitudes. For example, two years of moored observations in the northern Pacific Ocean revealed that energy at the near-inertial frequency was more than 200 times the CCW energy (Alford et al., 2012).

From the observed peaks in CW rotating amplitude, coinciding with relatively weak CCW amplitude (Figure 8), we choose two example events, from February and July 2015. Near-inertially band-passed currents and CW rotating amplitude from complex demodulation for the upper ocean during the two events are shown in Figure 9. Elevated current velocity initially starts near the surface, gradually spreading down, reaching 300-400 m in 5-7 days in both cases. Similar signal is identified by both near-inertial band-passing (upper panels) and complex demodulation (lower panels). The enhanced near-inertial signal is preceded by changes in the wind field. The February event is stronger than the July event in terms of both wind forcing and upper ocean response, although the energy propagating below the upper 100 m is similar in both cases.

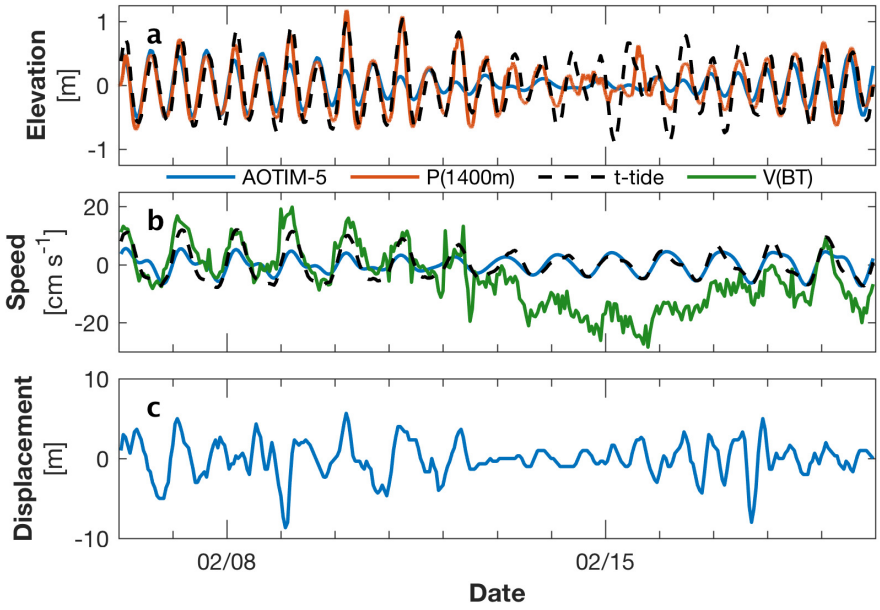

Figure 6. 14-day time-series of (a) vertical elevation from tidal model AOTIM-5, pressure record from deepest instrument on M15 and predicted tidal elevation using t-tide; (b) current speed from AOTIM-5 and barotropic current at M15; (c) isopycnal displacement at M15.

5.1 Wave characteristics

We infer wave characteristics by identifying individual NIW packets, following Cuypers et al. (2013). First, the baroclinic velocity field is separated into upward and downward propagating phases. This is done by applying a 2D fast Fourier transform (FFT) filter, and the downward (or upward) components are removed before performing the inverse 2D FFT filter to obtain the component with upward (downward) propagating phase. This method has the advantage that it can also be applied to scalar fields, and we apply the method to density fluctuations to calculate potential energy later on. Note that the data are not band-pass filtered for this step of upward/downward propagating phase component separation.

The upward propagating phase component (corresponding to downward energy propagation) is then demodulated for the observed near-inertial frequency ω_o, to obtain the phase and rotary amplitudes of downward propagating energy.

Contours of velocity for the upward propagating phase of the meridional component, $\mathbf{U_{up}}$, are shown for an example event from September/October 2014, with corresponding CW rotating current amplitude in Figure 10. Here, the upward propagating

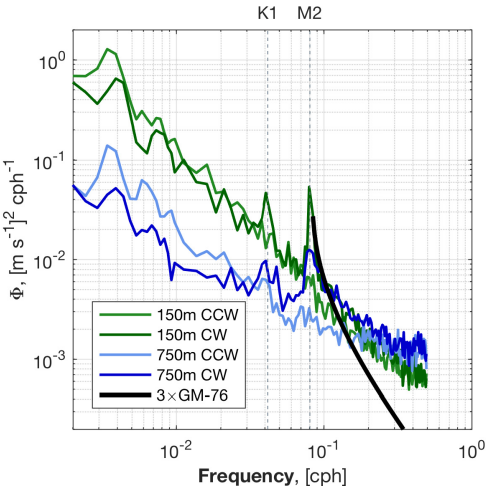

Figure 7. Rotary frequency spectra of horizontal baroclinic velocity from the M15 mooring. Spectra are calculated for two selected depths, using an FFT length of 2048, and averaged in bins of f. The Garrett-Munk universal spectrum (Garrett and Munk, 1975) is calculated using a local time-average of N, and multiplied by a factor of three for comparison.

phase comes out clearly, indicating a downward propagation of energy. Coherent wave structures are visible in Figure 10, interrupted by transitions which are less structured.

Figure 11 shows a profile from the example in Figure 10, at the time indicated by the black triangle. To account for varying stratification with depth, we use WKB-stretched coordinates (Section 2.2.4). CW amplitude dominates over CCW throughout, and individual wave packets can be identified as segments where phase changes linearly with depth (Cuypers et al., 2013). Vertical wave number m is calculated for each segment by a linear fit $\Phi_{up}(z) = mz$ to the phase profile. The wave packets are associated with peaks in the CW amplitude. Between the identified wave packets, CW amplitude reaches a minimum, and phase decreases with depth.

To obtain the energy ratio R, needed for calculation of the intrinsic frequency (ω_i, Equation 4), we calculate the near-inertial horizontal kinetic and available potential energy density from only the upward phase propagation components. The near-inertial contribution is extracted by bandpass filtering the density and velocity fluctuations with a 3rd order Butterworth filter around ω_o, using a passband $(0.85 - 1.15)\ \omega_o$ and a stopband $(0.7 - 1.3)\ \omega_o$. The corresponding near-inertial horizontal kinetic and available potential densities are

$$E_K = \frac{1}{2}\frac{\rho_0}{N^2}\left(\frac{g\rho'_{up}}{\rho_0}\right) \qquad \text{and} \qquad E_P = \frac{1}{2}\rho_0\left({u'_{up}}^2 + {v'_{up}}^2\right)^2, \tag{6}$$

where ρ'_{up}, u'_{up} and v'_{up} are the near-inertial band-passed, upward phase (downward energy) propagating components. The ratio $R = E_K/E_P$ is calculated as an average over 24 hours centered on the profile time. Resulting intrinsic frequency for the

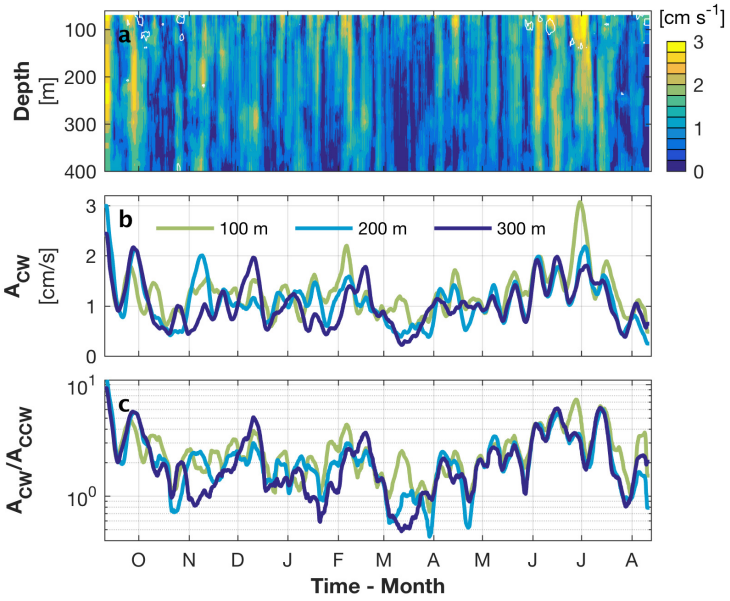

Figure 8. Near-inertial current amplitude at mooring M12, obtained from complex demodulation. Clockwise rotating component is for (a) the upper 400 m, (b) 7 day running average at selected depths, and (c) the ratio of clockwise to counter-clockwise amplitudes at the same depths. White contours in (a) are the 0.05 s^{-1} isolines of clockwise rotating near-inertial shear.

wave packets exemplified in Figure 11, calculated from Equation 4, are shown in Figure 11d, normalized by the local f. The wave packets are super-inertial.

The difference between intrinsic frequency and observed frequency is caused by Doppler shifting. Doppler shifting of the intrinsic frequency is given in Table 3, and averages to 8% of the local f.

Intrinsic frequency is further used to calculate the horizontal wave number from Equation 1, from which we can calculate the vertical and horizontal group velocities (Equation 2). The resulting group velocities are shown in Figure 11c, and an overview of the calculated wave characteristics are given in Table 3. Confidence intervals are calculated from the standard error of the wave slope fit. Note that the two middle wavegroups have smaller confidence intervals, and are thus more reliable estimates.

The intrinsic frequency can also be calculated from Equation (3), as $\omega_i = \omega_o + |k_H||\mathbf{U}|\cos(\theta - \alpha)$, where θ and α are the horizontal direction of propagation of NIWs and the mean current, respectively. The angles are calculated for each wave packet, averaging over the depth range of the wave packet, and a 12 hour window. Mean current components are used to find α, while the average direction of the maximum amplitude at each depth is calculated for θ, representing the major axis of the wave

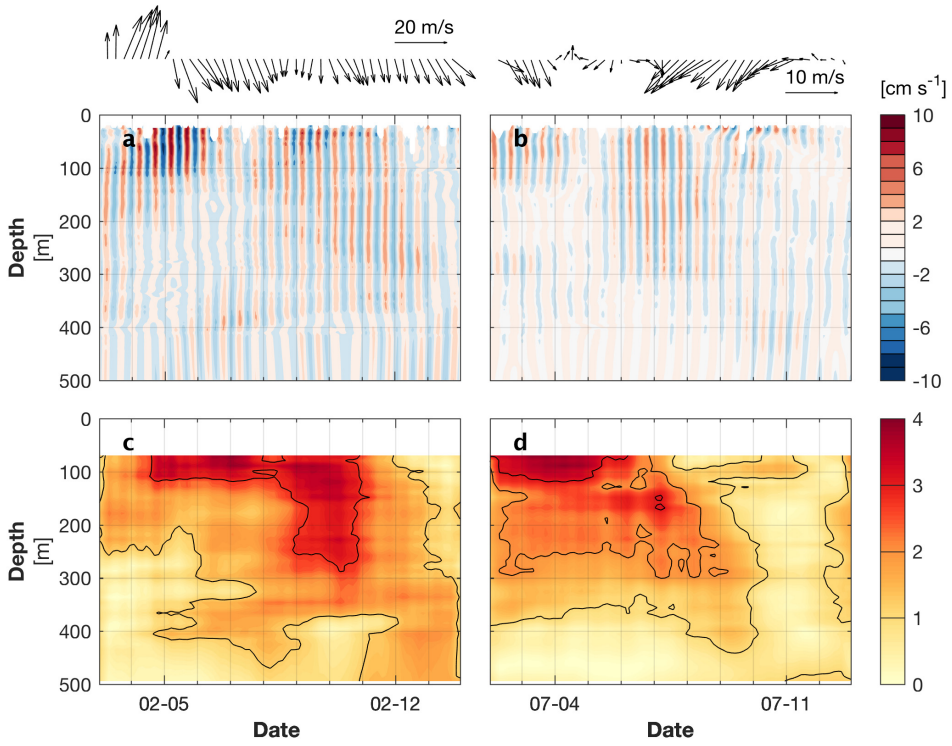

Figure 9. Two example time-series of near-inertial energy propagation in the upper ocean, from mooring M12 in (left) February and (right) July 2015. Upper panels (a & b) shows near-inertial band-passed northward velocity and below (c & d) are 15-hour running averaged clockwise rotating near-inertial current amplitudes from complex demodulation. Wind arrows from ERA Interim (6-hourly) are shown at the top.

Table 3. Wave characteristics for the wave groups identified on September 30, shown in Figure 11: Normalized intrinsic frequency, normalized Doppler shift (DS), near-inertial horizontal kinetic energy and its ratio (R) to available potential energy, vertical- and horizontal wavelengths, vertical- and horizontal group velocities. The observed frequency was $\omega_o = 0.5134$ cpd (cycles per day). Upper and lower bounds are given in brackets, calculated from the standard error of the vertical wavenumber slope fit.

Wave group	ω_i/f	DS$/f$	HKE $[10^{-3}$ J m$^{-3}]$	R	λ_z [m]	λ_H [km]	c_{gz} [cm s^{-1}, m d^{-1}]	c_{gH} [cm s^{-1}, km d^{-1}]
WG1	1.076	0.083	19	16	$396\,[343-467]$	$11\,[9.8-13.3]$	$0.11\,[0.04-0.34], 96$	$3.2\,[1.4-7.2], 2.7$
WG2	1.036	0.043	27	45	$379\,[369-390]$	$18\,[17.7-18.7]$	$0.04\,[0.03-0.05], 34$	$1.9\,[1.6-2.2], 1.6$
WG3	1.027	0.034	21	73	$349\,[334-366]$	$28\,[27.0-29.6]$	$0.02\,[0.02-0.03], 19$	$1.8\,[1.4-2.3], 1.6$
WG4	1.157	0.165	18	8	$453\,[431-477]$	$10\,[9.3-10.3]$	$0.28\,[0.19-0.41], 243$	$6.1\,[4.68.1], 5.3$

packet. This alternative calculation of ω_i provides a consistency check for the calculated wave properties. For the four wave packets in Figure 11, the calculated values of ω_i differ by 6% on average.

Kawaguchi et al. (2016) found WKB-stretched vertical wavelengths of 315 m and 190 m for two near-inertial peaks over the Chukchi plateau during ice-free conditions. From upper ocean microstructure measurements below sea ice near the North Pole, Fer (2014) found a near-inertial response to a passing storm, forcing waves of horizontal wavelength in the range 7-23 km, and dominant vertical scale for near-inertial motions of 128 m. At Ocean Station Papa in the northern Pacific, Alford et al. (2012) determined properties of a number of near-inertial internal wave groups, and found an average vertical group velocity of $c_{gz} = 13$ m d^{-1}, a vertical wavenumber peak in shear around 250 m for downgoing near-inertial motions. During a tropical storm, Cuypers et al. (2013) found vertical wavelengths of typically 100-300 m, found at depth down to their maximum measurement depth of 1000 m. Meyer et al. (2016) characterized near-inertial internal waves from a large dataset of drifting profilers near the Kergeulen Plateau in the Southern Ocean, and found mean vertical and horizontal wavelengths of 200 m and 15 km, respectively, and a horizontal group velocity of 3 cm s^{-1}. We conclude that the wave characteristics observed here are within the range of previous observations.

The aspect ratio of the wave groups are calculated as $\beta = k_H/m$, and averages to $\beta = 0.029$ for the values in Table 3. This is steeper than wave groups identified elsewhere, e.g. in Meyer et al. (2015), average of 45 wave groups near the Kerguelen Plateau was $\beta = 0.014$, and for the tropical storm studied in Cuypers et al. (2013), $\beta = 0.003$. This is likely a consequence of the lateral scale of the forcing. For wind-induced NIWs, smaller horizontal extent would be expected due to smaller scale of low pressure systems at high latitudes.

6 Generation mechanisms

A number of forcing mechanisms exists that can cause the generation of near-inertial internal waves, and their relative importance is generally unknown. The equations of motion are resonant at the inertial frequency, which is why nearly any forcing

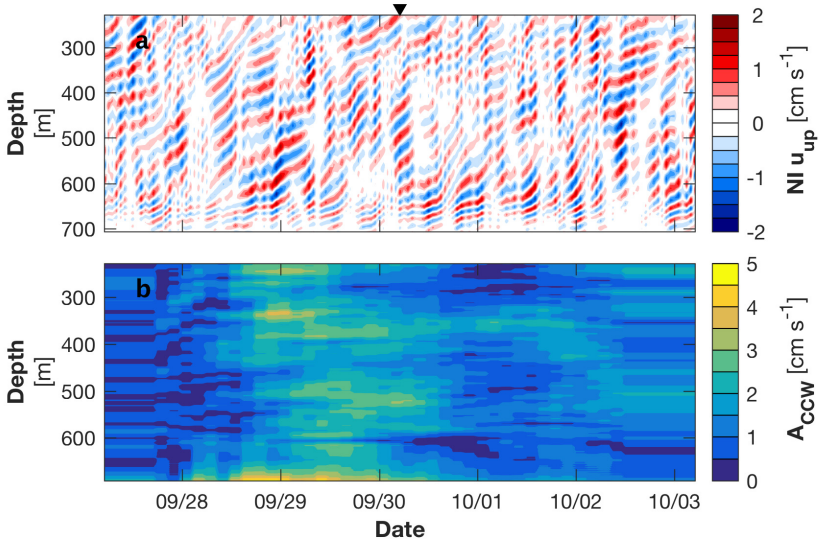

Figure 10. Example event of downward propagating wave packets at mooring M8 in September 2014. Amplitudes of (a) near-inertial current speed of the upward propagating phase component, and (b) clockwise rotating current velocity from complex demodulation.

can cause a near-inertial response (Alford et al., 2016). Wind forcing at the surface is believed to be most important, and is considered further in Section 6.1. Around the Yermak Plateau, the strong tidal currents are another likely source of generation, discussed in Section 6.2. Spontaneous generation of NIWs was modeled for the Kuroshio Front, although 85% of the energy was reabsorbed by the front rather than dissipating or radiating away (Nagai et al., 2015). Other mechanisms include nonlinear wave-wave interactions, lee-wave generation and formation through loss of balance (Alford et al., 2016), but these are not pursued further here.

6.1 Wind-generation

As the examples in Figure 9 illustrated, wind forcing is found to generate a near-inertial response, causing energy propagation to the interior. The dominant CW rotation observed at the near-inertial frequency (Figure 7), and the reduction of A_{CW}/A_{CCW} with depth (Figure 8) means that downward energy propagation exceeds upward propagation, and shows the importance of surface generation.

Wind work done by the wind on the mixed layer is calculated from near-inertial winds and mixed layer currents as $\Pi = \tau_{in} \cdot \mathbf{u}_{in}$ (Alford et al., 2012). We use wind from ERA-Interim reanalysis (Figure 12a) and currents averaged over the upper 100 m to obtain the wind work (Figure 12b).

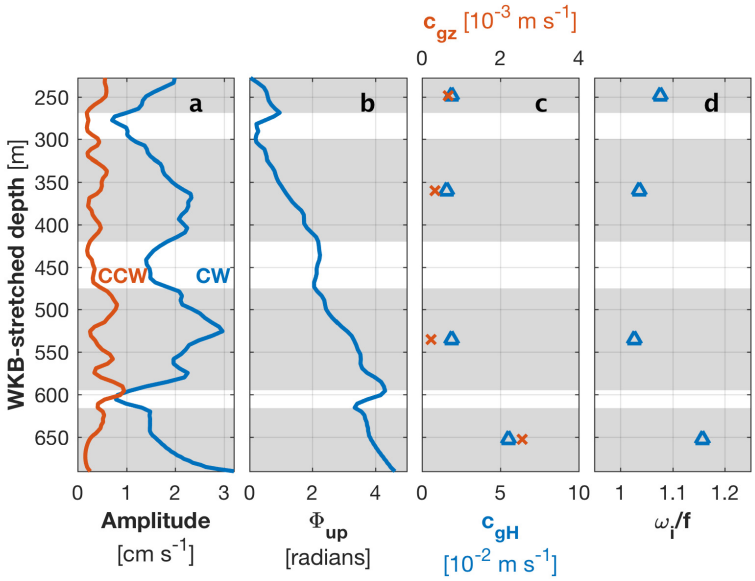

Figure 11. Profiles corresponding to the event shown in Figure 10, displaying (a) CW and CCW rotary amplitudes, (b) upward phase component. Identified wave packets are shown in shading, for which we calculate (c) horizontal and vertical group velocity, and (d) normalized intrinsic frequency.

Surface winds are generally the suspected generation mechanism of the downward propagating NIWs observed here. The lack of a clear correlation between wind work and near-inertial HKE in Figure 12 may be caused by the inability of reanalysis products in resolving major NI events. Alford et al. (2012) showed that NCEP reanalysis data failed to reproduce the two strongest events during a yearlong record in a slab model. Additionally, polar lows are commonly observed at high latitudes, but the dynamical intensity of polar lows are typically underestimated in ERA-Interim (Zappa et al., 2014).

NIWs can also be generated remotely and propagate southward. Elevated near-inertial up-phase HKE at intermediate depths may thus still have been generated by wind work at the surface. With a typical C_{gz} of 25 m d^{-1}, it would take 12 days to reach 300 m depth, during which a wave group can propagate some 20-30 km in the horizontal, according to the characteristics found for wave groups 2 and 3 (Table 3).

6.2 Tidal generation

Internal tidal waves are generated by interaction between tidal currents and topography. Since the M2 and S2 frequencies are within the near-inertial band, they are likely to generate a near-inertial internal response over topography. We find that several of the tidal ellipses are oriented on- or off-slope (Appendix B), rather than along-slope, which causes the tidal currents to move

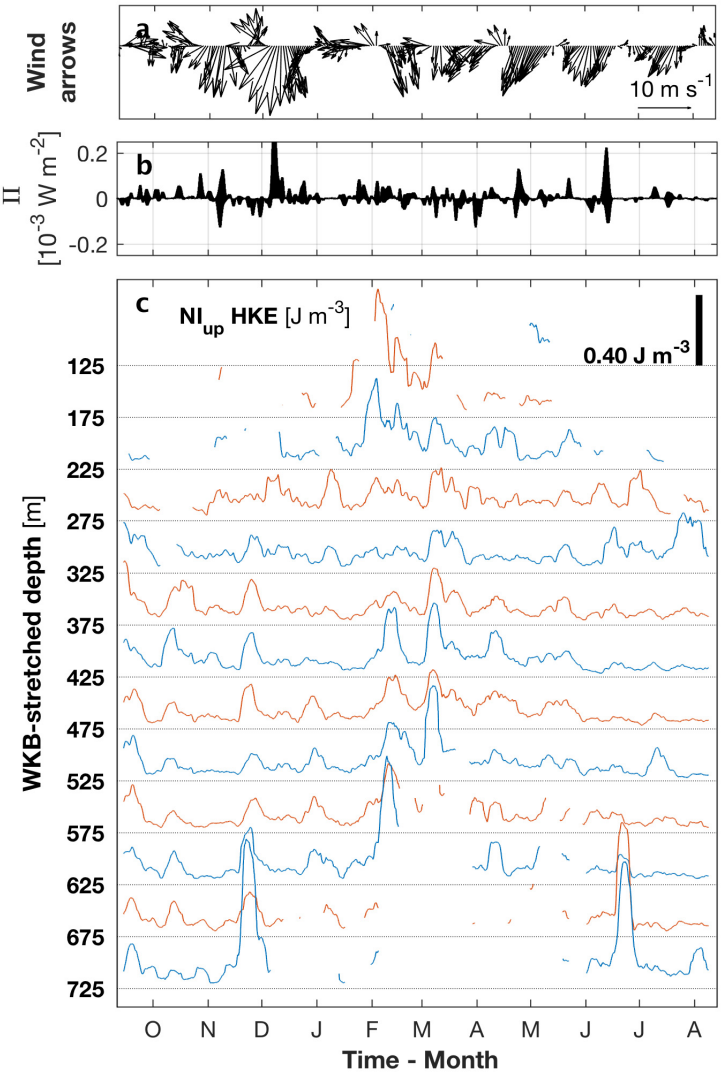

Figure 12. (a) Wind arrows from ERA-interim, (b) wind work calculated from ERA-interim winds and near-inertial band-passed upper 100 m currents, and (c) near-inertial, downward propagating horizontal kinetic energy (phase upward) at selected depths form mooring M15.

across the topography. Near-inertial tidal waves would be initiated from rough topographic features as tidal beams, following the characteristic slope

$$\beta = \frac{k_H}{m} = \frac{f^2 - \omega_o^2}{\omega_o^2 - N(z)^2}. \tag{7}$$

An example of a possible tidal beam path is shown in Figure 13, plotted over a section across the slope of the Yermak Plateau. The cross-section is shown in Figure 2b, where the slope is indicated in colors. Mooring positions have been projected onto the section along the isobaths. Near-inertial HKE is contoured between the moorings, and shows a maximum in the path of our hypothetical tidal beam. The beam is calculated using mooring stratification at the M12 mooring averaged over the whole month, but beams calculated using stratification from the high-resolution ship CTD in September, and the M12 September average, are shown for reference.

The elevated HKE at mid-depth is thus consistent with an upward propagating near-inertial tidal wave, generated at the shelf break. At mooring M12, elevated near-inertial HKE is found at depths around 600-800 m on several occasions (Figure 3e). This is consistent with the tidal beam path indicated in Figure 13.

The Yermak Plateau lies north of the critical latitudes of both M_2 and S_2, forcing the internal tide to dissipate locally (Simmons et al., 2004). Internal tides generated over topography has often been related to enhanced turbulent mixing, both over the YP and elsewhere in the Arctic Ocean (D'Asaro and Morison, 1992; Fer et al., 2015; Lenn et al., 2011; Rippeth et al., 2015).

7 Conclusions

The near-inertial internal variability on the southwestern Yermak Plateau is studied using data from a yearlong deployment of three moorings. Baroclinic currents are strongly clockwise polarized at the near-inertial and diurnal tidal frequencies. The clockwise polarization of near-inertial currents indicates downward energy propagation. Polarization is stronger near the surface, which further supports surface generation by winds.

Examples of wind-generated NIW propagation are presented, and downward propagation of near-inertial energy is found both through near-inertial band-passing and through complex demodulation at the observed near-inertial frequency. Wave groups characteristics were calculated from one example event, which had stretched vertical wavelengths of 350-450 m, horizontal wavelengths of 10-30 km and horizontal group velocities of 1.6-5.3 km d^{-1}. A higher aspect ratio indicates a steeper propagation compared to other studies. The wave frequencies are Doppler shifted 8% on average by the mean current.

A tidal analysis shows dominant K_1 and S_2 components, in agreement with studies from other parts of the Yermak Plateau. A significant seasonal cycle is found for the diurnal K_1 component. Several of the tidal ellipses are oriented on-slope, rather than along-slope. Across-slope tidal currents likely generates near-inertial internal waves by interaction with topography. Amplified near-inertial HKE at intermediate depth are consistent with a beam path of an internal wave generated by tidal currents over the shelf break. Elevated intermediate depth HKE is also seen for downward propagating energy, possibly caused by surface generation of near-inertial waves at a remote location.

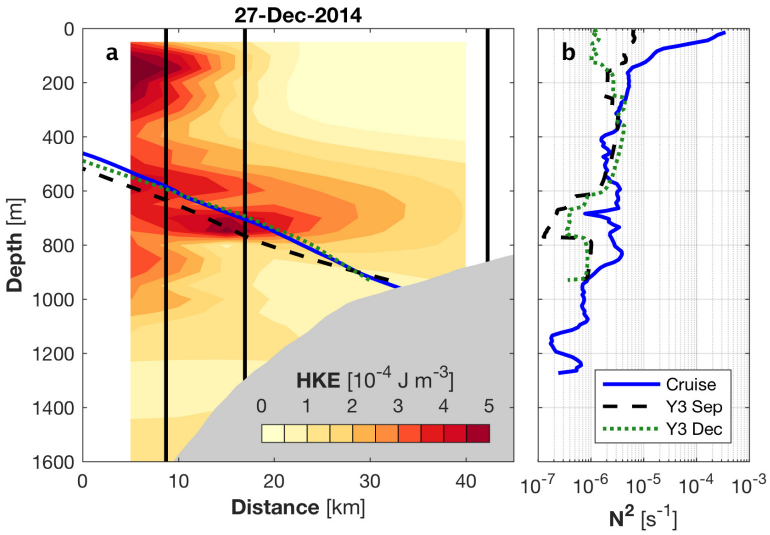

Figure 13. (a) Near inertial horizontal kinetic energy contoured between the mooring locations (vertical lines), with beam paths for a possible internal wave generated on topography indicated, calculated from (b) profiles of buoyancy frequency from a CTD cast in September 2014 (blue) and two monthly-averaged profiles from mooring M12.

Appendix A: Overview time-series

Figures A1 and A2 give an overview of the current conditions and the near-inertially bandpassed horizontal kinetic energy at moorings M8 and M15, respectively. The figures correspond to Figure 3 for mooring M12. Horizontal kinetic energy is surface intensified, and significant bottom intensification is evident in the shallowest mooring (Figure A1). Note the different depth ranges for the three moorings. The deepest current meters in all three moorings stopped logging before the end of deployment, so the full depth is not available at the end of the record.

Appendix B: Tidal analysis comparison with AOTIM

A tidal analysis of the mooring record is performed using Matlab's t_tide package (Pawlowicz et al., 2002). We apply the harmonic analysis of the four tidal constituents K_1, O_1, M_2 and S_2 over 30-day windows at each depth, following Pnyushkov and Polyakov (2011). We obtain the major and minor axes of tidal ellipses, tidal phase, ellipse inclination, the 95% confidence intervals, and a signal-to-noise ratio (SNR). The tidal characteristics are assigned to the window mid-point, and for each calculation the window is shifted by 1 hour.

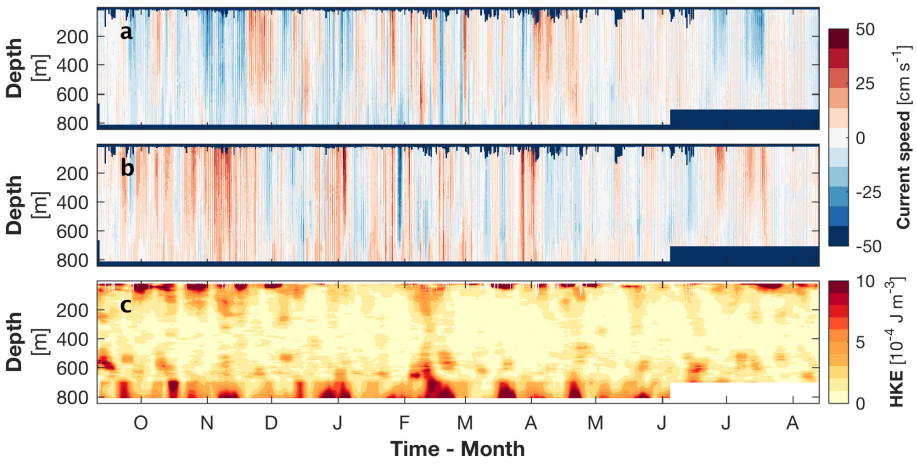

Figure A1. Time-series of (a) East and (b) North current speed at M8, and near-inertially bandpassed horizontal kinetic energy.

Figure A3 shows the variation of the four tidal constituents through the deployment, for moorings M8 and M15 (M12 is located in between and is not shown). K_1 has a strong seasonal cycle. K_1 displays a large seasonal variation, and in winter and summer, it is the dominant constituent. The M_2 has second highest amplitude, and is less variable over the year, and thus dominates the tidal variability when K_1 is weak.

In Table A1, tidal constituents from tidal analysis are compared to the AOTIM-5 results. Due to a difference between the total depth used in AOTIM and our best depth estimates (Table 1), the AOTIM values have been scaled by 4% and 3% for moorings M12 and M15, respectively, for consistency. The major axes are lower in AOTIM-5 compared to our observations, except for S_2, where there is a good agreement. Both AOTIM-5 and observations show that several of the components are directed across the slope rather than along the slope. On-slope orientation means that more energy moves across the slope, which consistent with tidal generation of internal waves at the shelf break, as discussed in Section 6.2.

Annual averages are shown in the table, but for K_1, there is a significant seasonal cycle (Figure A3). For reference, the upper quartiles of semi-major axes average to 14.1, 12.2 and 9.7 cm s^{-1}, and the lower quartiles average to 7.5, 6.0 and 4.8 cm $s^{-}1$ for the moorings M8, M12 and M15, respectively. The seasonal variation is negligible for the other constituents, which typically average to within 5% over the upper and lower quartiles.

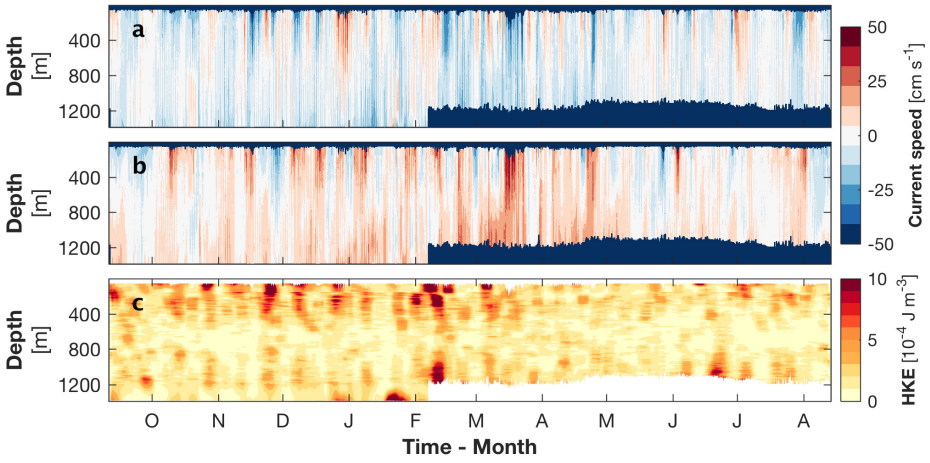

Figure A2. Same as Figure A2, but for mooring M15.

Author contributions. IF designed the study and moorings; AKP processed and analyzed the data with advice from IF. AKP drafted the manuscript. Both authors discussed and contributed to finalizing the paper.

Competing interests. The authors declare that they have no conflict of interest.

Disclaimer. TEXT

Acknowledgements. This study is supported by the Research Council of Norway, through the project 229786. Additional support was obtained from the Centre for Climate Dynamics at the Bjerknes Centre through the BASIC project. We thank Tor Gammelsrød and Jenny Ullgren and the other participants of the UNDERICE cruise on board KV Svalbard for deploying the moorings.

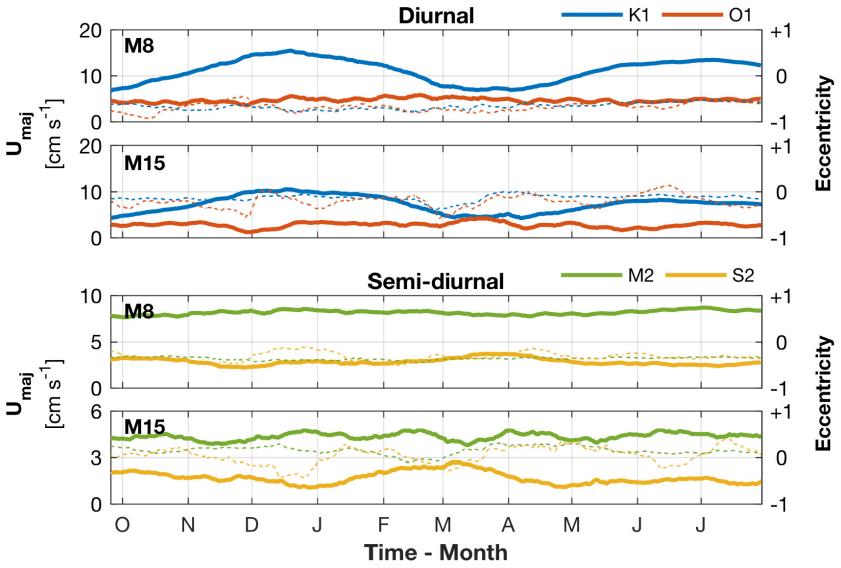

Figure A3. Tidal major axis (thick lines) and eccentricity (thin, dashed) from tidal analysis of moorings M8 and M15, for the dominant diurnal and semidiurnal frequencies K1, O1, M2 and S2. Eccentricity is positive for counter-clockwise rotating ellipses, and negative for clockwise rotation.

References

Alford, M. H., Cronin, M. F., and Klymak, J. M.: Annual cycle and depth penetration of wind-generated near-inertial internal waves at Ocean Station Papa in the northeast Pacific, Journal of Physical Oceanography, 42, 889–909, doi:10.1175/JPO-D-11-092.1, 2012.

Alford, M. H., MacKinnon, J. A., Simmons, H. L., and Nash, J. D.: Near-inertial internal gravity waves in the ocean., Annual review of marine science, 8, 95–123, doi:10.1146/annurev-marine-010814-015746, 2016.

Amante, C. and Eakins, B.: ETOPO1 1 arc-minute global relief model: Procedures, data sources and analysis, NOAA Technical Memorandum NESDIS NGDC-24, p. 19, doi:10.1594/PANGAEA.769615, 2009.

Beszczynska-Möller, A., Fahrbach, E., Schauer, U., and Hansen, E.: Variability in Atlantic water temperature and transport at the entrance to the Arctic Ocean, 1997-2010, ICES Journal of Marine Science, 69, 852–863, doi:10.1093/icesjms/fss056, 2012.

Carmack, E. C., Polyakov, I. V., Padman, L., Fer, I., Hunke, E., Hutchings, J. K., Jackson, J., Kelley, D. E., Kwok, R., Layton, C., Melling, H., Perovich, D. K., Persson, O., Ruddick, B., Timmermans, M.-L. L., Toole, J. M., Ross, T., Vavrus, S., and Winsor, P.: Toward quantifying the increasing role of oceanic heat in sea ice loss in the new Arctic, Bulletin of the American Meteorological Society, 96, 2079–2105, doi:10.1175/BAMS-D-13-00177.1, 2015.

		K1					O1				
		U_{major}	U_{minor}	Phase	Incl.	SNR	U_{major}	U_{minor}	Phase	Incl.	SNR
M8	Avg	11.1 ± 2.6	-7.4 ± 2.0	144 ± 5	41 ± 4	431	4.7 ± 0.4	-3.2 ± 0.6	300 ± 13	39 ± 15	72
	AOTIM	7.6	-4.0	353	46		2.8	-1.8	262	37	
M12	Avg	9.3 ± 2.4	-3.4 ± 1.1	230 ± 3	32 ± 3	346	3.7 ± 0.5	-2.1 ± 0.5	33 ± 11	34 ± 11	51
	AOTIM	5.9	-0.8	316	32		2.2	-0.9	226	28	
M15	Avg	7.3 ± 1.8	-1.0 ± 0.4	292 ± 3	29 ± 3	203	2.8 ± 0.6	-0.6 ± 0.4	81 ± 9	36 ± 9	30
	AOTIM	4.5	0.5	294	19		1.7	-0.4	204	20	
		M2					**S2**				
		U_{major}	U_{minor}	Phase	Incl.	SNR	U_{major}	U_{minor}	Phase	Incl.	SNR
M8	Avg	8.1 ± 0.2	-3.0 ± 0.3	303 ± 1	61 ± 2	388	2.8 ± 0.4	-0.9 ± 0.3	179 ± 4	66 ± 7	45
	AOTIM	7.4	-2.4	40	63		2.8	-0.8	273	61	
M12	Avg	5.4 ± 0.1	-0.2 ± 0.3	218 ± 1	58 ± 2	246	1.8 ± 0.4	-0.0 ± 0.2	79 ± 4	61 ± 4	31
	AOTIM	5.4	0.3	33	63		2.0	0.2	33	63	
M15	Avg	4.3 ± 0.2	0.7 ± 0.4	29 ± 3	63 ± 4	70	1.7 ± 0.4	0.1 ± 0.3	260 ± 8	75 ± 13	10
	AOTIM	1.5	1.1	34	68		1.5	0.4	204	20	

Table A1. Tidal constituents from tidal analysis of mooring data, and from the AOTIM-5 tidal model. Constituents from mooring data are averaged over the full deployment, error margins are standard deviation (95% confidence for inclination). Standard deviations are given in parentheses. Ellipses rotate counter-clockwise for positive semi-minor axes and clockwise for negative.

Cuypers, Y., Le Vaillant, X., Bouruet-Aubertot, P., Vialard, J., and McPhaden, M. J.: Tropical storm-induced near-inertial internal waves during the Cirene experiment: Energy fluxes and impact on vertical mixing, Journal of Geophysical Research: Oceans, 118, 358–380, doi:10.1029/2012JC007881, 2013.

D'Asaro, E. A. and Morison, J. H.: Internal waves and mixing in the Arctic Ocean, Deep Sea Research Part A. Oceanographic Research Papers, 39, S459–S484, doi:10.1016/S0198-0149(06)80016-6, 1992.

Dosser, H. V., Rainville, L., Dosser, H. V., and Rainville, L.: Dynamics of the changing near-inertial internal wave field in the Arctic Ocean, Journal of Physical Oceanography, 46, 395–415, doi:10.1175/JPO-D-15-0056.1, 2016.

Emery, W. J. and Thomson, R. E.: Data analysis methods in physical oceanography, Elsevier, 2nd edn., 2001.

Fer, I.: Near-inertial mixing in the central Arctic Ocean, Journal of Physical Oceanography, 44, 2031–2049, doi:10.1175/JPO-D-13-0133.1, 2014.

Fer, I., Müller, M., and Peterson, A. K.: Tidal forcing, energetics, and mixing near the Yermak Plateau, Ocean Science, 11, 287–304, doi:10.5194/os-11-287-2015, 2015.

Fofonoff, N. P.: Spectral characteristics of internal waves in ocean, Deep-Sea Research, 16, 59–71, 1969.

Garrett, C. and Munk, W.: Space-time scales of internal waves: A progress report, Journal of Geophysical Research, 80, 291–297, doi:10.1029/JC080i003p00291, 1975.

Guthrie, J. D., Morison, J. H., and Fer, I.: Revisiting internal waves and mixing in the Arctic Ocean, Journal of Geophysical Research-Oceans, 118, 3966–3977, doi:10.1002/jgrc.20294, 2013.

Kawaguchi, Y., Nishino, S., Inoue, J., Maeno, K., Takeda, H., and Oshima, K.: Enhanced diapycnal mixing due to near-inertial internal waves propagating through an anticyclonic eddy in the ice-free Chukchi Plateau, Journal of Physical Oceanography, pp. 15–0150, doi:10.1175/JPO-D-15-0150.1, 2016.

Leaman, K. D. and Sanford, T. B.: Energy propagation of inertial waves: A vector spectral analysis of velocity profiles, Journal of Geophysical Research, 80, 1975–1978, 1975.

Lenn, Y.-D., Rippeth, T. P., Old, C. P., Bacon, S., Polyakov, I. V., Ivanov, V., and Hölemann, J.: Intermittent intense turbulent mixing under ice in the Laptev Sea continental shelf, Journal of Physical Oceanography, 41, 531–547, doi:10.1175/2010JPO4425.1, 2011.

Levine, M. D., Paulson, C. a., and Morison, J. H.: Internal waves in the Arctic Ocean - comparison with lower-latitude observations, Journal of Physical Oceanography, 15, 800–809, doi:10.1175/1520-0485(1985)015<0800:IWITAO>2.0.CO;2, 1985.

Martin, T., Steele, M., and Zhang, J.: Seasonality and long-term trend of Arctic Ocean surface stress in a model, Journal of Geophysical Research: Oceans, 119, 1723–1738, doi:10.1002/2013JC009425, 2014.

Martin, T., Tsamados, M., Schroeder, D., and Feltham, D. L.: The impact of variable sea ice roughness on changes in Arctic Ocean surface stress: A model study, Journal of Geophysical Research: Oceans, 121, 1931–1952, doi:10.1002/2015JC011186, 2016.

Martini, K. I., Simmons, H. L., Stoudt, C. A., and Hutchings, J. K.: Near-inertial internal waves and sea ice in the Beaufort Sea, Journal of Physical Oceanography, 44, 2212–2234, doi:10.1175/JPO-D-13-0160.1, 2014.

McPhee, M. G., Kikuchi, T., Morison, J. H., and Stanton, T. P.: Ocean-to-ice heat flux at the North Pole environmental observatory, Geophysical Research Letters, 30, doi:10.1029/2003GL018580, 2003.

Meyer, A., Sloyan, B. M., Polzin, K. L., Phillips, H. E., and Bindoff, N. L.: Mixing variability in the Southern Ocean, Journal of Physical Oceanography, 45, 966–987, doi:10.1175/JPO-D-14-0110.1, 2015.

Meyer, A., Polzin, K. L., Sloyan, B. M., and Phillips, H. E.: Internal waves and mixing near the Kerguelen Plateau, Journal of Physical Oceanography, 46, 417–437, doi:10.1175/JPO-D-15-0055.1, 2016.

Mooers, C. N. K.: Several effects of a baroclinic current on the cross-stream propagation of inertial-internal waves, Geophysical Fluid Dynamics, 6, 245–275, doi:10.1080/03091927509365797, 1975.

Nagai, T., Tandon, A., Kunze, E., and Mahadevan, A.: Spontaneous generation of near-inertial waves by the Kuroshio Front, Journal of Physical Oceanography, 45, 2381–2406, doi:10.1175/JPO-D-14-0086.1, 2015.

Padman, L. and Dillon, T. M.: Turbulent mixing near the Yermak Plateau during the Coordinated Eastern Arctic Experiment, Journal of Geophysical Research-Oceans, 96, 4769–4782, doi:10.1029/90JC02260, 1991.

Padman, L. and Erofeeva, S.: A barotropic inverse tidal model for the Arctic Ocean, Geophysical Research Letters, 31, 2–5, doi:10.1029/2003GL019003, 2004.

Pawlowicz, R., Beardsley, R. C., and Lentz, S.: Classical tidal harmonic analysis including error estimates in MATLAB using t_tide, Computers and Geosciences, 28, 929–937, 2002.

Peterson, A. K. and Fer, I.: Measurements of ocean currents, temperature and salinity from moorings at the Yermak Plateau: September 2014 – September 2015, Tech. rep., Geophysical Institute, University of Bergen, 2017.

Peterson, A. K., Fer, I., McPhee, M. G., and Randelhoff, A.: Turbulent heat and momentum fluxes in the upper ocean under Arctic sea ice, Journal of Geophysical Research - Oceans, 122, 1–18, doi:10.1002/2016JC012283, 2017.

Pite, H. D., Topham, D. R., and van Hardenberg, B. J.: Laboratory measurements of the drag force on a family of two-dimensional ice keel models in a two-layer flow, Journal of Physical Oceanography, 25, 3008–3031, doi:10.1175/1520-0485(1995)025<3008:LMOTDF>2.0.CO;2, 1995.

Pnyushkov, A. V. and Polyakov, I. V.: Observations of tidally induced currents over the continental slope of the Laptev Sea, Arctic Ocean, Journal of Physical Oceanography, 42, 78–94, doi:10.1175/JPO-D-11-064.1, 2011.

Rainville, L. and Woodgate, R. A.: Observations of internal wave generation in the seasonally ice-free Arctic, Geophysical Research Letters, 36, L23 604, doi:10.1029/2009GL041291, 2009.

Rampal, P., Weiss, J., and Marsan, D.: Positive trend in the mean speed and deformation rate of Arctic sea ice, 1979-2007, Journal of Geophysical Research: Oceans, 114, 1–14, doi:10.1029/2008JC005066, 2009.

Rippeth, T. P., Lincoln, B. J., Lenn, Y.-D., Green, J. A. M., Sundfjord, A., and Bacon, S.: Tide-mediated warming of Arctic halocline by Atlantic heat fluxes over rough topography, Nature Geoscience, 8, 191–194, doi:10.1038/ngeo2350, 2015.

Schulze, L. M. and Pickart, R. S.: Seasonal variation of upwelling in the Alaskan Beaufort Sea: Impact of sea ice cover, Journal of Geophysical Research: Oceans, 117, 1–19, doi:10.1029/2012JC007985, 2012.

Simmons, H. L., Hallberg, R. W., and Arbic, B. K.: Internal wave generation in a global baroclinic tide model, Deep-Sea Research, 51, 3043–3068, doi:10.1016/j.dsr2.2004.09.015, 2004.

Sirevaag, A. and Fer, I.: Early spring oceanic heat fluxes and mixing observed from drift stations north of Svalbard, Journal of Physical Oceanography, 39, 3049–3069, doi:10.1175/2009JPO4172.1, 2009.

Skyllingstad, E. D., Paulson, C. A., Pegau, W. S., McPhee, M. G., and Stanton, T. P.: Effects of keels on ice bottom turbulence exchange, Journal of Geophysical Research, 108, 3372, doi:10.1029/2002JC001488, 2003.

Spreen, G., Kwok, R., and Menemenlis, D.: Trends in Arctic sea ice drift and role of wind forcing: 1992-2009, Geophysical Research Letters, 38, 1–6, doi:10.1029/2011GL048970, 2011.

Vlasenko, V., Stashchuk, N., and Hutter, K.: Baroclinic tides: Theoretical modeling and observational evidence, Cambridge University Press, 2005.

Zappa, G., Shaffrey, L., and Hodges, K.: Can polar lows be objectively identified and tracked in the ECMWF operational analysis and the ERA-Interim reanalysis?, Mon. Wea. Rev., 142, 2596–2608, doi:10.1175/mwr-d-14-00064.1, 2014.

Chapter 5

Conclusions

5.1 Main results

The under-ice turbulence measurements presented here sets a new benchmark for oceanic heat fluxes to the sea ice. In the interior Arctic in winter, observed heat fluxes typically are $O(1\,W\,m^{-2})$, similar to previously reported values. Mixing events during storms lead to order-of-magnitude higher heat fluxes for short duration, and this study has found one-dimensional processes to be important for vertical mixing in the interior, away from significant topography. Our 1D model indicates that as much as 90% of the salt increase observed in the mixed layer came from entrainment by saline water from below, and only 10% came from brine rejection from ice formation.

Later in the season, and closer to the Yermak Plateau, we observed heat fluxes reaching $O(100\,W\,m^{-2})$, in response to a wind event concurrent with warm water close to the surface. We found that the commonly used bulk parametrization for heat fluxes agreed well with our direct measurements. However, at two occasions in the end of May, we found that the bulk formula overestimated heat flux, which we hypothesize was caused by accumulated freshwater from sea ice melt. The parametrization held for the rapid melting conditions in June.

During the rapidly melting last floe of N-ICE2015, heat and salt fluxes were inversely related, contrary to expectations during melt. From the flux measurements, plumes of brine descending past the measurement volume were identified. The accumulated measured salt flux was comparable to salt content of nearby ice cores, indicating a nearly full desalination as the ice melted. The findings indicate that the brine and fresh meltwater leave the ice separately, rather than as a homogenous water mass with salinity equal to the bulk salinity of the sea ice.

From mooring observations on the southwestern Yermak Plateau, we have studied the near-inertial wave field over a one-year period. We observe evidence of surface-generated near-inertial internal waves, likely forced by wind events. This is evident from the strong

clockwise polarization of the currents, which indicates downward propagation of energy. The clockwise polarization is stronger closer to the surface. Examples of wind-generated near-inertial waves are presented, and we calculate wave group properties for one event. We also find that tidal forcing is significant in the observations, with dominance of the K_1 diurnal and M_2 semidiurnal components. This extends previous findings from other parts of the plateau, and shows that the tidal interaction with topography is important. Elevated near-inertial energy at intermediate depths can be caused by remotely generated internal waves propagating downward from the surface, but we also find that the location of enhanced energy at specific depths is consistent with beam paths of a near-inertial tidal wave generated at the shelf break.

5.2 Outlook

As our observations show that oceanic heat fluxes are significantly elevated during storms, and more generally that turbulent fluxes are largely dominated by individual events, future changes may have significant impact on turbulent mixing. Connecting the observations with predicted further decrease in sea ice concentration, increasing storm activity and drift speed, heat flux to the interior ice pack may be increasing in a future Arctic Ocean. These effects compete with the stronger stratification due to increasing freshwater runoff at the surface, and their relative importance needs further study.

The findings of brine plumes below melting Arctic sea ice show that there is still much to learn about processes at the interface between sea ice and the ocean. Why did we observe brine plumes below the ice, while Sirevaag (2009) found that doubly diffusive processes were altering the heat fluxes during melt? More targeted campaigns are needed to clarify these processes, and for example by better coordinating under-ice observations with targeted ice coring to follow the desalination more closely.

The data collected during N-ICE2015 can probably still reveal much more about the Arctic Ocean, the marginal ice zone and air-ice-sea interactions. A further study of the effect of storms on the ice floes, and connecting it to all the measured components from N-ICE, would be very interesting to pursue. This, and several more studies following the N-ICE campaign have already been planned, and will be followed up by the N-ICE group.

The mooring data collected for this project also holds potential for further studies. Because of unfortunate sea ice conditions during deployment, the moorings were not in an area which was fully ice covered in winter. Thus we were unable to address one of the issues we had originally intended, which was to study the impact of the seasonal sea ice cover on the near-inertial wave field. This is a topic that still deserves attention in future studies. However, the moorings were placed in an area where many processes take place, and the combination of near-inertial wave generation revealed in this study near

the strong boundary current invites to further study possible trapping of near-inertial waves along the coast, as has been observed elsewhere.

There is a continuing need to study mixing processes in the Arctic Ocean. This can be aided by increasingly advanced drifting platforms designed for use in sea ice, such as the ITP (Ice-tethered profiler) and the IAOOS (Integrated Arctic Ocean Observing System) buoys. In addition to the autonomous systems, manned drifts will still be needed for much of the research. Drift campaigns in the Arctic Ocean such as the N-ICE campaign provide invaluable data sets to aid our understanding of the Arctic climate system. Similar to the SHEBA (Surface Heat Budget of the Arctic) drift, I believe the N-ICE project will produce new research for many years to come. Another big drift project that is already under way is MOSAiC (Multidisciplinary drifting Observatory for the Study of Arctic Climate), where the icebreaker Polarstern will drift across the Arctic Ocean in a yearlong drift campaign starting in fall 2019. This, and other projects are needed to further improve our understanding of the atmosphere-ice-ocean system, and processes impacting the mass and energy budgets of the sea ice.

Appendix A

Free Drift Force Balance During N-ICE2015

The sea ice drift is forced by winds, internal ice stress, as well as oceanic processes such as baroclinic tides and geostrophic currents. Following McPhee (2013), wind-driven component of the ice drift, $\mathbf{V}_{fd}$, can be found through the free-drift force balance,

$$imf\mathbf{V}_{fd} = \rho_a c_{10}\mathbf{W}_{10}\mathrm{W}_{10} - \rho_w \mathbf{u}_{*0}u_{*0}, \tag{A.1}$$

where m is the ice mass per unit area, $f = 1.4 \times 10^{-4}\,\mathrm{s}^{-1}$ is the Coriolis parameter, $\rho_a = 1.3\,\mathrm{kg\,m}^{-3}$ and $\rho_w = 1030\,\mathrm{kg\,m}^{-3}$ are densities of air and water, respectively, and C_{10} is the air-ice drag coefficient. Vectors are typed in bold font. The friction velocity at the ice-ocean interface, $\mathbf{u}_{*0}$, is related to $\mathbf{V}_{fd}$ through a Rossby-similarity drag relation,

$$\frac{\mathbf{V}_{fd}}{\mathbf{u}_{*0}} = \frac{1}{\kappa}\left(log\frac{\mathbf{u}_{*0}}{fz_0} - A - iB\right), \tag{A.2}$$

where z_0 is the surface roughness length, A and B are constants (McPhee, 2012). We solve Equations A.1 and A.2 iteratively from an initial guess, using hourly N-ICE wind speed data and appropriate parameters from SHEBA ($C_{10} = 15 \times 10^{-4}$, $z_0 = 0.04\,\mathrm{m}$, $A = 1.91$, $B = 2.12$ McPhee, 2008) The ship's weather mast provided wind data (Figure 3b in Paper I). Ice mass is calculated from ice density $\rho_{ice} = 920\,\mathrm{kg\,m}^{-3}$ and ice thickness, for which we use an average value typical for each ice floe, obtained after surveys conducted by the ice physics group. Since all floes had considerable snow depth, we account for this by calculating the equivalent ice mass, assuming a density $\rho_{snow} = 400\,\mathrm{kg\,m}^{-3}$. Total ice mass equivalent per unit area was then 1.1 m, 1.4 m, 2.0 m and 1.0 m for Floes 1-4, respectively. Results are not very sensitive to the exact choice of ice thickness.

A comparison of the calculated free-drift trajectories to the observed drift is shown in Figure A.1. For Floes 1 and 2, a large discrepancy between observed and free drifts arises during southerly winds. While the wind pushes the ice northward, internal stress

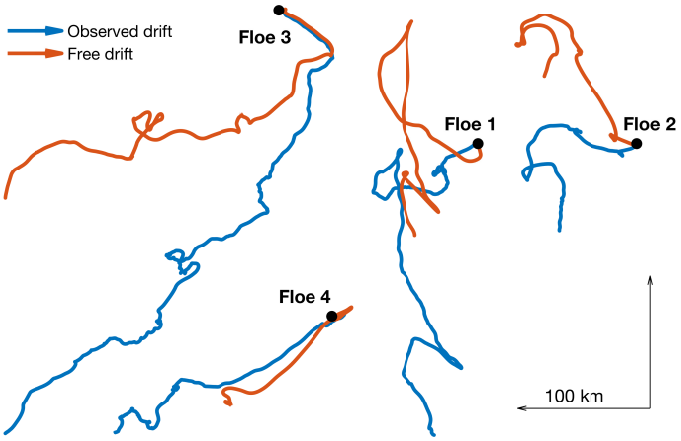

Figure A.1: Free drift, calculated from Equations A.1 and A.2, compared to the observed drift. Starting positions (black dots) are arbitrary.

prevents the ice from moving northward. When the wind turns northerly, the observed drift resembles free drift. Floe 3 drifts further south than what free drift predicts. This is consistent with currents flowing along the slope of the YP. Floe 4 drift is close to the free drift prediction, however, the discrepancy is in the opposite direction of the expected eastward flow of AW across the YP. Comparison between the free drift $u_{*\mathrm{fd}}$ and the spectral u_{*s} (Figure A.2) confirms the general picture: Friction velocity from the free drift calculations ($u_{*\mathrm{fd}}$) is higher than observed $u_{*,s}$ (from spectra) 87% of the time, and on average u_* is about half of $u_{*\mathrm{fd}}$. The difference is largest ($u_{*s}/u_{*\mathrm{fd}} = 0.3$) in Floes 1 and 2, where drift is mostly confined to the interior ice pack (on average 200 km from the ice edge). There is a tendency towards better agreement between the two for lower ice concentrations, and averaged over Floes 3 and 4, we find $u_{*s}/u_{*\mathrm{fd}} = 0.59$ and 0.65, respectively. The free drift equations neglect internal ice stress and background currents, and deviations between free drift and observed drift suggests the presence of other forcing.

The free drift analysis shows that momentum transfer can be sensitive to wind direction, as well as sea ice concentration. Further decreases in sea ice concentration will allow sea ice to flow more like the free drift, and together with increased storminess in the Arctic, momentum transfer to the upper ocean is likely to increase.

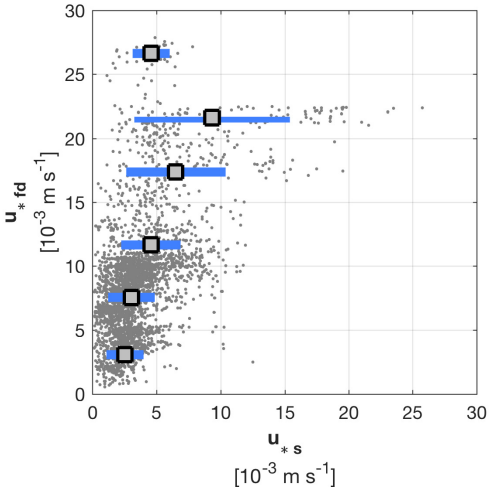

Figure A.2: Comparison of friction velocity derived from spectra of vertical velocity (u_{*s}) and free drift calculations (u_{*fd}). Also shown are averages in $5 \times 10^{-}3$ wide bins of u_{*fd} (squares), and the standard deviation of each bin (bars).

Appendix B

Mooring Deployment and Processing

The following sections contain information about the deployment of the moorings and processing of the data from the moored instruments. The information is largely similar to that given in the mooring report (Peterson and Fer, 2017), but is repeated here for completeness.

B.1 Deployment

B.1.1 Location

Three moorings were deployed on the western slope of Spitsbergen, at about 80°N. The moorings were deployed from the Norwegian coast guard vessel KV Svalbard in September 2014, and recovered in August 2015 by research vessel (RV) Håkon Mosby. The moorings were placed in a south to north line along the slope (Figure 2.4). Placement of the moorings were limited by unusually large sea ice cover in the region in September 2014. Exact locations, depths and deployment times are given in Table 1. As the echo sounder of KV Svalbard was unreliable, depths from RV Håkon Mosby's echo sounder upon retrieval are also given.

The moorings were originally named Y1, Y2 and Y3, but were renamed to M12, M8 and M15 for clarity in publication, corresponding to their deployment depths (e.g., M8 was deployed at approximately 800 m depth). In the following, we use the original (Y) names for consistency with the mooring drawings.

B.1.2 Instrumentation

The moorings were equipped with temperature, salinity, pressure and current sensors, designed to capture near-inertial internal waves. See the mooring drawings (Appendix)

Mooring	Y1 (M15)	Y2 (M8)	Y3 (M12)
Longitude	5E 57.541	5E 48.733	5E 56.333
Latitude	79N 37.209'	80N 03.876'	79N 44.093'
Echo depth	1535 m	850 m	1209 m
Recovery depth	1609 m	863 m	1327 m
Deployed (UTC)	10.09.2014 18:55	10.09.2014 09:05	11.09.2014 10:47
Recovered (UTC)	13.08.2015 17:00	13.08.2015 08:00	13.08.2015 13:00

Table B.1: Mooring deployment and recovery details.

for detailed overview of instruments, serial numbers and planned deployment depth.

B.2 Data Processing

B.2.1 Mooring blowdown and pressure drift

Strong currents occasionally blow down the mooring lines. To account for this, we created a pressure matrix from the SBE37 and SBE39 pressure sensors. For each hourly time step, pressure is linearly interpolated to the other instrument depths, based on the planned distance along the wire from the pressure sensors.

Pressure readings can drift through the deployment. A check of pressure of all SBE instruments before and after recovery reveals drift of about 1dBar in one sensor (SBE37, SN6018). The other sensors show pressure within 0.2dBar of pre-deploymen values. 1dBar is considered to be acceptable, as other error sources are larger, and we did not correct for this drift.

B.2.2 Time resolution and vertical resolution

The instruments sampled at different intervals, and to create a unified structure, we adjusted this to 1 hour intervals. Instruments with a higher frequency were bin-averaged to 1 hour, and instruments with 1 hour intervals were linearly interpolated to the common time-stamp. No instruments had lower sampling frequency than 1 hour.

Data was interpolated to a 5 m vertical grid.

B.2.3 Offset corrections

We compared mooring data to CTD casts performed shortly after each mooring deployment. The CTD cast was compared to mooring data within 3 hours, and to the deployment-averaged profiles. Some instruments showed a systematic offset (particularly when looking at month/yearlong vertical profiles). If these were covered by other instruments that we deemed more reliable (consistent), the offset data were discarded. When there was no overlap, and it seemed otherwise reasonable to do so (particularly at depth), we corrected the offset in comparison with nearby sensors.

Salinity corrections

Y1 was the only mooring which had systematic offsets in salinity. We corrected all sensors systematically with +0.006, to better match the CTD data. In addition, one sensor (SBE-CT, sn 8973) had an offset of -0.04 relative to the others, which we corrected for.

On Y2, some of the salinity sensors made temporary offsets, lasting for up to a few weeks. This was presumably due to blocking of the salinity cell, preventing throughflow. We made an attempt at correcting for this, but the offset was not constant in time, so we decided to discard these data.

B.2.4 Current data – Compass corrections

In some places, ADCP data overlapped with other instuments, such as SeaGuards or RCM-7s. Here we checked for consistency, and then used one of the data sets. If the data sets agree well, we typically used the ADCP data because of better spatial coverage.

One ADCP, the uplooking RCM longranger 21444 on Y1, had issues with its compass. After comparing to the nearby current measurements on the same mooring, and to current measurements on the other two moorings, we corrected the compass for an offset. This was done by matching its first 3 bins to the first 3 bins of the downlooking ADCP on the same buoy.

Because of compass calibration errors, we needed to correct current direction on a number of instruments. A downlooking Longranger ADCP compass on Y2 (SN 18447) was corrected against the uplooking Longranger mounted on the same buoy (SN 17226) by matching the three first bins of the two instruments. Similar corrections were made for other ADCPs, listed in Table B.2.

We did not correct for magnetic declination. The declination in mid-deployment (Feb 24, 2015) at 79.621°N, 5.9590°E was 0.84°E, with an error margin of 0.83°, and changing by 0.41°E per year. Compass uncertainty is about 5°. Declination was calculated using NOAA's magnetic field calculator at `http://www.ngdc.noaa.gov/geomag-web/#declination`.

Y1

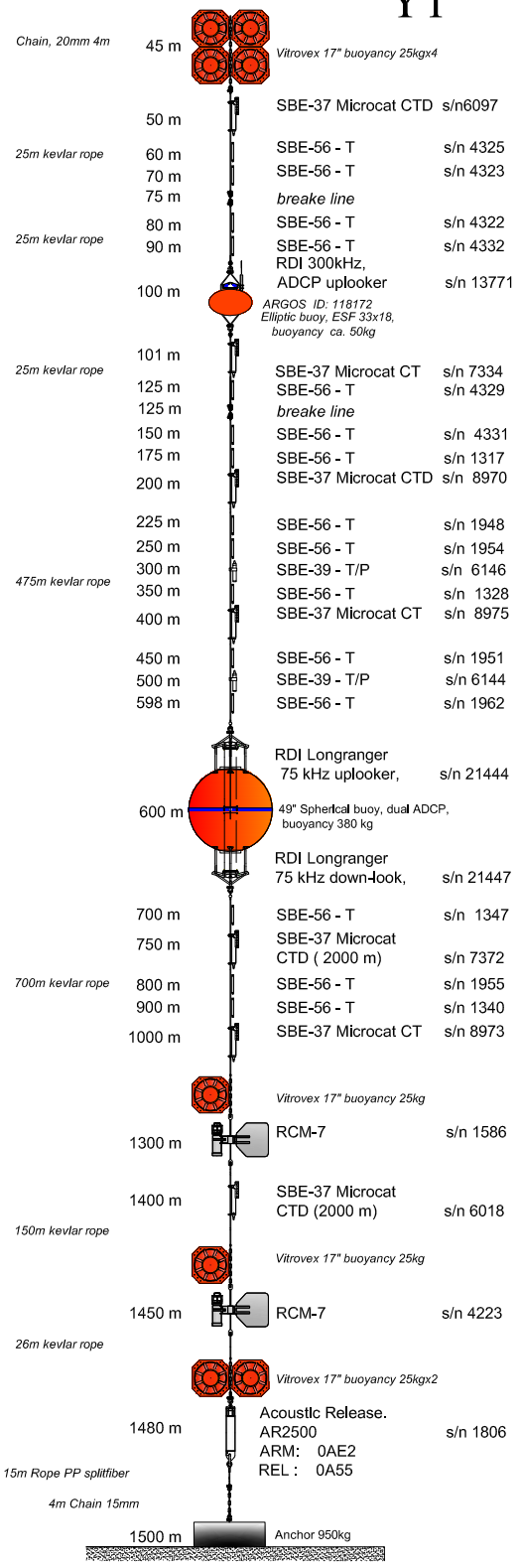

UNIVERSITETET I BERGEN
Geofysisk Institutt

Project:
Location: Yermak Plateau
Position: N 79 37.209 E 005 57.541
Depth: 1535 m
Deployment:
Recover:

SBE37- CTD	4
SBE37 - CT	3
SBE56	15
SBE39 T/P	2
ADCP LR	2
ADCP 300kHz	1
RCM Aadi	2
Argos,ID:118172	1
Ixsea AR 2500 s/n 1806	1

Arm code:	**0AE2**
Release	Arm + 0A55
Release with ping	Arm + 0A56
Pinger on	Arm + 0A47
Pinger of	Arm + 0A48
Diagnostic	Arm + 0A49

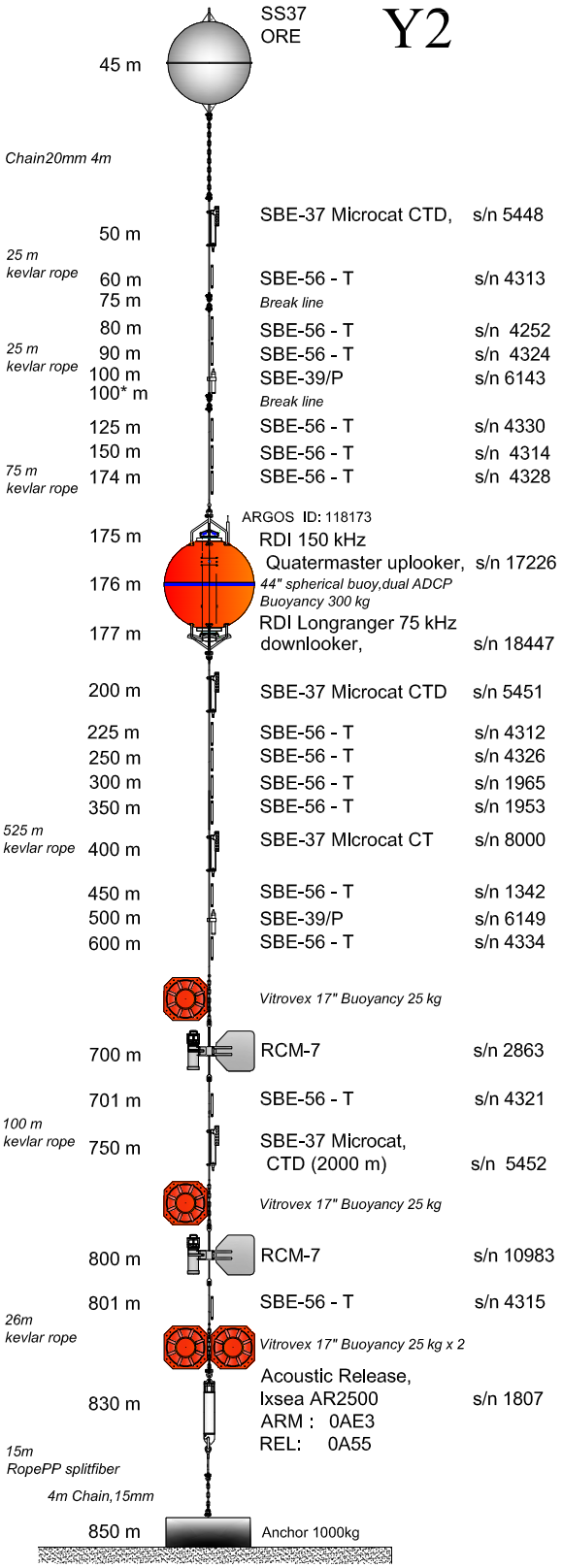

UNIVERSITETET I BERGEN
Geofysisk Institutt

Project:	
Location:	Yermak Plateau
Position:	N 80 03.876 E 005 48.733
Depth:	850 m
Deployment:	
Recover:	

SBE37- CTD	3
SBE37 - CT	1
SBE56	16
ADCP LR	1
ADCP 150kHz	1
RCM Aadi	2
Argos,ID:118173	1
Ixsea AR 2500 s/n 1807	1

Arm code:	**0AE3**
Release	Arm + 0A55
Release with ping	Arm + 0A56
Pinger on	Arm + 0A47
Pinger of	Arm + 0A48
Diagnostic	Arm + 0A49

Y3

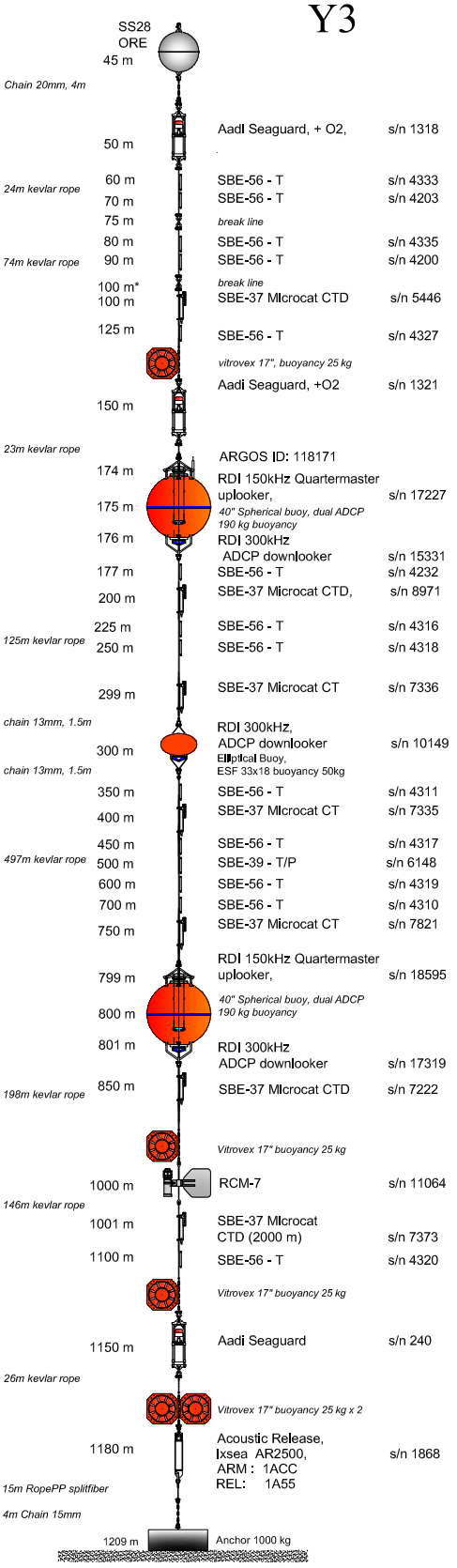

UNIVERSITETET I BERGEN
Geofysisk Institutt

Project:
Location: Yermak Plateau
Position: N 79 44.093 E 005 56.333
Depth: 1209 m
Deployment:
Recover:

SBE37- CTD	4
SBE37 - CT	3
SBE56	13
SBE39 T/P	1
ADCP 150kHz	2
ADCP 300kHz	3
RCM-7 Aadi	1
Seaguard Aadi	3

Argos,ID:118171 1

Ixsea AR 2500 1
s/n 1868

Arm code:	1**ACC**
Release	Arm + 1A55
Release with ping	Arm + 1A56
Pinger on	Arm + 1A47
Pinger of	Arm + 1A48
Diagnostic	Arm + 1A49

	Corrected instrument			Corrected against		
Mooring	Instrument	S/N	Type	Instument	S/N	Type
Y1	RDI75 kHz	21444	Uplooker	RDI 75 kHz	21447	Downlooker
Y2	RDI 75 kHz	18447	Downlooker	RDI 150 kHz	17226	Uplooker
Y3	RDI 300 kHz	15331	Downlooker	RDI 150 kHz	17227	Uplooker
Y3	RDI 150 kHz	18595	Uplooker	RDI 300 kHz	17319	Downlooker
Y3	RCM-7	11064	Point	RDI 300 kHz / SeaGuard	17319 / 240	Downlooker / Point
Y3	RDI 300 kHz	10149	Downlooker	RDI 150 kHz	18595	Uplooker
Y3	SeaGuard	1321	Point			60° CW

Table B.2: Overview of instruments corrected for compass error or calibration errors.

Bibliography

Aagaard, K., Coachman, L. K. and Carmack, E. C. (1981), 'On the halocline of the Arctic Ocean', *Deep Sea Research Part A, Oceanographic Research Papers* **28**(6), 529–545. doi: 10.1016/0198-0149(81)90115-1. 1.1.2, 1.2

Aagaard, K. and Greisman, P. (1975), 'Toward new mass and heat budgets for the Arctic Ocean', *Journal of Geophysical Research* **80**(27), 3821–3827. doi: 10.1029/JC080i027p03821. 1.1.1

Aagard, K. and Carmack, E. C. (1989), 'The role of sea ice and other fresh water in the Arctic circulation', *Journal of Geophysical Research* **94**(1), 14,414–485,498. doi: 10.1029/JC094iC10p14485. 1.2

Alford, M. H. (2003), 'Redistribution of energy available for ocean mixing by long-range propagation of internal waves.', *Nature* **423**(6936), 159–162. doi: 10.1038/nature01628. 1.3.2

Alford, M. H., MacKinnon, J. A., Simmons, H. L. and Nash, J. D. (2016), 'Near-inertial internal gravity waves in the ocean.', *Annual review of marine science* **8**, 95–123. doi: 10.1146/annurev-marine-010814-015746. 1.3.2

Årthun, M., Eldevik, T., Smedsrud, L. H., Skagseth, Ø. and Ingvaldsen, R. B. (2012), 'Quantifying the influence of atlantic heat on Barents Sea ice variability and retreat', *Journal of Climate* **25**(13), 4736–4743. doi: 10.1175/JCLI-D-11-00466.1. 1.2

Årthun, M. and Schrum, C. (2010), 'Ocean surface heat flux variability in the Barents Sea', *Journal of Marine Systems* **83**(1-2), 88–98. doi: 10.1016/j.jmarsys.2010.07.003. 1.1.1

Beszczynska-Möller, A., Fahrbach, E., Schauer, U. and Hansen, E. (2012), 'Variability in Atlantic water temperature and transport at the entrance to the Arctic Ocean, 1997-2010', *ICES Journal of Marine Science* **69**(5), 852–863. doi: 10.1093/icesjms/fss056. 1.1.1

Bitz, C. M., Holland, M. M., Hunke, E. C. and Moritz, R. E. (2005), 'Maintenance of the sea-ice edge', *Journal of Climate* **18**(15), 2903–2921. doi: 10.1175/JCLI3428.1. 1.2

Björk, G., Söderkvist, J., Winsor, P., Nikolopoulos, A. and Steele, M. (2002), 'Return of the cold halocline layer to the Amundsen Basin of the Arctic Ocean: Implications for the sea ice mass balance', *Geophysical Research Letters* **29**(11), 1513. doi: 10.1029/2001GL014157. 1.1.2

Boyd, T. J., Steele, M., Muench, R. D. and Gunn, J. T. (2002), 'Partial recovery of the Arctic Ocean halocline', *Geophysical Research Letters* **29**(14), 1–4. doi: 10.1029/2001GL014047. 1.1.2

Carmack, E. C., Polyakov, I. V., Padman, L., Fer, I., Hunke, E., Hutchings, J. K., Jackson, J., Kelley, D. E., Kwok, R., Layton, C., Melling, H., Perovich, D. K., Persson, O., Ruddick, B., Timmermans, M.-L. L., Toole, J. M., Ross, T., Vavrus, S. and Winsor, P. (2015), 'Toward quantifying the increasing role of oceanic heat in sea ice loss in the new Arctic', *Bulletin of the American Meteorological Society* **96**(12), 2079–2105. doi: 10.1175/BAMS-D-13-00177.1. 1.1, 1.2, 1.3.3

Cohen, L., Hudson, S. R., Walden and Granskog, M. A. (n.d.), 'Meteorological conditions in a thinner Arctic sea ice regime from winter through summer during the Norwegian young sea ICE expedition (N-ICE2015)', *Journal of Geophysical Research* p. submitted. 2.2.1

Cole, S. T., Timmermans, M.-L., Toole, J. M., Krishfield, R. A. and Thwaites, F. T. (2014), 'Ekman veering, internal waves, and turbulence observed under Arctic sea ice', *Journal of Physical Oceanography* **44**(5), 1306–1328. doi: 10.1175/JPO-D-12-0191.1. 1.3.1, 1.3.3

Curry, J. A., Schramm, J. L. and Ebert, E. E. (1995), 'Sea-ice albedo climate feedback mechanism', *Journal of Climate* **8**(2), 240–247. doi: 10.1175/1520-0442(1995)008<0240:SIACFM>2.0.CO;2. 1.3.1

D'Asaro, E. A. and Morison, J. H. (1992), 'Internal waves and mixing in the Arctic Ocean', *Deep Sea Research Part A. Oceanographic Research Papers* **39**(2), S459–S484. doi: 10.1016/S0198-0149(06)80016-6. 1.3.2, 1.3.2

Dohan, K. and Davis, R. E. (2011), 'Mixing in the transition layer during two storm events', *Journal of Physical Oceanography* **41**(1), 42–66. doi: 10.1175/2010JPO4253.1. 1.3.2

Dosser, H. V., Rainville, L., Dosser, H. V. and Rainville, L. (2016), 'Dynamics of the Changing Near-Inertial Internal Wave Field in the Arctic Ocean', *Journal of Physical Oceanography* **46**(2), 395–415. doi: 10.1175/JPO-D-15-0056.1. 1.3.3

Eicken, H., Grenfell, T. C., Perovich, D. K., Richter-Menge, J. A. and Frey, K. (2004), 'Hydraulic controls of summer Arctic pack ice albedo', *Journal of Geophysical Research C: Oceans* **109**(8), 1–13. doi: 10.1029/2003JC001989. 1.2

Feltham, D. L., Untersteiner, N., Wettlaufer, J. S. and Worster, M. G. (2006), 'Sea ice is a mushy layer', *Geophysical Research Letters* **33**(14), 4–7. doi: 10.1029/2006GL026290. 1.2

Fer, I. (2009), 'Weak vertical diffusion allows maintenance of cold halocline in the central Arctic', *Atmospheric and Ocean Science Letters* **2**(3), 148–152. doi: 10.1080/16742834.2009.11446789. 1.1.2

Fer, I. (2014), 'Near-inertial mixing in the central Arctic Ocean', *Journal of Physical Oceanography* **44**(8), 2031–2049. doi: 10.1175/JPO-D-13-0133.1. 1.3.3

Fer, I., Müller, M. and Peterson, A. K. (2015), 'Tidal forcing, energetics, and mixing near the Yermak Plateau', *Ocean Science* **11**(2), 287–304. doi: 10.5194/os-11-287-2015. 1.3.2

Fer, I., Skogseth, R. and Geyer, F. (2010), 'Internal waves and mixing in the marginal ice zone near the Yermak Plateau', *Journal of Physical Oceanography* **40**(7), 1613–1630. doi: 10.1175/2010JPO4371.1. 1.3.2

Garrett, C. and Munk, W. (1975), 'Space-time scales of internal waves: A progress report', *Journal of Geophysical Research* **80**(3), 291–297. doi: 10.1029/JC080i003p00291. 1.3.2

Griewank, P. J. and Notz, D. (2015), 'A 1-D modelling study of Arctic sea-ice salinity', *Cryosphere* **9**(1), 305–329. doi: 10.5194/tc-9-305-2015. 1.2

Guthrie, J. D., Morison, J. H. and Fer, I. (2013), 'Revisiting internal waves and mixing in the Arctic Ocean', *Journal of Geophysical Research-Oceans* **118**, 3966–3977. 1.3.3

Holloway, G. and Proshutinsky, A. Y. (2007), 'Role of tides in Arctic ocean/ice climate', *Journal of Geophysical Research-Oceans* **112**(C4). doi: 10.1029/2006JC003643. 1.3.2

Hunkins, K. (1986), 'Anomalous diurnal tidal currents on the Yermak Plateau', *Journal of Marine Research* **44**(1), 51–69. doi: 10.1357/002224086788460139. 1.3.2

Jardon, F. P., Vivier, F., Vancoppenolle, M., Lourenço, A., Bouruet-Aubertot, P. and Cuypers, Y. (2013), 'Full-depth desalination of warm sea ice', *Journal of Geophysical Research: Oceans* **118**(1), 435–447. doi: 10.1029/2012JC007962. 1.2

Jeffries, M. O., Overland, J. E. and Perovich, D. K. (2013), 'The Arctic shifts to a new normal', *Physics Today* **66**(10), 35. doi: 10.1063/PT.3.2147. 1.2

Kowalik, Z. and Proshutinsky, a. Y. (1993), 'Diurnal tides in the Arctic Ocean', *Journal of Geophysical Research* **98**(C9), 16449. doi: 10.1029/93JC01363. 1.3.2

Laîné, A., Yoshimori, M. and Abe-Ouchi, A. (2016), 'Surface arctic amplification factors in CMIP5 models: Land and oceanic surfaces and seasonality', *Journal of Climate* **29**(9), 3297–3316. doi: 10.1175/JCLI-D-15-0497.1. 1.3.1

Lenn, Y.-D., Rippeth, T. P., Old, C. P., Bacon, S., Polyakov, I. V., Ivanov, V. and Hölemann, J. (2011), 'Intermittent intense turbulent mixing under ice in the Laptev Sea continental shelf', *Journal of Physical Oceanography* **41**(3), 531–547. doi: 10.1175/2010JPO4425.1. 1.3.2, 1.3.3

Levine, M. D., Paulson, C. a. and Morison, J. H. (1985), 'Internal waves in the Arctic Ocean - comparison with lower-latitude observations', *Journal of Physical Oceanography* **15**(6), 800–809. doi: 10.1175/1520-0485(1985)015<0800:IWITAO>2.0.CO;2. 1.3.2

Levine, M. D., Paulson, C. A. and Morison, J. H. (1987), 'Observations of internal gravity-waves under the Arctic pack ice', *Journal of Geophysical Research-Oceans* **92**(C1), 779–782. doi: 10.1029/JC092iC01p00779. 1.3.2

Lincoln, B. J., Rippeth, T. P., Lenn, Y.-D., Timmermans, M. L., Williams, W. J. and Bacon, S. (2016), 'Wind-driven mixing at intermediate depths in an ice-free Arctic Ocean', *Geophysical Research Letters* **43**(18), 9749–9756. doi: 10.1002/2016GL070454. 1.3.3

Lindsay, R. W. and Zhang, J. (2005), 'The thinning of Arctic sea ice, 1988–2003: Have we passed a tipping point?', *Journal of Climate* **18**(1999), 4879–4894. doi: 10.1175/JCLI3587.1. 1.3.1

Martin, T., Tsamados, M., Schroeder, D. and Feltham, D. L. (2016), 'The impact of variable sea ice roughness on changes in Arctic Ocean surface stress: A model study', *Journal of Geophysical Research: Oceans* **121**(3), 1931–1952. doi: 10.1002/2015JC011186. 1.3.1

Martini, K. I., Simmons, H. L., Stoudt, C. A. and Hutchings, J. K. (2014), 'Near-inertial internal waves and sea ice in the Beaufort Sea', *Journal of Physical Oceanography* **44**(8), 2212–2234. doi: 10.1175/JPO-D-13-0160.1. 1.3.1

Maykut, G. A. and McPhee, M. G. (1995), 'Solar heating of the Arctic mixed layer', *Journal of Geophysical Research* **100**(C12), 24691. doi: 10.1029/95JC02554. 1.1.2, 1.3.1

McPhee, M. G. (1992), 'Turbulent heat flux in the upper ocean under sea ice', *Journal of Geophysical Research* **97**(C4), 5365. doi: 10.1029/92JC00239. 1.3.1

McPhee, M. G. (2008), *Air-Ice-Ocean Interaction*, Springer, New York, NY. doi: 10.1007/978-0-387-78335-2. A

McPhee, M. G. (2012), 'Advances in understanding ice-ocean stress during and since AIDJEX', *Cold Regions Science and Technology* **76-77**(SI), 24–36. doi: 10.1016/j.coldregions.2011.05.001. A

McPhee, M. G. (2013), 'Intensification of geostrophic currents in the Canada Basin, Arctic Ocean', *Journal of Climate* **26**(10), 3130–3138. doi: 10.1175/JCLI-D-12-00289.1. 1.2, A

McPhee, M. G. (2017), The sea ice – ocean boundary layer, *in* D. N. Thomas, ed., 'Sea ice', 3rd edn, John Wiley & Sons, Ltd, chapter 5, pp. 138–159. 1.2

McPhee, M. G. and Kantha, L. H. (1989), 'Generation of internal waves by sea ice', *Journal of Geophysical Research* **94**(C3), 3287–3302. 1.3.1

McPhee, M. G., Kikuchi, T., Morison, J. H. and Stanton, T. P. (2003), 'Ocean-to-ice heat flux at the North Pole environmental observatory', *Geophysical Research Letters* **30**(24). doi: 10.1029/2003GL018580. 1.3.2

McPhee, M. G., Morison, J. H. and Nilsen, F. (2008), 'Revisiting heat and salt exchange at the ice-ocean interface: Ocean flux and modeling considerations', *Journal of Geophysical Research* **113**(C6), C06014. doi: 10.1029/2007JC004383. 1.2

Merrifield, M. A. and Pinkel, R. (1996), 'Inertial currents in the Beaufort Sea : Observations of response to wind and shear', *Journal of Geophysical Research* **101**(C3), 6577–6590. doi: 10.1029/95JC03625. 1.3.3

Morison, J. H., Long, C. E., Levine, D. and Levine, M. D. (1985), 'Internal wave dissipation under sea ice', *Journal of Geophysical Research* **90**(C6), 959–966. doi: 10.1029/JC090iC06p11959. 1.3.2

Morison, J. H., McPhee, M. G. and Maykut, G. A. (1987), 'Boundary layer, upper ocean, and ice observations in the Greenland Sea marginal ice zone', *Journal of Geophysical Research* **92**(C7), 6987. doi: 10.1029/JC092iC07p06987. 1.3.1

Nansen, F. (1902), 'Oceanography of the north polar basin: The Norwegian north polar expedition 1893-96', *Scientific Results* **3**(9). 1.2

Notz, D., McPhee, M. G., Worster, M. G., Maykut, G. A., Schlünzen, K. H. and Eicken, H. (2003), 'Impact of underwater-ice evolution on Arctic summer sea ice', *Journal of Geophysical Research* **108**(C7), 3223. doi: 10.1029/2001JC001173. 1.2

Notz, D. and Worster, M. G. (2009), 'Desalination processes of sea ice revisited', *Journal of Geophysical Research: Oceans* **114**(5), 1–10. doi: 10.1029/2008JC004885. 1.2

Nummelin, A., Ilicak, M., Li, C. and Smedsrud, L. H. (2016), 'Consequences of future increased Arctic runoff on Arctic Ocean stratification, circulation, and sea ice cover', *Journal of Geophysical Research: Oceans* **121**(1), 617–637. doi: 10.1002/2015JC011156. 1.3.3

Onarheim, I. H., Eldevik, T., Årthun, M., Ingvaldsen, R. B. and Smedsrud, L. H. (2015), 'Skillful prediction of Barents Sea ice cover', *Geophysical Research Letters* **42**(13), 5364–5371. doi: 10.1002/2015GL064359. 1.2

Onarheim, I. H., Smedsrud, L. H., Ingvaldsen, R. B. and Nilsen, F. (2014), 'Loss of sea ice during winter north of Svalbard', *Tellus A* **66**(1), 1–9. doi: 10.3402/tellusa.v66.23933. 1.2

Padman, L., Plueddemann, A. J., Muench, R. D. and Pinkel, R. (1992), 'Diurnal tides near the Yermak Plateau', *Journal of Geophysical Research* **97**(C8), 12639. doi: 10.1029/92JC01097. 1.3.2

Perovich, D. K. and Elder, B. C. (2002), 'Estimates of the ocean heat flux at SHEBA', *Geophysical Research Letters* **29**(9), doi:10.1029/2001GL01171. doi: 10.1029/2001GL014171. 1.1.2

Peterson, A. K. (2016), 'Varmt atlanterhavsvatn smelter is i Arktis', *Naturen* **139**(01), 36–41. doi: 10.18261/issn.1504-3118-2016-01-06. 1.5, 1.6

Peterson, A. K. and Fer, I. (2017), Measurements of ocean currents, temperature and salinity from moorings at the Yermak Plateau: September 2014 – September 2015, Technical report, Geophysical Institute, University of Bergen. B

Petrich, C. and Eicken, H. (2010), Growth, structure and properties of sea ice, *in* D. N. Thomas and G. S. Dieckmann, eds, 'Sea ice', 2nd edn, John Wiley & Sons, Ltd, chapter 2, pp. 23–77. 1.2

Pinkel, R. (2005), 'Near-inertial wave propagation in the western Arctic', *Journal of Physical Oceanography* **35**(5), 645–665. doi: 10.1175/JPO2715.1. 1.3.2, 1.4

Pite, H. D., Topham, D. R. and van Hardenberg, B. J. (1995), 'Laboratory measurements of the drag force on a family of two-dimensional ice keel models in a two-layer flow', *Journal of Physical Oceanography* **25**(12), 3008–3031. doi: 10.1175/1520-0485(1995)025<3008:LMOTDF>2.0.CO;2. 1.3.1

Plueddemann, A. J. (1992), 'Internal wave observations from the Arctic environmental drifting buoy', *Journal of Geophysical Research - Oceans* **97**(C8), 12619–12638. doi: 10.1029/92JC01098. 1.3.2

Polyakov, I. V., Alexeev, V. A., Ashik, I. M., Bacon, S., Beszczynska-Möller, A., Carmack, E. C., Dmitrenko, I. A., Fortier, L., Gascard, J. C., Hansen, E., Hölemann, J., Ivanov, V. V., Kikuchi, T., Kirillov, S., Lenn, Y.-D., McLaughlin, F. A., Piechura, J., Repina, I., Timokhov, L. A., Walczowski, W. and Woodgate, R. (2011), 'Fate of early 2000s Arctic warm water pulse', *Bulletin of the American Meteorological Society* **92**(5), 561–566. doi: 10.1175/2010BAMS2921.1. 1.1.1

Polyakov, I. V., Beszczynska-Möller, A., Carmack, E. C., Dmitrenko, I. A., Fahrbach, E., Frolov, I. E., Gerdes, R., Hansen, E., Holfort, J., Ivanov, V. V., Johnson, M. A., Karcher, M., Kauker, F., Morison, J. H., Orvik, K. A., Schauer, U., Simmons, H. L., Skagseth, Ø., Sokolov, V. T., Steele, M., Timokhov, L. A., Walsh, D. and Walsh, J. E. (2005), 'One more step toward a warmer Arctic', *Geophysical Research Letters* **32**(17), 1–4. doi: 10.1029/2005GL023740. 1.1.1

Polyakov, I. V., Pnyushkov, A. V., Alkire, M. B., Ashik, I. M., Baumann, T. M., Carmack, E. C., Goszczko, I., Guthrie, J. D., Ivanov, V. V., Kanzow, T., Krishfield, R., Kwok, R., Sundfjord, A., Morison, J. H., Rember, R. and Yulin, A. (2017), 'Greater role for Atlantic inflows on sea-ice loss in the Eurasian Basin of the Arctic Ocean', *Science* **291**, 285–291. doi: 10.1126/science.aai8204. 1.2

Rainville, L. and Winsor, P. (2008), 'Mixing across the Arctic ocean: Microstructure observations during the Beringia 2005 expedition', *Geophysical Research Letters* **35**(8). doi: 10.1029/2008GL033532. 1.3.1

Rainville, L. and Woodgate, R. A. (2009), 'Observations of internal wave generation in the seasonally ice-free Arctic', *Geophysical Research Letters* **36**(23), L23604. doi: 10.1029/2009GL041291. 1.3.3

Rampal, P., Weiss, J. and Marsan, D. (2009), 'Positive trend in the mean speed and deformation rate of Arctic sea ice, 1979-2007', *Journal of Geophysical Research: Oceans* **114**(5), 1–14. doi: 10.1029/2008JC005066. 1.2

Rippeth, T. P., Lincoln, B. J., Lenn, Y.-D., Green, J. A. M., Sundfjord, A. and Bacon, S.

(2015), 'Tide-mediated warming of Arctic halocline by Atlantic heat fluxes over rough topography', *Nature Geoscience* **8**(3), 191–194. doi: 10.1038/ngeo2350. 1.3.2

Rudels, B., Anderson, L. G. and Jones, E. P. (1996), 'Formation and evolution of the surface mixed layer and halocline in the Arctic Ocean', *Journal of Geophysical Research* **101**(C4), 8807–8821. doi: 10.1029/96JC00143. 1.1.2

Schauer, U. and Beszczynska-Möller, A. (2009), 'Problems with estimation and interpretation of oceanic heat transport - conceptual remarks for the case of Fram Strait in the Arctic Ocean', *Ocean Science* **5**(4), 487–494. doi: 10.5194/os-5-487-2009. 1.1.1

Schulze, L. M. and Pickart, R. S. (2012), 'Seasonal variation of upwelling in the Alaskan Beaufort Sea: Impact of sea ice cover', *Journal of Geophysical Research: Oceans* **117**(6), 1–19. doi: 10.1029/2012JC007985. 1.3.1

Serreze, M. C. and Stroeve, J. C. (2015), 'Arctic sea ice trends, variability and implications for seasonal ice forecasting', *Philosophical Transactions of the Royal Society A: Mathematical, Physical and Engineering Sciences* **373**(2045), 20140159. doi: 10.1098/rsta.2014.0159. 1.2

Shaw, W. J. and Stanton, T. P. (2014), 'Vertical diffusivity of the Western Arctic Ocean halocline', *Journal of Geophysical Research : Oceans* **119**, 5017–5038. doi: 10.1002/2013JC009598. 1.3.2

Shaw, W. J., Stanton, T. P., McPhee, M. G., Morison, J. H. and Martinson, D. G. (2009), 'Role of the upper ocean in the energy budget of Arctic sea ice during SHEBA', *Journal of Geophysical Research* **114**(C6), C06012. doi: 10.1029/2008JC004991. 1.1.2, 1.3.1

Sirevaag, A. (2009), 'Turbulent exchange coefficients for the ice/ocean interface in case of rapid melting', *Geophysical Research Letters* **36**(4), L04606. doi: 10.1029/2008GL036587. 1.2, 5.2

Skagseth, Ø. (2008), 'Recirculation of Atlantic Water in the western Barents Sea', *Geophysical Research Letters* **35**(11). doi: 10.1029/2008GL033785. 1.1.1

Skyllingstad, E. D., Paulson, C. A., Pegau, W. S., McPhee, M. G. and Stanton, T. P. (2003), 'Effects of keels on ice bottom turbulence exchange', *Journal of Geophysical Research* **108**(C12), 3372. doi: 10.1029/2002JC001488. 1.3.1

Spreen, G., Kwok, R. and Menemenlis, D. (2011), 'Trends in Arctic sea ice drift and role of wind forcing: 1992-2009', *Geophysical Research Letters* **38**(19), 1–6. doi: 10.1029/2011GL048970. 1.2

Stanton, T. P., Shaw, W. J. and Hutchings, J. K. (2012), 'Observational study of relationships between incoming radiation, open water fraction, and ocean-to-ice heat flux in the Transpolar Drift: 2002-2010', *Journal of Geophysical Research: Oceans* **117**(C7). doi: 10.1029/2011JC007871. 1.3.1

Steele, M. and Boyd, T. J. (1998), 'Retreat of the cold halocline layer in the Arctic Ocean', *Journal of Geophysical Research* **103**(C5), 10419. doi: 10.1029/98JC00580. 1.1.2

Tietsche, S., Notz, D., Jungclaus, J. H. and Marotzke, J. (2011), 'Recovery mechanisms of Arctic summer sea ice', *Geophysical Research Letters* **38**(2), 1–4. doi: 10.1029/2010GL045698. 1.3.1

Turner, J. S. (2010), 'The melting of ice in the Arctic Ocean: The influence of double-diffusive transport of heat from below', *Journal of Physical Oceanography* **40**(1), 249–256. doi: 10.1175/2009JPO4279.1. 1.1.1

Walsh, J. E., Fetterer, F., Scott Stewart, J. and Chapman, W. L. (2016), 'A database for depicting Arctic sea ice variations back to 1850', *Geographical Review* **107**(January), 89–107. doi: 10.1111/j.1931-0846.2016.12195.x. 1.2

Widell, K., Fer, I. and Haugan, P. M. (2006), 'Salt release from warming sea ice', *Geophysical Research Letters* **33**(12), L12501. doi: 10.1029/2006GL026262. 1.2

Winsor, P. and Björk, G. (2000), 'Polynya activity in the Arctic Ocean from 1958 to 1997', *Journal of Geophysical Research* **105**(1999), 8789. doi: 10.1029/1999JC900305. 1.2